9-2021

# Profiling Atmospheric Turbulence Using a Dynamically Ranged Rayleigh Beacon System

Steven M. Zuraski


# PROFILING ATMOSPHERIC TURBULENCE USING A DYNAMICALLY RANGED RAYLEIGH BEACON SYSTEM

DISSERTATION

Steven M. Zuraski, Civilian, USAF

AFIT-ENP

**DEPARTMENT OF THE AIR FORCE**
**AIR UNIVERSITY**

## AIR FORCE INSTITUTE OF TECHNOLOGY

**Wright-Patterson Air Force Base, Ohio**

AFIT-ENP-DS-21-S-036

# PROFILING ATMOSPHERIC TURBULENCE USING A DYNAMICALLY RANGED RAYLEIGH BEACON SYSTEM

DISSERTATION

Presented to the Faculty

Department of Engineering Physics

Graduate School of Engineering and Management

Air Force Institute of Technology

Air University

Air Education and Training Command

In Partial Fulfillment of the Requirements for the

Degree of Doctor of Philosophy

Steven M. Zuraski, BS, MS

Civilian, USAF

July 2021

AFIT-ENP-DS-21-S-036

# PROFILING ATMOSPHERIC TURBULENCE USING A DYNAMICALLY RANGED RAYLEIGH BEACON SYSTEM

Steven M. Zuraski, BS, MS

Civilian, USAF

Committee Membership:

Steven T. Fiorino, PhD
Chairman

Jack. E McCrae, PhD
Member

Richard K. Martin, PhD
Member

Elizabeth A. Beecher, PhD
Member

ADEDEJI B. BADIRU, PhD
Dean, Graduate School of Engineering and Management

AFIT-ENP-DS-21-S-036

## Abstract

The effect of turbulence on a long range imaging system manifest as an image blur effect usually quantified by the phase distortions present in a system. The blurring effect is conceivably understood on the basis of measured strength of atmospheric turbulence profiled within the propagation volume. One method for obtaining a turbulence strength profile is by use of a dynamically ranged Rayleigh beacon system that exploits strategically varied beacon ranges along the propagation path, effectively deducing estimates of specific path segment contributions of the blurring aberrations affecting an optical imaging system. A system utilizing this technique has been designed, and a prototype has been constructed for testing. This system is named TARDIS, which stands for Turbulence and Aerosol Research Dynamic Interrogation System. The TARDIS is an optical sensing system that is based on dynamically changing the range between the collecting sensor and Rayleigh beacon during a static period of relatively unchanging turbulence-induced wavefront perturbations. A notional collecting scenario consists of beacons where the air molecule and aerosol particle backscatter images captured at different distances from the collecting aperture based on laser pulsing and camera shutter speeds. Obtaining measurement based estimates of the turbulence strength profile from TARDIS is based around collating segmented refractive index structure parameter, $C_{n_{seg}}^2$, values traced to specific layers of the atmosphere. These $C_{n_{seg}}^2$ values are developed from Fried parameter segments, $r_{0_i}$, which are deduced from neighboring measurements on the Shack-Hartmann wavefront sensor. A single value of the Fried parameter is estimated from the mean of the variance of the phase present on the sensing system's collecting aperture. The mean of the variance of the estimated phase across the aperture is built from the zonal tilt tiles reconstructed from the Shack-Hartmann wavefront sensor measured gradients. This paper provides the foundational theory for understanding atmospheric turbulence, provides reference to currently available turbulence estimation techniques, and provides details towards TARDIS, the tomographic turbulence estimation methodology, and analysis of initial proof of concept data collected.

This body of research provides a novel means for quantifying the strength profile of atmospheric turbulence. Utilizing the outlined methodologies, a direct measurement of the perturbed wavefront is used which differs fundamentally from other means of estimating a turbulence strength profile. Due to this difference, the method of utilizing a dynamically ranged beacon to produce turbulence profile estimates could be used to add confidence to other methodologies or be used as an independent measurement technique that is not susceptible to the same set of error source influences. Furthermore, since this technology utilizes direct measurements of the wavefront, it is conceivable that this could be linked to an adaptive optics system used for image correction.

**Acknowledgments**

I would like to express my sincere appreciation to my faculty advisor, Steven T. Fiorino, for his guidance and support throughout the course of this dissertation effort. The insight and experience was certainly appreciated. I would, also, like to thank my committee members Elizabeth Beecher, Jack McCrae, and Richard Martin for their involvement in this research effort. Additionally, I would like to thank the Air Force Research Laboratory Sensors Directorate Multispectral Sensing Division for both the support and latitude provided to me in this endeavor. Lastly, a special thanks needs to be given to the team members from Applied Optimization who spent many long nights with me collecting data and troubleshooting the sensor system at the John Bryan Observatory.

Steven M. Zuraski

## Table of Contents

Page

## List of Figures

## List of Tables

# PROFILING ATMOSPHERIC TURBULENCE USING A DYNAMICALLY RANGED RAYLEIGH BEACON SYSTEM

## I. Introduction

Atmospheric turbulence has a wide-spread effect degrading the capability of optical systems utilized for laser beam propagation, free space optical communication, and terrestrial imaging systems. Fluctuations due to turbulence across a projected wavefront cause a loss of coherence in the beam, beam broadening, beam wander, intensity fluctuations known as scintillation, and intensity hot spots within the beam. All of these are typically unwanted effects, and consequently a body of research has developed in order to provide mitigation strategies. In order to develop a mitigation strategy, the first step is to gain or assume some knowledge of the strength and distribution of the turbulence along the propagation path. However, this is a very difficult thing to do as turbulence is random in nature, constantly changing, and difficult to quantify as a profiled strength quantity. This has led to the development of models, approximations, and assumed values for the atmospheric turbulence strength profile in absence of a direct measurement. Additionally, there are numerous strategies for deducing the profiled strength of turbulence by inferring it from more easily measured quantities or by taking volumetric measurements and scaling a modeled profile. The aim of this research was to provide a novel means for directly measuring the turbulence strength profile along the path.

Knowledge of the strength of the turbulence and how it varies along the path is needed in order to mitigate and overcome unwanted effects. A common metric for this is the refractive index structure parameter, $C_n^2$, which provides a quantified way of describing strength of turbulence along the viewing or propagation path. However, $C_n^2$ is not a quantity that is measurable in a continuous fashion along the propagation path of an optical wave. In order to create a $C_n^2$ profile, this

innovative research developed a sensing system that registers wavefront measurements representative of discrete diversified volumes of the atmosphere in rapid succession such that the ensemble of measurements provides a discretized direct measurement of the profiled turbulence strength. These resultant measurements will provide insight into the validity of various models and other indirect forms of deducing the profiled strength of atmospheric turbulence.

Analysis of prior research serves as the starting point for this proposed research identifying the strengths of sensing techniques and gaps in prior system capabilities. The theoretical framework provided a common language for discussing and evaluating the capability of the measurement systems. Preparatory research conducted provided base calculations showing the feasibility of this leading-edge research and also showed some initial engineering hurdles that had to be mitigated in the design of this system. Initial feasibility research led to an optimized system design, cost analysis, and system part realization. Parts were subsequently purchased and tested in the lab as critical sub-systems. After initial laboratory based testing was completed, the sub-systems were installed at the John Bryan Observatory on the telescope system housed there. Preliminary on-sky testing led to some key discoveries in the sensing system that were unique to dynamic ranging of a Rayleigh beacon. One key effect involved the Pockels cell's ability to act as an optical shutter in the presence of converging light fields that were induced from changing the range of the Rayleigh beacon. This effect was analyzed by evaluating the polarized pupil relayed through the sensing system, and a re-design of the optical beam relay was conducted to minimize unwanted effects. After this re-design of the sensing system beam relay, successful proof of concept dynamic ranging was demonstrated. This validated the novel sensing concept's ability to produce a discretized measurement of the turbulence strength profile, $C_n^2$.

# II. Background

## 2.0 Introduction

A review of relevant theory and published research relevant to the exploration of measurement techniques for retrieving the refractive index structure parameter, $C_n^2$, is presented. Key accomplishments are grouped into three subject areas, methods for directly measuring the refractive index structure parameter, methods for inferring the refractive index structure parameter, and models used for describing the refractive index structure parameter. Previous direct measurements of $C_n^2$ have involved coherent LIDAR systems. Not producing a profile, but also a direct measurement, prior research has involved measuring the Fried parameter for an integrated atmosphere. Indirect methods for inferring $C_n^2$ are numerous and include balloon born or satellite sounding based in situ measurements of weather parameters, wind profiling LIDARs, multi-laser guide star sensing used for slope detection and ranging (SLODAR), imaging shadow patterns in scintillation (SCIDAR and MASS), image differential motion characterization, and acoustic sounding radar based techniques. Lastly, models used for describing $C_n^2$ include weather parameter based approaches, model fitting to in situ data, Zernike polynomial based wavefront representation. After reviewing the published works in the three categorized subject areas, a trend is shown that points to a lack of unique novel means for obtaining direct measurements of $C_n^2$, and a plethora of indirect measurement schemas and modeled assumed values. This identifies a need for further research that aims at obtaining direct measurements of $C_n^2$.

The refractive index structure parameter, $C_n^2$, is a measure of the varying strength of optical turbulence as a function of distance. The distance is often expressed as an altitude as there are strong variations in the strength of the turbulence creating a changing profile as a function of altitude. The variation assumed can span multiple orders of magnitude and depending on the model used can create disagreement in results. This creates a need for a direct measurement system. The

following background summary of published works provides a basis for the types of measurement schemas used for measuring, characterizing, and predicting the strength of atmospheric turbulence, and will lead into the innovative sensing architecture proposed as the topic for this dissertation.

## 2.1 Methods for Measuring Cn2

Directly measuring $C_n^2$ involves gaining knowledge of the phase disturbances along slant path ranges. This has previously been done utilizing a coherent Light Detection and Ranging (LIDAR) based system. Alternative approaches measure an integrated volume $C_n^2$ which results in a measurement of $r_0$, the Fried parameter. Systems measuring the Fried parameter utilize guide stars at fixed ranges whether produced by a laser or by naturally occurring starlight. These techniques are well known and have been documented in various published works. The traditional techniques utilizing laser guide stars have evolved into research programs aimed at multi-range, multi-source laser beacons. Knowledge of direct measurement techniques have provided the basis for developing a technique as an alternative means for providing measurements of $C_n^2$.

Utilizing coherent LIDAR techniques, turbulence strength has been measured for slant path ranges up to 2.2 km by the research group at Montana State University. Proven by the ability of a coherent LIDAR to synthesize synthetic aperture LIDAR-based images, the phase of the range profile is deterministic and is sensitive to optical phase perturbations imparted by atmospheric turbulence along the path. This measurement scheme works by utilizing the resolved range of point features of the target, retro-reflectors for this experiment, and estimating the mutual coherence between each pair by calculating the complex correlation coefficient over an averaging period. Combining all pairs and using the known spacing of the target features an estimate of the wave structure function, *D(r)*, is determined. This estimate of the wave structure function is fit to standard

turbulence parameters such as the Fried parameter, $r_0$, or the refractive index structure parameter, $C_n^2$. The sampling of the wave structure function is limited to the array of target features. Consequently, a small array limits turbulence measurement sensitivity whereas a widely space array leads to saturation of the mutual coherence function caused by wrapped phases for target pairs with separation larger than the coherence width. Therefore, for this measurement scheme to function a balance has to be constructed that separated the target features but keeps them within a coherence width of the atmosphere. For testing, this technique was used in a horizontal configuration and a constant refractive index structure parameter was assumed for the path. [63, 64]

The Center for Astronomical Adaptive Optics at the University of Arizona has been researching a dynamic refocus system for increasing the signal to noise ratio of multi-height beacons that are aimed to be applied to the Multi-Mirror Telescope (MMT) and Magellan telescope. This is a system that is designed to refocus a large telescope system in order to reduce aberrations for Rayleigh beacons in the range of 20 to 30 km. The effect of a dynamic refocus system is shown in Figure 01. It is noted that the goal is to keep the focused spot of the returned laser lights as a small as possible spot seen in the detector plane. [22]

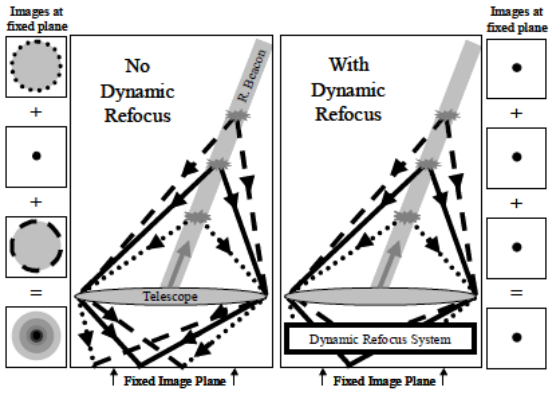


Fig. 01. Illustration showing the concept and benefit of a dynamic refocus system

Keeping the spot at focus as light travels through a larger range of altitude from a single pulse allows for more photons to return to the sensing system as compared to a traditional range gate technique. This technique would have the disadvantage of having inaccuracies of sensing high level aberrations, however, if this concept is used in conjunction with a multi conjugate adaptive optics systems, a tomographic solution can be produced for aberrations in layers from different heights. Thus the benefit of an increased photon return can be utilized and supports multi-laser beacon systems. Initial designs involve a pattern of five beacons that are phase locked and launched simultaneously. The goal is to hold all five beacons in focus as they rise in height together. For the MMT system this requires a change in focus of 113 microns which corresponds to approximate movement of 320 waves. The output from a Zemax model shows the optical components involved in achieving a dynamic refocus system as shown in Figure 02. [21]

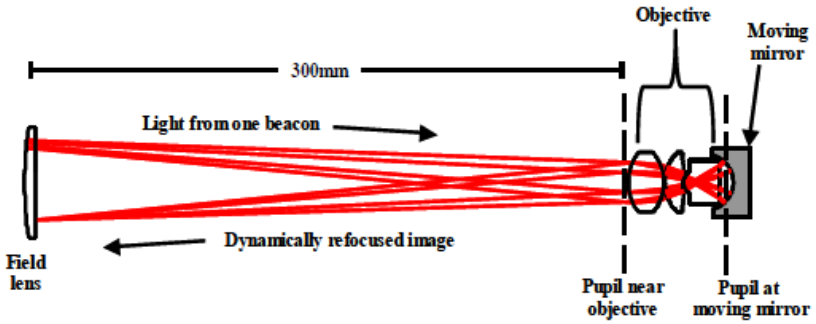


Fig. 02. Zemax model of the dynamic refocus system concept

Utilizing a similar set of theoretical calculations as part of the design of the dynamic refocus beam system, the concept of a dynamic Rayleigh beacon system can be realized. The difference is in the implementation. The dynamic refocus system aimed at increasing SNR by allowing for a longer depth of the atmosphere to be used to produce a focused spot on the sensor, effectively increasing

the number of photons available. The dynamic Rayleigh beacon system utilized different heights from a single beacon measured on subsequent pulses. One challenge that will have to be overcome as noted by the dynamic refocus system is the need to keep a focused spot on the detector for multi-range beacons.

## 2.2 Methods for Inferring $C_n^2$

Many methods for inferring $C_n^2$ exist and there is a wide diverse body of research from many research organizations and university programs. Presented here is a subset of the body of research that aims to cover the major sensing techniques to include balloon born or satellite sounding based in situ measurements of weather parameters, wind profiling LIDARs, multi-laser guide star sensing used for slope detection and ranging (SLODAR), imaging shadow patterns in scintillation (SCIDAR and MASS), image differential motion characterization, and acoustic sounding radar based techniques.

An early work that aimed to characterize atmospheric turbulence strength scaling with altitude was published by R. Hufnagel in 1974. This worked examined the spatial and temporal variations of the parameters of atmospheric turbulence, $C_n^2(h,t)$, mainly focused above Earth's boundary layer with the goal of constructing a heuristic model for the dynamic $C_n^2(h,t)$ profile. For this Hufnagel utilized available experimental evidence and connected that to physically reasonable mathematical processes. Data used included $C_n^2$ profiles collected by Bufton's balloon born in situ measurements of temperature fluctuations, NOAA acoustic sounder data, Vinnichenko and Dutton temperature fluctuation data, Hardy's high power radar echoes, and numerous observations of stellar scintillation. From these data sets Hufnagel draws conclusions into understanding the various turbulence related effects as they relate to physical phenomenon. The temperature fluctuations

provided insight into large fluctuations around a mean value and the behavior of the profile fit a lognormal random distribution. Scintillation data provided variance statistics and was related to the weighted path integral of $C_n^2$. From a year's worth of data Hufnagel concluded that the variance approximately fit the profile of a Gaussian random variable with a standard deviation of 2.1. Based on these observations from the data Hufnagel synthesized a model for $C_n^2(h,t)$ that is valid for altitude regimes from 3000m to 24000m. This model is

$$C_n^2 = \left\{\left[(2.2 \times 10^{-53})h^{10}\left({}^{W}/_{27}\right)^2\right] exp\left({}^{-h}/_{1000}\right) + (10^{-16}) exp\left({}^{-h}/_{1500}\right)\right\} exp[r(h,t)] \quad (1)$$

where $h$ is in meters above sea level, $r$ is a zero mean homogeneous Gaussian random variable, and $W$ is a normal distribution random variable with average of 27 meters per second and a standard deviation of 9 meters per second for Maryland based data. The values of W will be different for different terrain types. From this model Hufnagel provided the sample profile shown in Figure 03. [41]

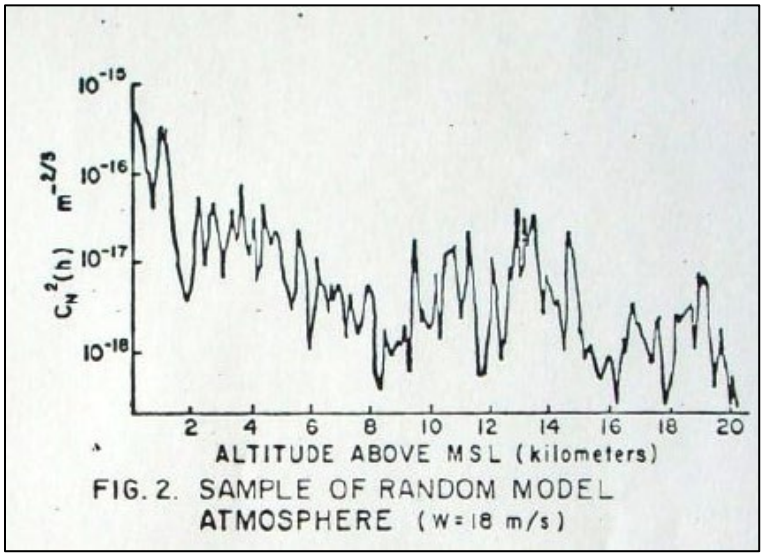


Fig. 03. Sample of a typical $C_n^2$ profile using the random atmosphere model with W=18 m/s

To extend the theory and measurements done by Hufnagel, a wavelet transformation based approached has been established. This method estimates $C_n^2$ by vertical scaling characteristics of temperature and pressure fields. The needed input temperature and pressure fields can be readily obtained from various means such as weather balloons, satellite based sounding, or atmospheric generated models. Using this framework, the spatial-temporal variations in the turbulence strength can be captured. For this a study was completed using thermosonde collected data near Bradshaw Air Force Base which had a vertical resolution of approximately 10 m starting at an elevation of 4120m to avoid adverse effects of local mountains. This method uses Tatarski's derived method for estimating the temperature structure parameter, $C_T^2$ which is defined as

$$C_T^2 = c_0 L_0^{4/3} \left(\frac{d\bar{\theta}}{dz}\right)^2 \tag{2}$$

where $L_0$ is the outer scale of turbulence, $c_0$ is a constant assumed to be 2.8, and the ratio of theta to z is proportional to the mean potential temperature representative at a height above the ground. From the temperature structure parameter it is straight forward to calculate the index of refraction structure parameter using the Gladstone relationship which is

$$C_N^2 = \left(7.9 \times 10^{-5} \frac{P}{T^2}\right)^2 C_T^2 \tag{3}$$

where $P$ is the atmospheric pressure and $T$ is the temperature. With the exception of the outer scale all variables are readily available through radiosonde measurements. The outer scale is stated to be estimated from temperature profiles as well as utilizing the Thorpe scale. These inputs are the basis for the wavelet based approach proposed by Basu. It is known that temperature profiles from radiosonde data do not resolve the temperature inertial range. To circumvent this Basu utilizes the buoyancy-range inherent scaling of the temperature profile. Doing this with a weighted neighboring sampling schema provides added resolution into the temperature data. During this scaling Basu applies a local energy (square of the wavelet coefficients) parent scale to the child

scale. This preserves the buoyancy range spectral slope. After this process, the temperature data is at a finer resolution than the outer range of the turbulence outer scale. Then $C_T^2$ is estimated using the following equation

$$\langle\Big(\big(\theta(z-\Delta z)\big)-\theta(z)\Big)^2\rangle = C_T^2(\Delta z)^{2/3} \tag{4}$$

where the angle brackets denote ensemble averaging. Since there exists a stochastic nature of the down sampling threshold on a single coarsely measured profile, many fine resolution profiles can be generated resulting in a realization for $C_T^2$. [45]

The next methods of deducing $C_n^2$ are based off of differential image motion (DIM). The first method utilizes a light detection and ranging (LIDAR) system and the second is based off of passive imagery measurements. Georgia Tech Research Institute developed what they call a DIM LIDAR. A DIM LIDAR is a hybrid of two well established techniques, a differential image motion monitor which uses light from natural stars to deduce the Fried parameter, $r_0$, and laser guide star adaptive optics which create an artificial beacon at a fixed altitude by ranging an outgoing laser pulse synched to a camera. By moving the fixed beacon height to a range of altitudes an inversion algorithm can be used to retrieve the $C_n^2$ profile. The DIM technique measures the differential wavefront tilt of two spatially separated apertures. In the focal plane changes in tilt correspond to image motion. The variance between subsequent measurements is used as the metric to deduce $r_0$. This method relies on 10 minutes of averaging to deduce $C_n^2$ strength values from ground level to approximately 10km. The model used to as the basis for the inversion is

$$\sigma_{DIM}^2 = f(d/D)D^{-1/3}\bar{C}_n^2 \tag{5}$$

where $f(d/D)=33.2[0.358-0.242(d/D)^{-1/3}]$, $D$ is the sub-aperture diameter, $d$ is the sub-aperture separation, and the path integrated turbulence is defined as

$$\bar{C}_n^2 = \int_0^S C_n^2(s)\left(1-\frac{s}{S}\right)^{\frac{5}{3}} ds \tag{6}$$

where S is the distance to the laser guide star. For this system four sub-apertures were used in an equally spaced circular configuration to measure the differential tilt. Additionally, in order to go from differential tilt measurements that provide the image tilt variances a weighting function has to be assumed. The weighting function assumed for this technique is shown in Figure 04. Note that since the turbulence structure function is non-negative, the variance will always be constant or increasing. This weighting function is used to smooth the $C_n^2$ profile that is produced.

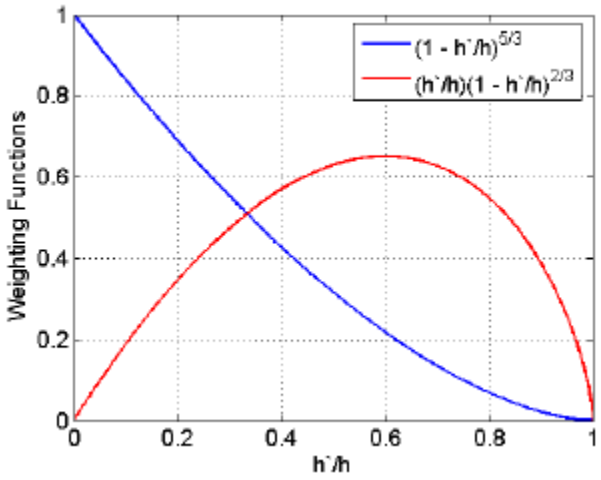


Fig. 04. Weighting functions used for DIM LIDAR method

A testing campaign was conducted with this system and for an instance at White Sands Missile Range during the daytime an $HV_{5/7}$ profile was calculated through the inversion as shown in Figure 05. [16]

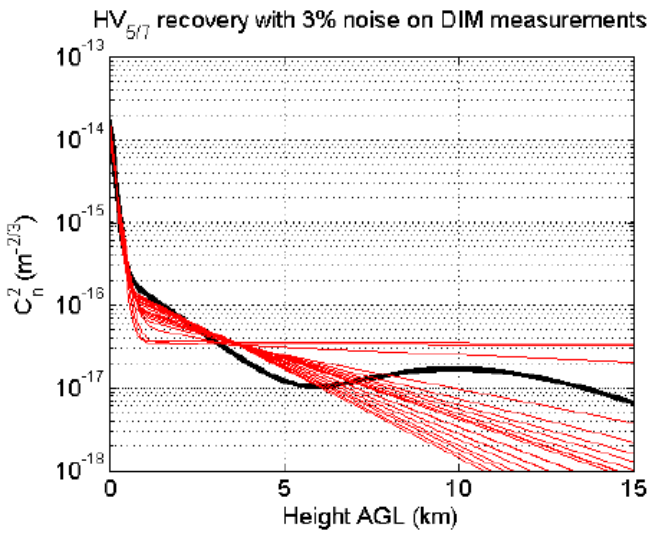


Fig. 05. Retrieval of $HV_{5/7}$ profile from experimental test data

A similar implementation of the DIM algorithm called Delayed Tilt Anisoplanatism (DELTA) was implemented by the company MZA. They developed an imaging system algorithm that uses a feature detection algorithm within an image and then uses the frame rate of the camera to derive differential motion between the jittering feature pairs. The feature pairs act similarly to the sub-apertures in the GTRI technique and are the basis for the turbulence strength profile measurement. The advantage of the DELTA system is that it is completely passive thus requiring no laser safety concerns. In order for the DELTA algorithm to work there needs to be a sufficient number of detectable features within scene that create separation diversity in the measurements. The separation diversity is what creates the range profile. An example of the DELTA system with output from one of the measurement campaign is shown in Figure 06. [38]

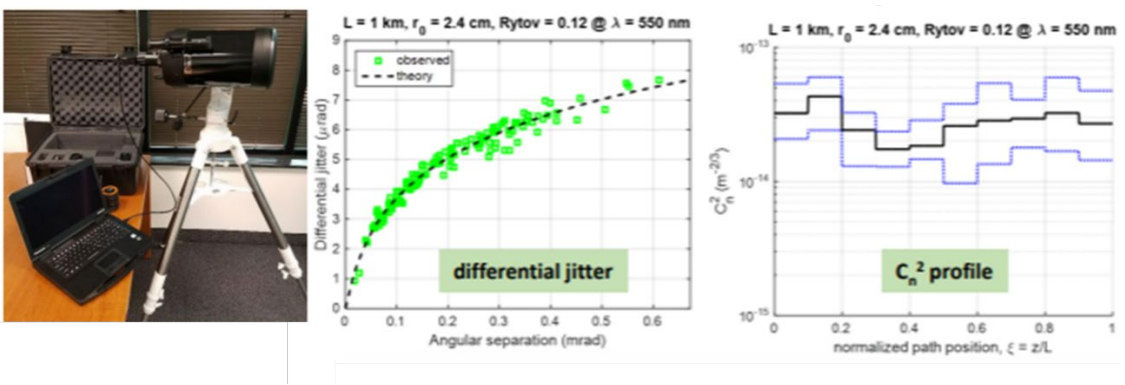


Fig. 06. (left) DELTA system and example outputs of (middle) differential jitter measurements and (right) calculated $C_n^2$ profile

The DELTA system has been configured into a DELTA-Sky variant under an AFRL SBIR contract. The DELTA-Sky configuration utilizes a small telescope looking at the moon or star fields. Features from craters on the moon or star fields act as the features used for calculating the differential jitter. Since the system is looking up at the night sky the algorithm is constrained to a 30km assumed altitude. This is a fair assumption as the major turbulence effects above this altitude will not be captured well by the base DELTA algorithm. [9]

The Air Force Institute of Technology has investigated a similar treatment for estimating turbulence strength along the viewing path from time lapse imagery. The use of weighted $C_n^2$ and $r_0$ functions are inferred from differential motion from extended features within the viewing scene. This method is phased based and therefore could be applied to extended ranges. The approach used by the Air Force Institute of Technology utilizes a set of derived path weighting functions that drop to zero on both ends with the peak location depending on the size of the imaging system and the relative size separations of the features whose motions are being tracked. The weighting functions can be linearly combined in such a way that the results can mimic those produced by a scintillometer. Good agreement between time-lapse imagery based estimates of $C_n^2$ and a scintillometer were

shown in multiple experiments coving multiple ranges and target types. This showed the feasibility of using this technique for estimating the refractive index structure parameter. [47, 23]

A third method for deducing the strength of the refractive index structure parameter is implemented in the Gemini multi-conjugate adaptive optic system and is called slope detection and ranging (SLODAR). This technique utilizes five separate Shack-Hartmann wavefront sensor systems each pointing to a laser guide star and then reconstructs wavefronts for a deformable mirror based on these slope measurements combined with data from a wind LIDAR. This implementation of the SLODAR technique is able to profile atmospheric turbulence into 16 distinct layers spanning altitudes from 0 to 19km. SLODAR based algorithms work by estimating the turbulence strength at different altitudes by cross-correlating the information from two stars measured on a single Shack-Hartmann wavefront sensor. The geometry involved along with the cross-correlation strengths based on slope measurements is what provides insight into the layered strength of atmospheric turbulence. The multi guide star and sensor implementation here is an adaption of a conventional SLODAR system but utilizes the optimized multi-beacon geometry and sensor system to provide layered turbulence strength estimates over a wider viewing area. This system has also been enhanced by knowledge gained from data collected from a wind profiling LIDAR which provides influence for a time-delayed cross-correlation measurement between different sensors.

The underlying mathematics that provide the range information in a SLODAR system rely on optical triangulation utilizing spatial covariance of slope data from individual lenslets in a Shack-Hartmann wavefront sensor system. The layer height is defined in a SLODAR system by $h = md/\theta sec\xi$ where $m$ is an integer that identifies the bin, $d$ is the sub-aperture size, $\theta$ is relative angular separation and $\xi$ is the zenith angle. Additionally, the separation of layers can be calculated

by $\delta h_m = dz^2\theta/(z\theta + md)^2$ where $z$ is the propagation range. The geometrical configuration for a SLODAR system is shown in Figure 07.

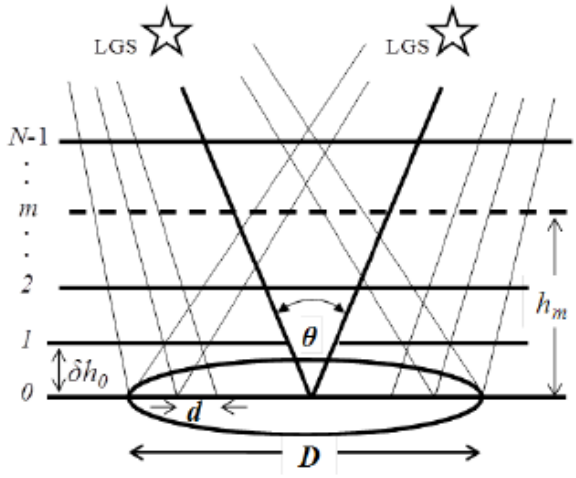


Fig. 07. Geometry for a SLODAR system

For this system proper averaging was needed to extract the low order turbulence modes from the covariance matrices. This resulted in approximately 10,000 frames of data required for an accurate measurement. Since this system also utilizes laser guide stars there is a cone effect present in the geometry. This manifests itself as a stretching in the binned profile for the refractive index structure parameter. Relating this back to the Fried parameter, $r_0$, and the integrate tilt variance, $\sigma_d^2$, the turbulence strength can be derived as

$$r_0 = \left[.423k^2 sec\xi \int_0^H C_n^2(z)dz\right]^{-\frac{3}{5}} \tag{7}$$

$$C_n^2(m)\delta h_m = \frac{1}{.423k^2 sec\xi}\frac{r_0(m)^{-\frac{5}{3}}}{\rho_m} \tag{8}$$

$$\rho_m = 1 - \frac{h_m}{z} \tag{9}$$

$$\sigma_d^2 = .179\lambda^2 r_0^{-\frac{5}{3}} d^{-\frac{1}{3}} \tag{10}$$

$$C_n^2(m)\delta h_m = \frac{2.37\omega_m}{sec\xi}\sigma_0^2 \tag{11}$$

Utilizing these equations and data taken by the Gemini system initially this technique has obtained agreeable results with other models and techniques. More data is currently being collected to understand the technique's capability to estimate turbulence over the Gemini site in varied turbulence conditions. [1]

A fourth method involves the use of scintillation from astronomical sources as seen by a multi-aperture system. This type of system is called Multi-Aperture Scintillation Sensor (MASS). A MASS utilizes spatial scintillation properties to reconstruct low altitude turbulence profiles. This technique is able to deduce the strength of the turbulence in vicinity of the telescope depending on the size of the source or separation if using a field of sources. The induced scintillation contributed from different layers in the atmosphere can be detangled in systems known as SCIDARs. However a SCIDAR has a couple problems which lead to the development of the MASS. A SCIDAR requires a suitably bright double star seen from a greater than 1m telescope. The MASS can use extended sources like planets or the moon. Traditionally, large objects such as a planet will average out the scintillation. However, a MASS system can sense weak contributions from scintillation from lower altitudes making the use of planets or the moon possible. The spatial spectrum of a light wave passing through weak phase screens over a propagation distance, $z$, is

$$\Phi_\chi(f) = 0.0229 r_0^{-5/3} |f|^{-11/3} sin^2(\pi \lambda z |f|^2) \tag{12}$$

where the spectrum of the intensity fluctuations (scintillation) is $\Phi_I = 4\Phi_\chi$, $f$ is the two dimensional spatial frequency, and $r_0^{-5/3} = 0.423(2\pi/\lambda)^2 C_n^2 dz$ which is the Fried parameter where $C_n^2$ is the turbulent layer refractive-index fluctuation. Using this knowledge the framework for a scintillation based metric is deduced from the differential scintillation index as

$$s_k^2 = \int W_k(z) C_n^2(z) dz \tag{13}$$

where $W_k(z)$ is a weighting function that is assumed based on the size of the aperture combination and size of the source used. The principle of a MASS device is shown in Figure 08.

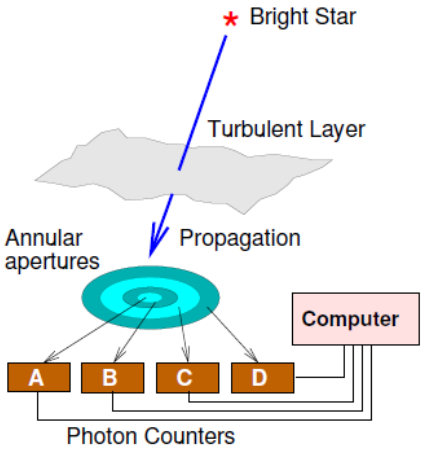


Fig. 08. Principle for a MASS

Inherently in the design of this device a differential image motion monitor (DIMM) measurement system is possible. Therefore most MASS devices can also be a DIMM device which is an added benefit and provides a comparator for the deduced turbulence profile produced. [7]

The last methodology presented here will be for obtaining measurements of $C_T^2$ from sound detection and ranging measurements (SODAR). For this a calibrated Doppler SODAR from a research aircraft can be used. The Doppler SODAR has the ability to take in situ observations of the temperature and velocity fluctuations when within the inertial range of turbulence. These measurements produce SODAR observations of the temperature and velocity fluctuation variances and consequently the turbulent energy dissipation and temperature variance destruction rates. Initial experiments conducted using SODAR had the goals of measuring $C_T^2$ as well as evaluating

the existence or non-existence of an inertial subrange in which SODAR signals would scatter at elevation.

The Doppler SODAR system used by Penn State for retrieving $C_T^2$ is a configurable system that can be tailored to the feature or region being probed. General characteristics include an operating frequency of 700 to 4000 Hz, pulse lengths of 10 to 200 ms, bandwidths of 10 to 100 Hz, pulse repetition frequencies of 1 to 10 Hz. Tri-static Doppler receivers are used for obtaining the phase-coherent measurements. The theory to obtain atmospheric turbulence induced structure functions relies on Kolmogorov spectrum assumptions. The general equation to get from the acoustic power, $\sigma(\theta,r)$, to a structure function is

$$\sigma(\theta,r) = 0.03k^{1/3}cos^2\left[\left(\frac{C_V^2(r)}{C^2}\right)cos^2(\theta/2) + 0.13(C_T^2(r)/T^2)\right]sin(\theta/2)^{-11/3} \quad (14)$$

where $k$ is the wavenumber, $\theta$ is the scattering angle, and $r$ is the range. The sound velocity and temperature of the scattering volume are $C$ and $T$, respectively. The power at range SODAR equation can be written as

$$P(r) = P_0\frac{A_r C_\tau}{2r^2}\sigma(\pi,r)exp\left[-2\int_0^r \alpha(r)dr\right] \quad (15)$$

where $P_0$ is the radiated power, $A_r$ is the received aperture area, $C_\tau$ is the scattering volume length, and $\alpha(r)$ is the attenuation coefficient. Assuming a constant attenuation to the range of interest the temperature structure function can be calculated as

$$C_T^2(r) = 265.5\frac{r^2\lambda^{1/3}}{A_r C_\tau}T^2e^{2\alpha r}\frac{P(r)}{P_0}. \quad (16)$$

Utilizing this treatment, SODAR has the capability to study the spatiotemporal behavior of atmospheric turbulence in the lower atmosphere. Altitude resolutions are limited to approximately 300 m above a ground or tower based test, however when utilizing outfitted research aircraft this altitude limitation can be lifted allowing for SODAR to be an effective means for probing spatial effects of the structure functions associated with atmospheric turbulence. [13]

## 2.3 Models used for Describing $C_n^2$

Cherubini and Businger discuss the mathematical formulation of the refractive index structure parameter which is based on a hydrostatic assumption. This formulation leads to inaccuracies in the profile at higher altitudes as compared to profiles generated from potential temperature. For this treatment of atmospheric turbulence the atmosphere is considered to be locally homogeneous and isotropic for the sub-regions of the atmosphere between the large eddies that serve as the energy source for turbulence and the small-scale eddies that serve as the viscous effect. This region is the inertial subrange. Dimensional analysis from Kolmogorov showed that the structure function in this region follows a two-thirds power law and the refractive index structure parameter can be considered a measure of the strength of the small-scale turbulence. The inertial subrange can also be defined as the region between the inner and out scales as shown in Figure 09.

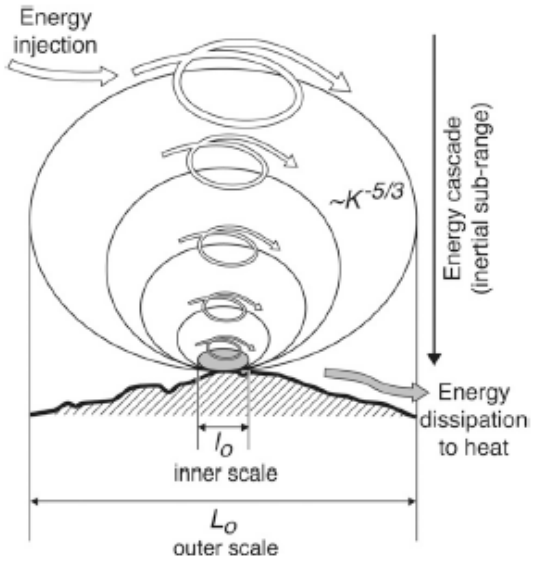


Fig. 09. Illustration of the cascading turbulence process depicting the spatial wavenumber (K) energy insertion, inertial subrange, and energy dissipation.

Outside the inertial subrange the Kolmogorov treatment of isotropic turbulence is no longer valid. Additionally inside the inertial subrange the refractive index is correlated which has led to the development of the Tatarski based relations. [60, 61] Moreover, many atmospheric parameters of importance have been developed based on these frameworks such as the Fried parameter, the isoplanatic angle, and the refractive index structure parameter. The relation of the refractive index structure parameter to the temperature structure parameter for astronomical applications is

$$C_n^2(z) = \left(\frac{80\times10^{-6}p}{T^2}\right)^2 C_T^2(z). \tag{17}$$

Cherubini and Businger point out deficiencies and propagated errors with these approaches especially for the formulation of parameters involving calculations derived from above the lower tropopause. To mitigate this the use of potential temperature in the denominator and derivative in the refractive index structure parameter is suggested to be used. This results in the following modification to the refraction index structure parameter which now becomes

$$C_n^2(z) = \left(\frac{80\times10^{-6}p}{T\vartheta}\right)^2 C_\vartheta^2(z) \tag{18}$$

where $C_\vartheta^2(z) = a^2(K_H/K_M)L_0^{4/3}(\delta_\vartheta/\delta_z)^2$. This equation provides a constant structure for the potential temperature and no approximations were needed for its derivation. Using this formalism for the development of the refractive index structure parameter removes the assumption that the atmosphere is in hydrostatic equilibrium resulting in a more robust definition. This new definition was evaluated against a SCIDAR based case study in Hawaii in 2002 and resulted in rough agreement. This refractive index structure parameter correction in the derivation will aid in providing increased validity to measurements quantifying the strength of turbulence in the upper atmosphere. [57]

The Air Force Institute of Technology has advanced the Tatarski based model for calculation of $C_n^2$ from $C_T^2$ by showing that the inclusion of pressure perturbations are an important factor in the equation. The general expressions provided by Tatarski [61] for $C_n^2$ and $C_T^2$ is

$$C_n^2 = 2.8\frac{K_H}{K_M}\left(79\times10^{-6}\frac{P}{T^2}\right)^2 L_0^{\frac{4}{3}}\left(\frac{dT}{dz}+\gamma_d\right)^2 \tag{19}$$

$$C_T^2 = 2.8\frac{K_H}{K_M} L_0^{\frac{4}{3}}\left(\frac{dT}{dz}+\gamma_d\right)^2 \tag{20}$$

where $L_0$ is the outer scale of turbulence, $P$ is pressure, $T$ is temperature, and

$$\frac{K_H}{K_M} = \begin{cases} \frac{1}{7R_i} & for\ R_i \geq 1 \\ \frac{1}{6.879R_i+\frac{1}{1+6.873R_i}} & for\ 0.01 < R_i \leq 1 \end{cases} \tag{21}$$

where $R_i$ is the gradient Richardson number which indicates the stability of the atmosphere. [24] The problem with this model for environments that consist of naturally buoyant well mixed turbulence layers is that $C_T^2$ is derived from the dry adiabatic lapse rate. For naturally buoyant layers the dry adiabatic lapse rate is close to the actual lapse rate which makes $C_n^2$ very small. This will inherently underrepresent the actual turbulence strength. To remove this assumption and take into account pressure perturbations the calculation that takes $C_n^2$ from $C_T^2$ becomes $C_n^2 = a^2\frac{K_H}{K_M}L_0^{\frac{4}{3}}\left(\frac{dnd\theta}{dTdz}+\frac{dndp}{dPdz}\right)^2$. Here the potential temperature gradient term has the dominant contribution for optical turbulence, but the additional terms accounting for atmospheric pressure is non-zero. Using this approach a robust weather parameter based model for estimating the strength of atmospheric turbulence can be obtained. [48]

Other common turbulence models are based off of scaling terms applied to fitted models such that the resultant profile matches well with data collected. To account for discrepancies between the models and measured data random variable scaling terms were also used as an uncertainty multiplier. A common turbulence strength model of this type is

$$C_n^2(h) = A\left[2.2 \times 10^{-53} h^{10} \left(\frac{w}{27}\right)^2 exp\left(-\frac{h}{1000}\right) + 1 \times 10^{-16} exp\left(-\frac{h}{1500}\right)\right] + Bexp\left(-\frac{h}{100}\right) \quad (22)$$

with $A = exp[r(h,t)]$ where *r* is a Gaussian random variable with zero mean; *h* is the height, *t* is the time, $w^2 = \left(\frac{1}{15km}\right)\int_{5km}^{20km} v^2(h)dh$; where *v(h)* is the wind speed in meters per second at altitude *h*.

For average turbulence A = 2.7; B controls the surface layer turbulence. A generalized model is

$$C_N^2(h) = Aexp\left(-\frac{h}{H_A}\right) + Bexp\left(-\frac{h}{H_B}\right) + Ch^{10} exp\left(-\frac{h}{H_C}\right) + Dexp\left(-\frac{(h-H_D)^2}{2d^2}\right) \quad (23)$$

where *A* is the coefficient for the surface boundary layer turbulence strength, $H_A$ is the height for its 1/e decay, *B* and $H_B$ similarly for the troposphere (up to 10km), *C* and $H_C$ define the peak turbulence in the tropopause, *D* and $H_D$ define one or more isolated layers of turbulence, with *d* being the layer thickness. Common Constants for various models are shown in Table 01. [31]

Table 01. Constants used as inputs into the generalized model for specific turbulence models

| Model | A (E-15) | $H_A$ (m) | B (E-17) | $H_B$ (m) | C (E-53) | $H_C$ (m) | D (E-16) | $H_D$ (m) | FWHM (arcsec) | $r_0$ (m) | $\theta_0$ (arcsec) |
|---|---|---|---|---|---|---|---|---|---|---|---|
| **Hufnagel** | 0 | | 27 | 1500 | 5.94 | 1000 | 0 | | 1.15 | .11 | 1.1 |
| **HV 5-7** | 17 | 100 | 27 | 1500 | 3.59 | 1000 | 0 | | 2.5 | .05 | 1.4 |
| **HV 10-10** | 4.5 | 100 | 9 | 1500 | 2.0 | 1000 | 0 | | 1.26 | .10 | 2.1 |
| **HV 15-12** | 2.0 | 100 | 7 | 1500 | 1.54 | 1000 | 0 | | 0.84 | .15 | 2.5 |
| **Mauna Kea (1)** | 0 | | 1 | 3000 | 1.63 | 1000 | 0 | | 0.36 | .34 | 2.4 |
| **Maun Kea (2)** | 0 | | 1 | 3000 | 1.63 | 1000 | 1 | 6500 | 0.53 | .24 | 1.9 |

## 2.4 Conclusion

There is a body of research that aims to quantify the strength of atmospheric turbulence. Upon review, there are only a few methods of directly measuring the turbulence strength and many strategies for deducing the strength of the turbulence from measurement of other associated parameters such as atmospheric weather parameters like temperature. Additionally, there are a few base modeling strategies. These are based off of observed weather phenomenon or fit data to site specific measured values. These provide a good basis and give insight into the scale strength of atmospheric turbulence.

After surveying these methods it has become apparent that there is a need for additional methods that directly measure the strength of the atmospheric turbulence along the observing path. This is the aim of the research presented as part this dissertation. Utilization of the strength of observing the sensed wavefront was used as a direct measure of the integrated turbulence. Then there was a need to take the integrated measurement and quantify the at range turbulence strength value. The presented method in the following sections takes varied integrated volume measurements in rapid rate so that they can be directly compared to each other in order to produce a measure of the path resolved turbulence strength. The implementation of a novel system that does this is described in the methodology section and builds upon the mathematical treatment presented in the theory section.

# III. Theory

## 3.0 Introduction

This section describes some of the required theoretical background involved in understanding atmospheric turbulence, quantifying the strength of atmospheric turbulence, modeling atmospheric turbulence induced wavefront distortions, and design of a measurement system aimed at quantifying the profile of the turbulence strength. Base theory starts with understanding the mechanism for turbulence generation and the influencing functions of the atmosphere. Next a common model for characterizing turbulence is presented. This is the Kolmogorov model. Aspects of the Kolmogorov model are presented as they relate to an optical wave propagating through the atmosphere. This leads to metric parameters that describe the atmospheric turbulence. Next the subject of wavefront sensing is analyzed for multiple approaches and then applied to specific methods that will be used in the design of a Rayleigh beacon system. Lastly, the system components requirements are described for a Rayleigh beacon system.

## 3.1 The Atmosphere

### *3.1.1 Composition*

The atmosphere is comprised of seven primary layers, the troposphere, the tropopause, the stratosphere, the stratopause, the mesosphere, the mesopause, and the thermosphere. The troposphere and tropopause are the regions where a Rayleigh beacon system operates and will be the focal region of the atmosphere relevant to the research presented. The troposphere extends up to 11 km above Earth's surface and contains approximately 75% of the atmospheric mass of Earth. In general, the maximum air temperature is at the Earth's surface and decreases with altitude. The

tropopause is the next layer that extends up to 20 km. Here the air temperature remains fairly constant. These two layers together are considered the lower atmosphere. [32]

Turbulence within the atmosphere is mainly considered to be present in thin localized layers where wind shear is present. During the day turbulence is strongest near the ground as a response to solar heating and thermal currents. At night, surface turbulence is low and disturbances are present at higher altitudes as a result of wind shear. [31]

### *3.1.2 Modeling the Atmosphere*

For treatment and measurement of atmospheric turbulence refractivity is one of the most important under lying concepts. Refractivity is the departure of the refractive index from a value of one and is highly dependent on the composition of the atmosphere to include the presence of $CO_2$ and water vapor. For optical wavelengths it can be approximated by the temperature pressure relationship as *N=77.6P/T*. For dry air the refractivity can be modeled as

$$N_S(\lambda) = 8.34213 \times 10^{-5} + \frac{2.40603\times10^{-2}}{130-\lambda^{-2}} + \frac{1.5997\times10^{-4}}{38.9-\lambda^{-2}} \tag{24}$$

where $\lambda$ is the wavelength in microns. [31] This can be derived from Edlen formulation of the dispersion formula for standard air. This formula is

$$(n-1)_S \times 10^8 = 8342.13 + 2406030(130-\sigma^2)^{-1} + 15997(38.9-\sigma^2)^{-1} \tag{25}$$

where $\sigma^2$ is the vacuum wavenumber in microns$^{-1}$. This formula can be transformed into a dependence on pressure in torr, $p$, and temperature in $^{o}$C, $t$. This formula was found in the laboratory [14] and can be approximated by

$$(n-1)_{TP} = (n-1)_S \times 0.00138823p/(1+0.003671t). \tag{26}$$

The second major effect on atmospheric turbulence is the wind. A general model for the wind velocity is based on a Gaussian average model and is defined as

$$v(z) = v_G + v_T exp\left[-\left(\frac{zcos(\zeta)-H_T}{L_T}\right)^2\right][sin^2\phi + cos^2\phi cos^2\zeta]^{1/2} \quad (27)$$

where $v_G$ is the wind velocity at low altitude, $v_T$ is the wind velocity at the tropopause, $\zeta$ is the zenith angle of observation, $H_T$ is the height of the tropopause, $L_T$ is the thickness of the tropopause layer, and $\varphi$ is the wind direction relative to the telescope's azimuth direction. The wind speed models and turbulence models derived from the refractivity model are used to generate turbulence parameters that are required for adaptive optics systems. [31]

## 3.2 Atmospheric Turbulence

*3.2.1 Base theory*

There are three basic phenomenon that affect optical wave propagation through the atmosphere. These are absorption, scattering, and refractive-index fluctuations. Absorption and scattering give rise to attenuation of the optical wave, whereas refractive-index fluctuations lead to fluctuations in the irradiance distribution, beam spreading, and a loss of spatial coherence of the optical wave. Scattering is a critical concept that forms the basis for the returned laser energy from a Rayleigh beacon system. Scattering is strongly dependent on wavelength and the size of the scatters determines the type of scattering that takes place. Rayleigh scattering is caused primarily by air molecules and haze that are small compared to the wavelength of light that is propagating. The second type of scattering is Mie scattering, also called aerosol scattering. This is when the scattering particle is comparable to the size of the light wavelength. Rayleigh scattering is typically considered to be isotropic whereas Mie scattering is strongly concentrated in the forward direction.

Refractive index fluctuations give rise to wave front distortions. These distortions in the optical wave result in beam spread which is beyond what is expected from pure diffraction and a random redistribution of the beam energy within the cross-section of the beam. This redistribution of energy is regarded as irradiance fluctuations and is the most well-known of the phenomenon as it can be seen in the twinkling of the stars. Atmospheric turbulence also works towards degrading spatial coherence as a light wave propagates. The loss of spatial coherence limits the ability to focus or collimate a laser beam which results in a reduction of received power. Additionally, heterodyne detection receivers are sensitive to the loss of spatial coherence since the spatial coherence effectively limit the size of the detection system's collecting aperture. [32]

*3.2.2 Kolmogorov Model*

In 1941 Kolmogorov proposed a model for the velocity of motion in a fluid medium which is used to explain the observed phenomenon of atmospheric turbulence. This model assumes energy is added to the system in the form of large scale disturbances, referred to as the "outer scale", which then breaks down into smaller scale structures. The process of turbulent flow is when the Reynolds number exceeds a critical number that is dependent on the physical structure of the flow system. The Reynolds number is defined as $Re=V_0L_0/\upsilon_0$, where $V_0$ is the characteristic velocity, $L_0$ is the character size of the flow, and $\upsilon_0$ is the kinematic viscosity of the fluid. For air $\upsilon_0$ is typically $15 \times 10^{-6}\ m^2/s$. With normal values of 15 m for the scale size and 1 m/s for the velocity the Reynolds number is $1 \times 10^6$ which greatly exceeds the critical value, making the atmosphere almost always turbulent.

The main source of energy input for the atmosphere is solar heating which introduces energy over a large range of input sizes. During the day, energy comes from local convection from the heating of Earth's surface, while at night, the energy source is the mixing of air at different temperatures at

various altitudes due to the wind. The turbulent flow kinetic energy transfer continually breaks down into smaller and smaller scales in an energy cascade until it reaches another critical value in the Reynolds numbers, which is referred to as the "inner scale". At the inner scale the kinetic energy is dissipated as heat by viscous friction and the turbulent motion fades away. Under the Kolmogorov treatment for turbulence the relation between the inner and outer scale is defined as $(Re)^{3/4} = L_0/l_0$. This shows that the larger the velocity of the flow is the larger the Reynolds number will be and thus the smaller the inner scale of turbulence will be.

The power spectrum of atmospheric turbulence is deduced from the dimensional relationship governed by the velocity fluctuations and scale sizes. The spatial wave number of a turbulent eddy of scale size $l$ is defined as $\kappa=2\pi/l$. The spectral density of a fluctuation, $\Phi(\kappa)$, of an energy increment is proportional to the velocity fluctuations squared, which leads to Kolmogorov power spectrum

$$\Phi(\kappa) \propto \kappa^{-5/3} \tag{28}$$

which is only valid within the inertial range for $L_0>l>l_0$. [31]

Structure functions in turbulence theory are mainly used to describe the spatial characteristics of the medium. Kolmogorov treatment for turbulence is dependent on the thermal properties associated with the physical process of turbulence. Therefore a temperature based structure function is used as defined as $D_T(r) = C_T^2 r^{2/3}$, where $C_T^2$ is the structure parameter for temperature and $r$ is the separation distance. Temperature fluctuations affect the density of air and therefor influence the refractive index, $n$. The refractivity of air can be closely approximated by $N=(n-1)10^6=77.6P/T$, where $P$ is the atmospheric pressure in millibars and $T$ is the atmospheric temperature in Kelvin. For vertical propagations pressure perturbations are mainly smoothed out

so mainly the temperature fluctuations are considered. There changes in the refractivity are described as $\delta N=-77.6(P/T)\delta T$. Thus, the structure function for the refractive index variations is $D_n(r) = C_n^2 r^{2/3}$, where $C_n^2$ is the refractive index structure parameter. This leads to the power spectrum for the refractive index variations to be

$$\Phi_N(\kappa) \propto 0.033 C_n^2 \kappa^{-11/3}. \quad (29)$$

The Kolmogorov treatment for atmospheric turbulence has limitations. It is assumed to be an incompressible medium. Also, it is only valid within the inertial subrange between the inner and outer scales. These scales are subject to debate. The inner scale can vary from 1mm near the ground to 1cm at the tropopause, and the outer scale is subject to much discussion, but is generally viewed as being 1m to more than 100m. For astronomical systems the outer scale is what determines the overall size of the tilt seen by a telescope. Lastly, Kolmogorov turbulence relies on a basic physical mechanism for which the turbulence strength generation is considered to be smooth in response to energy input or output. There is evidence that this is not the case and that there are often intermittent conditions in which small scale structures of turbulence create microbursts. This effect is not captured in the averaged treatment of using the 5/3's power laws. [31]

*3.2.3 Modeling Turbulence with Zernike Polynomials*

Kolmogorov turbulence is well suited for treatment by means of Zernike polynomials since it is a continuously smooth varying representation of optical wavefronts. Zernike polynomial representation of optical wavefronts allow for complex two-dimensional wavefronts to be decomposed into a set of orthogonal mode basis functions of ascending order. The lowest of the Zernike polynomials are recognizable aberration functions such as piston, tilt, defocus, and astigmatism. Zernike polynomials are able to more accurately represent a wavefront than a zonal approach (array of flat sub-apertures) which have a similar number of degrees of freedom. Zernike

polynomials are defined in polar coordinates on a unit circle as a function of azimuthal frequency *m* and radial degree *n*, where $m \leq n$ and *n-m* is even. The set of Zernike polynomials is defined as

$$Z_{even} = \sqrt{n+1} R_n^m(r) \sqrt{2} cos(m\theta), \quad m \neq 0 \tag{30}$$

$$Z_{odd} = \sqrt{n+1} R_n^m(r) \sqrt{2} sin(m\theta), \quad m \neq 0 \tag{31}$$

$$Z_{even} = \sqrt{n+1} R_n^0(r), \quad m = 0, \tag{32}$$

where

$$R_n^m(r) = \sum_{S=0}^{(n-m)/2} \frac{(-1)^S (n-S)! r^{n-2S}}{S! \left[\frac{(n+m)}{2} - S\right]! \left[\frac{(n-m)}{2} - S\right]!}. \tag{33}$$

An arbitrary phase function, $\varphi(r,\theta)$, can be expanded into Zernike coefficients as

$$\phi(r,\theta) = \sum_0^\infty a_j Z_j(r,\theta), \tag{34}$$

where $a_j$ is the strength of the Zernike component. [31]

*3.2.4 Mutual Coherence Function and Von Karman spectrum*

The mutual coherence function (MCF) can be used to predict the spatial coherence radius at the receiver plane. This MCF is derived under the assumption of a Kolmogorov spectrum which for a spherical wave corresponds to

$$\Gamma_2(p,r,L) = \frac{1}{(4\pi L)^2} exp\left(\frac{ik}{L} pr - 4\pi^2 k^2 L \int_0^1 \int_0^\infty \kappa \Phi_n(\kappa)[1 - J_0(\kappa\xi\rho)] d\kappa d\xi\right) \tag{35}$$

where $L$ is the propagation path length, $k$ is the wave number, $p$ is the propagation parameter, $r$ is the transverse position of the observation point, $\kappa$ is the scaler spatial wave number, $\Phi$ is the spatial power spectrum of the refractive index and $J$ is a Bessel function.

This under the assumption of a Kolmogorov spectrum reduces to

$$\Gamma_2(p,r,L) = \frac{1}{(4\pi L)^2} exp\left(\frac{ik}{L}pr - \frac{3}{8}\left(\frac{qk\rho^2}{L}\right)^{5/6}\right)$$
$$= \frac{1}{(4\pi L)^2} exp\left(\frac{ik}{L}pr - 0.55C_n^2k^2L\rho^{5/3}\right), \qquad l_0 \ll \rho \ll L_0 \tag{36}$$

where $q = 1.22(\sigma_R^2)^{6/5}$ which is a measure of the irradiance fluctuations based on the Rytov variance, ρ is the spatial coherence radius, $C_n^2$ is the refractive index structure parameter, $l_0$ is the inner scale of the turbulence, and $L_0$ is the outer scale of the turbulence. The loss of spatial coherence can be deduced from the modulus of the complex degree of coherence (DOC) which is of the form

$$DOC(r_1,r_2,L) = \frac{|\Gamma_2(r_1,r_2,L)|}{\sqrt{\Gamma_2(r_1,r_1,L)\Gamma_2(r_2,r_2,L)}}$$
$$= exp\left(-.5D(r_1,r_2,L)\right) \tag{37}$$

where $D(r_1,r_2,L) = Re[\Delta(r_1,r_2,L)]$ is the wave structure function (WSF). For a spherical wave the WSF is

$$D_{sp}(\rho,L) = 8\pi^2k^2L\int_0^1\int_0^\infty \kappa\Phi_n(\kappa)[1 - J_0(\kappa\rho\xi)]d\kappa d\xi. \tag{38}$$

The spherical wave WSF can be reduced using the von Karman spectrum. The von Karman spectrum is a model that takes into account inner and outer scale turbulence effects applied to the Kolmogorov power law spectrum model. The spherical wave WSF using the von Karman spectrum approximately reduces to

$$D_{sp}(\rho,L) = 1.09C_N^2k^2Ll_0^{-1/3}\rho^2\left[\frac{1}{\left(1+\rho^2/l_0^2\right)^{1/6}} - 0.72(\kappa_0 l_0)^{1/3}\right]. \tag{39}$$

For the case where the outer scale is viewed as infinity, the spherical wave spatial coherence radius is

$$\rho_0 = \rho_{sp} = \begin{Bmatrix} \left(0.55C_N^2k^2Ll_0^{-1/3}\right)^{-1/2}, & \rho_{sp} \ll l_0 \\ (0.55C_N^2k^2L)^{-3/5}, & l_0 \ll \rho_{sp} \ll L_0 \end{Bmatrix}. \tag{40}$$

In some cases the spatial coherence is related to a similar value, the atmospheric coherence width $r_0$, which is defined as $r_0 = 2.1\rho_0 = \left[0.423sec(\xi)k^2 \int_{h_0}^{H} C_N^2(h)dh\right]^{-3/5}$. Alternatively, we can simplify the relation by combining terms with the definition of atmospheric coherence width to show that the spatial coherence is

$$\rho_0 = \left(\frac{cos\xi}{1.45k^2 \int_{h_0}^{H} C_N^2(h)dh}\right)^{3/5}. \tag{41}$$

Here we can see the influence of the atmospheric structure parameter,$C_N^2$, as it relates to the spatial coherence involved. [32]

*3.2.5 Metric parameters induced by the atmosphere*

Metric parameters of interest to describing turbulence or turbulence effects include: turbulence coherence length, the Strehl ratio, the mean square angle of arrival fluctuations, angular anisoplanatism, and the Greenwood frequency. The atmospheric coherence width, $r_0$, known as the Fried parameter is a measure of the effective aperture of an imaging system. The Fried parameter is defined as

$$r_0 = \left[0.423sec(\xi)k^2 \int_{h_0}^{H} C_n^2(h)dh\right]^{-3/5}. \tag{42}$$

It is built on the integral of the refractive index structure parameter. The Fried parameter also describes the number of degrees of freedom required by an adaptive optics corrector.

The Strehl ratio is defined as the ratio of the actual peak intensity of a point source to the diffraction limited peak intensity of that point source through the same telescope. The Strehl ratio is expressed as $S = \exp(-\sigma^2)$ where $\sigma^2$ is the mean-square wavefront error in the optical beam. The Strehl ratio is a useful metric when the imaging performance is near the diffraction limit. However, if the

wavefront is severely distorted such as that of an uncompensated image through strong turbulence the Strehl ratio becomes a less meaningful metric.

The mean square value of the angle of arrival fluctuations of an optical wavefront can be described as a tilt when the size of the collecting aperture is on the order of the Fried parameter or smaller. The mean square of the angle of arrival fluctuations is described as

$$\sigma_\alpha^2 = 0.18\lambda^2 D^{-1/3} r_0^{-5/3}, \tag{43}$$

where $\lambda$ is the wavelength of light, $D$ is the aperture diameter, and $r_0$ is the Fried parameter which is the turbulence coherence length. [31]

Angular anisoplanatism degrades all imaging systems that have a finite field of view. For an adaptive optics system it is usually caused by the three dimensional distribution of atmospheric turbulence along the propagation path. The metric of merit for this is the anisoplanatic angle which is defined as

$$\theta_0 = \left[2.914k^2(sec\zeta)^{8/3} \int_{h_0}^{H} C_n^2(h) h^{5/3} dh\right]^{-3/5}. \tag{44}$$

Angular anisoplanatism is most sensitive to disturbances located at long distances from the imaging system. For astronomical scenarios this means it is the turbulence at higher altitudes.

The characteristic frequency of atmospheric turbulence is known as the Greenwood frequency and is given by

$$f_G = \left[0.102k^2(sec\zeta) \int_0^{\infty} C_n^2(h) v^{\frac{5}{3}}(h) dh\right]^{\frac{3}{5}} \tag{45}$$

$$f_G = 0.427 \frac{v}{r_0} \tag{46}$$

The greenwood frequency is determined by the wind velocity and the atmospheric turbulence. This is a measure of temporal effects of the changing atmosphere. [31]

*3.2.6 Turbulence regimes*

Optical turbulence is generally divided into two regimes, weak fluctuations and strong fluctuations. Weak fluctuations are based on the Rytov perturbation approximation which yields simple mathematical models that characterize statistical quantities involving the optical wave. The theories that are based off the Rytov perturbation approximation impose strict limitations that are based on the assumed magnitudes of the irradiance fluctuations. Strong fluctuation theory has evolved from several different approaches such as the Huygens-Fresnel principle, but will not be presented within this research effort.

When using the Kolmogorov spectrum for plane or spherical waves that have propagated through sections of the atmosphere it is customary to distinguish between the strong and weak turbulence regimes by using the Rytov variance which is defined as

$$\sigma_R^2 = 1.23 C_N^2 k^{7/6} L^{11/6}. \tag{47}$$

Weak fluctuations are typically associated with $\sigma_R^2 < 1$ and are associated with unbounded fluctuations in irradiance of a plane wave. [32]

## 3.3 Wavefront Sensing

*3.3.1 Wavefront sensing*

There are two major forms of wavefront sensing, direct and indirect. Direct wavefront sensors determine the shape of the wavefront in the optical pupil. There are two basic measurement schemas for doing this, zonal and modal. Zonal sensing measures the slope vector of the wavefront

in continuous segments within the pupil. This principle is to deconstruct the wavefront into simple segments that can be easily measured. The zones are sized such that the predominant distortion in each zone is wavefront tilt. This is the basis for a Shack-Hartmann wavefront sensor. Modal sensing on the other hand divides the wavefront into distinct surface shapes such as tilt, defocus, and astigmatism. These surface shapes are then sensed independently. These surface shapes become the basis for a Zernike polynomial decomposition representation of the wavefront. It is possible in processing to go back and forth between zonal and modal measurement styles. Direct wavefront sensing utilizing a Shack-Hartmann wavefront sensor will be the focus of this research.

Indirect wavefront sensing are schemes that measure a related effect and then deduce the wavefront errors. Common practices for indirect sensing usually involve measuring the intensity distribution in the image plane. Here the image plane contains information found in the pupil plane average across the whole aperture. These types of techniques usually utilize a deconvolution from image intensity or some sort of aperture tagging system that feeds into a wavefront analyzer. These processes can become computationally intensive especially when the aberrations become large and high order. Also, there is a hard to mitigate effect of spatial invariance induced when taking a Fourier transform to perform deconvolution which can be hard to overcome. These schemas for indirect sensing are known, but are not considered as part of the research system design utilizing the dynamically ranged Rayleigh beacon.

*3.3.2 Shack-Hartmann wave front sensor*

A Shack-Hartmann wavefront sensor is simple in design and acts as a zonal gradient sensor that measures induced wavefront tilt in localized regions. This is done by placing an array of identical lenses in the pupil plane of an optical system. This array of lenses is continuous over the pupil plane and is sized to match localized wavefront tilts. This array of lenses produces a series of

focused spots that are sensed on a detector. The location of these spots will change on a detector based upon the tilt present in each individual lens. This deviation from center for each lens is what is measured and converted into a gradient measurement. This gradient measurement provides knowledge of the wavefront tilt in a localized region and can be stitched together to show a continuous wavefront that is produced by zonal tilts.

The mean square tilt induced on each lens can be calculated based on knowledge of the atmospheric turbulence, $r_0$, and sensing system properties such as the operating wavelength, $\lambda$, and the aperture size, $d$. The equation for this is

$$\sigma_\alpha^2 = 0.182 \left(\frac{d}{r_0}\right)^{5/3} \left(\frac{\lambda}{d}\right)^2. \tag{48}$$

This leads to a sub-aperture size of $d=1.21r_0$. As an example, if the expected Fried number is 7 cm then the projected aperture size on the optical pupil of the system should be 8.47 cm.

To optimize the design of a Shack-Hartmann wavefront sensor a common metric is the standard deviation of the one-axis measurement error. This measurement error is a product of the SNR, turbulence effects, and source size. The resultant equation is

$$\sigma_\phi = \frac{\pi^2 K_g}{4(SNR)} \left[\left(\frac{3}{2}\right)^2 + \left(\frac{\theta d}{\lambda}\right)^2\right]^{\frac{1}{2}} \qquad for\ r_0 > d \tag{49}$$

$$\sigma_\phi = \frac{\pi^2 K_g}{4(SNR)} \left[\left(\frac{3d}{2r_0}\right)^2 + \left(\frac{\theta d}{\lambda}\right)^2\right]^{1/2} \qquad for\ r_0 < d \tag{50}$$

where $K_G$ is typically between values of 1.2 and 1.5 and is a factor that accounts for increases in spot displacement at nulls in the system. For a two-axis system the total error is $\sqrt{2}$ times the standard deviation value for a one-axis system.

### *3.3.3 Other forms of wavefront sensing*

An alternate form of direct wavefront sensing is a shearing interferometer. Shearing interferometry is a technique that measures the phase difference in optical wavefronts. A shearing interferometer operates on the principle of taking an original wave and interfering it with a displaced version of itself. Then the phase differences are converted into intensity differences and can be measured. This is typically done with an optical grating. The grating generates sheared replicas of the pupil at the detector plane. Wavefront gradients in the pupil create the intensity differences. These differences are measured and the wavefront tilts are then calculated.

Curvature sensors also exist and are another means of directly measuring the wavefront. An example of a device consists of an optical mask in the pupil plane. This mask creates a sharp intensity gradient at its edges. Changes in wavefront curvature produce convergent or divergent rays of the normally parallel beams created by the mask. This results in radial displacement of the edges of the beams and also changes the average intensity of the beams. In the simplest form, two detectors are placed at detector planes on opposite sides of the focal plane. Local changes in wavefront tilt produce opposite polarity at the two planes, and the ratio of the intensities at the two planes corresponds to wavefront curvature. A series of local wavefront curvatures are sensed and then stitched back together as tilts to directly measure the incoming wavefront. [31]

## 3.4 Turbulence Effects on Spatial Coherence

### *3.4.1 Introduction*

When flow of a medium exceeds a critical Reynolds number the flow changes from laminar to turbulent. Turbulent air motion represents a set of eddies or various sizes between the inner and outer scales. Between the inner and outer scales inertial forces influence the breakup of larger

eddies into smaller ones. This is known as the inertial range and is the concentration of turbulence sensing.

Optical wave propagations are greatly affected by the small fluctuations in the refractive index. This effect leads to beam spreading, loss of spatial coherence, angle of arrival fluctuations, beam wander, phase fluctuations, and irradiance fluctuations. In general when propagating an optical wave through a random medium, the first and second order moments of the optical field are of interest. The first moment, mean field, is associated with the part of the wave energy that passes through the turbulent medium without distortion. This is the coherent part of the field and takes the form

$$\langle U(r,L)\rangle = U_0(r,L)exp\left(-.39C_N^2k^2L\kappa_0^{-5/3}\right) \tag{51}$$

where $U_0$ is the optical field in absence of turbulence. The second moment of the field determines the spatial coherence and mean irradiance. The mutual coherence function for a spherical wave is

$$\Gamma_2(p,r,L) = \frac{1}{(4\pi L)^2}exp\left[\frac{ik}{L}p\cdot r - .5D(\rho,L)\right] \tag{52}$$

where $D(\rho,L)$ is the wave structure function.

*3.4.2 Structure function*

The wave structure function for a spherical wave through distributed turbulence is known to be

$$D_{sp}(\rho,L) = 1.093k^2\rho^{5/3}\int_0^L C_n^2(z)dz \quad for\ l_0 \ll \rho_{sp} \ll L_0. \tag{53}$$

From this, the spatial coherence radius can be deduced for spherical waves which is

$$\rho_{sp} = \left[1.46k^2\int_0^L C_N^2\left(\frac{z}{L}\right)^{5/3}dz\right]^{-3/5} \quad for\ l_0 \ll \rho_{sp} \ll L_0. \tag{54}$$

Similar results can be concluded for plane or Gaussian beam waves, however since the returning light from the point beacon will be spherical in nature, the spherical wave calculations are the ones that are most relevant to this research.

The root-mean-square (rms) angle of arrival behind a lens of radius $W_G$ and focal length $f$ can be calculated as

$$\sqrt{\langle \beta_a^2 \rangle} = \sqrt{2.91 C_N^2 L (2W_G)^{-1/3} [1 - 0.81(2\kappa_0 W_G)^{1/3}]} \quad where\ 2W_G \gg l_0. \tag{55}$$

For a spherical waves under weak turbulence the scintillation index is calculated as

$$\sigma_I^2(L) = 8\pi^2 k^2 L \int_0^1 \int_0^\infty \kappa \Phi_n(\kappa) \left\{1 - cos\left[\frac{L\kappa^2}{k}\xi(1-\xi)\right]\right\} d\kappa d\xi. \tag{56}$$

Which leads to

$$\sigma_I^2(L) = \beta_0^2 = 0.4\sigma_R^2 \tag{57}$$

for the Kolmogorov spectrum. [32]

## 3.5 Dynamic Rayleigh Beacon Components

### *3.5.1 Introduction*

The design of a turbulence profiling direct measurement system consists of a beam launch system and a sensor system. The theory behind the beam launch system is to send laser energy out into the atmosphere such that the backscattered energy can be viewed as a point source. This means that the beam has to be sufficiently small at range and that there needs to be enough energy in the sensed backscattered laser light.

### *3.5.2 Beam launch system*

The governing equation that optimizes the beam launch system is the standard deviation of the measurement error in a Shack-Hartmann wavefront sensor which is restated here as

$$\sigma_\phi = \frac{\pi^2 K_g}{4(SNR)}\left[\left(\frac{3}{2}\right)^2 + \left(\frac{\theta d}{\lambda}\right)^2\right]^{\frac{1}{2}} \tag{58}$$

for measurements sized for measuring localized tilts on each sensor sub-aperture. This equation accounts for the extended size of the projected beam. When the beam is small it can be viewed as a point source and the number of photons enabling detection is summed up in an SNR term. SNR is defined to be

$$SNR = \frac{n_p}{\sqrt{n_p + N_D\left(n_B^2 + \left(\frac{e}{G}\right)^2\right)}} \tag{59}$$

where $n_p$ is the detected photoelectrons per sub-aperture, $N_D$ is the detector pixels per sub-aperture, $n_B$ is the number of background electron per pixel, $e$ is the read noise, and $G$ is the intensifier gain. The detected photoelectrons can be calculated from the LIDAR equation which is

$$N(z) = \left(\frac{E\lambda}{hc}\right)(\sigma_B n(z)\Delta z)\left(\frac{A_R}{4\pi z^2}\right)(T_o T_A^2 \eta) + N_B \tag{60}$$

where $N(z)$ is the expected number of photo detected electrons in the range interval $\Delta z$, $E$ is the laser energy per pulse, $\lambda$ is the wavelength, $h$ is Plank's constant, $c$ is the velocity of light, $\sigma_B$ is the effective backscatter cross-section, $n(z)$ is the number density of scatters in range $z$, $A_R$ is the area of the receiving aperture, $T_o$ is the transmission of the optical components, $T_A$ is the transmission of the atmosphere, $\eta$ is the quantum efficiency of the photodetector, and $N_B$ is the number of background and noise photoelectrons. The Rayleigh backscatter cross-section and atmospheric density product is given by

$$\sigma_B n(z) = 3.6 \times 10^{-31}\frac{P(z)}{T(z)}\lambda_L^{-4.0117} \tag{61}$$

where $P$ is the atmospheric pressure at range $z$ in millibars and $T$ is the atmospheric temperature at range in K. The optimum angular size of a beacon can be determined by the size of the effective

aperture which can be viewed as $d$ from the telescope sub-aperture or $r_0$ induced by the atmosphere. This is expressed as

$$\Delta\alpha = 2.44\frac{\lambda}{d}. \tag{62}$$

For a typical value of $d$ of 7 cm and wavelength of 550 nm this results in an angular size of 19.17 microradians. [31]

*3.5.3 Sensing system*

The sensing system consists of a telescope aperture, an optical shutter, and a Shack-Hartmann wavefront sensor which consists of a lenslet array and a camera. The telescope aperture defines the pupil plane size of the total sensed area. In order to reconstruct a wavefront the telescope aperture needs to be multiple lengths of $r_0$ across. Typical values of $r_0$ are approximately 7-12 cm for imaging scenarios involving ground to space wave propagation in visible wavelengths. The optical shutter needs to be fast enough to create a sharp cutoff of the returning optical light and also have enough blocking power to not allow the near field light into the system. One way to do this is to use a Pockels cell as an optical shutter. The Pockels cell is made of a polarization rotating crystal controlled by a high voltage power source and two linear polarizers placed on both sides of the crystal. Returning laser light is polarized matched to the crystal by the first polarizer and 90 degrees out of phase to the second polarizer. This creates light blockage. When high voltage is applied to the Pockels cell the polarization of the optical wave is rotated by 90 degrees allowing light to pass through the system. The last piece of the sensing system is the Shack-Hartmann wavefront sensor. This consists of a lenslet array that is size matched to the expected turbulence strength to be sensed as seen in the telescope's pupil plane. The camera needs to have capabilities to measure low light signals with minimal noise. This is needed since backscattered photons entering the sensing system are low in number.

# IV. Design Methodology, Laboratory Testing, and System Integration

## 4.0 Introduction

The design goal was proposed a new methodology for measuring the strength profile of optical turbulence along the viewing path of an optical system. The methodology utilized a Rayleigh beacon with a Shack-Hartmann sensor based architecture in order to obtain a direct measurement of the optical wavefront entering the collecting aperture. However, this concept only provides a path integrated measurement. So, an alternative implementation of a Rayleigh beacon was developed that allowed for fast changes in the beacon's range on a pulse by pulse basis. In changing the range of a Rayleigh beacon on a pulse by pulse basis many design challenges were considered. In changing the range of a point source created by the laser there could possibly be a movement in the focus position in the sensing system. An engineering solution for mitigating this had to be developed. A fast optical shutter that was controllable needed to be identified as a commercial part or had to be created from purchasable parts. The system had to operate quickly enough that the atmosphere would be considered frozen so that differencing subsequent measurements was mathematically justifiable as an algorithm technique for determining the profile strength of atmospheric turbulence. Lastly, when dealing with backscattered light aiming at measuring a profile across the collection aperture, the SNR of the system had to be carefully determined. All components in the optical system for both beam projection and wavefront sensing had to be carefully designed and implemented in order to perform the low light level sensing that is needed.

The methodology associated with this dissertation can be divided into two major tasks. The first was to properly choose and optimize the components needed to create a dynamic range Rayleigh beacon. The basis for this was further constrained by cost as the Air Force Research Laboratories were sponsoring this, and a fixed budget for hardware components was imposed. So in choosing

the system components a balance between cost and performance was implemented as part of the design optimization. Within cost constraints, a design was achievable that could meet the goal as a proof of concept system used as a prototype demonstrator for collecting data. The second task was to design the sensing algorithm. This utilized the direct measurements of the wavefront from a Shack-Hartmann sensor sensed from the dynamic changes in beacon geometry of the system to produce range resolved measurements of atmospheric turbulence strength. The system design considerations, laboratory testing of components, and measurement methodology are discussed in subsequent sub-sections within the Methodology chapter. Additionally, some initial challenges that have been overcome in the early stages of implementing this research are also presented.

## 4.1 System Design Considerations

Moving from concept to system design there were many topics that were considered which had influence on part selection. The first and most interconnected was system signal to noise ratio (SNR). The SNR can be divided into two major functional areas, photons sensed and noise. Noise is specific to camera specifications and the environment, but is assumed to generally be 33 photo-electrons per sub-aperture which is reasonable for most mid-grade cameras for our scenario. Photons sensed can be estimated using the LIDAR equation on the outgoing beam and then scale that number by the various optical transmissions in the system. The mathematical basis for this was provided in the theory section. Many laser were considered initially for this and the generalized sensing system used was a 0.6096 m telescope with 100 sub-apertures representing a 10 by 10 grid sub-aperture array. The results from the three best candidate laser systems is shown in Table 02.

Table 02. Parameters of top three laser source candidates optimized for 10km range

| Parameter | DP-532-8 | DP-527-8 | DP-532-4 |
|---|---|---|---|
| **Pulse energy (mJ)** | 8 | 8 | 4 |
| **Repetition rate (Hz)** | 1000 | 200 | 1000 |
| **Pulse width (ns)** | 20 | 10 | 20 |
| **Beam quality ($M^2$)** | 1.3 | 2.0 | 1.3 |
| **Cooling type** | Water | Air | Water |
| **Price ($K)** | 95 | 45 | <95 |
| | | | |
| **Performance Parameters** | | | |
| **Pixel variance** | 0.94 | 1.0 | 1.8 |
| **Launch radius (cm)** | 4.7 | 5.8 | 4.7 |
| **Number of photons per sub-aperture** | 250 | 257 | 125 |

Based on cost and performance the DP-527-8 laser by Photonics Inc. was chosen. Do note that the number of photons per sub-aperture was calculated for 100 sub-apertures spread across the input aperture. This is fairly pessimistic in terms of the transmissions used for the optical elements in the system. The most significant loss was due to Malus Law, 50%, from converting unpolarized light to polarized light. Having photon levels around 250 per sub-aperture is good as it will result in a detectable signal with an SNR of approximately 7.6. There are also many opportunities left open in the design that will result in a higher SNR such as better performance camera, higher throughput optical components, and reduction in the number of sub-apertures.

To optimize the design, components were chosen to feed into the standard deviation of the one-axis measurement error. Restated here, this measurement error is a product of the SNR, turbulence effects, and source size. The equation used is

$$\sigma_\phi = \frac{\pi^2 K_g}{4(SNR)}\left[\left(\frac{3}{2}\right)^2 + \left(\frac{\theta d}{\lambda}\right)^2\right]^{\frac{1}{2}} \qquad for\ r_0 > d \tag{63}$$

$$\sigma_\phi = \frac{\pi^2 K_g}{4(SNR)}\left[\left(\frac{3d}{2r_0}\right)^2 + \left(\frac{\theta d}{\lambda}\right)^2\right]^{1/2} \qquad for\ r_0 < d \tag{64}$$

where $K_G$ is typically between values of 1.2 and 1.5 and is a factor that accounts for increases in spot displacement at nulls in the system. The SNR was calculated as

$$SNR = \frac{N}{\left[N + n_{pix}(\sigma_r^2 + \sigma_{BG}^2)\right]^{1/2}} \tag{65}$$

N is calculated from the LIDAR equation and accounts for the number of photo-detected electrons for each sub-aperture. The equation used is

$$N_{PDE} = \eta T_t T_r T_{atm}^2 \frac{A_{sub}\beta_{BS}\Delta l E_p \lambda}{R^2 hc} \tag{66}$$

The spot size is calculated at range and then simply converted into an angular diameter to feed into the optimization equation. The spot size calculation is

$$\omega_R(z) = \omega_0 \sqrt{1 + \left(\frac{M^2 \lambda z}{\pi \omega_0^2}\right)^2} \tag{67}$$

Using these equations, the resultant performance metrics are shown in Table 02 for the top three laser source candidates. All three choices result in workable designs, however the DP-527-8 performs well and has the lowest cost. The result from this optimization for the selected components yielded a curve with an inflection point as shown in Figure 10.

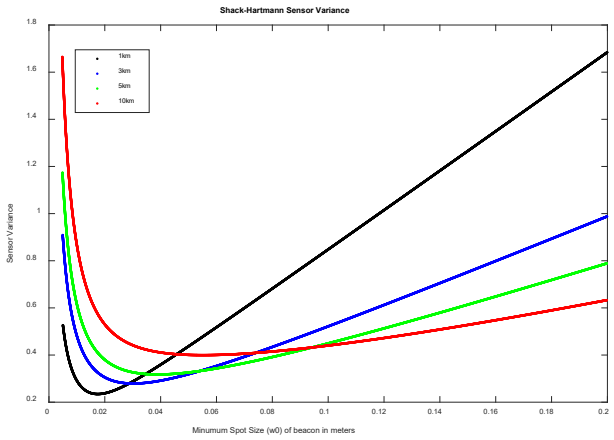


Fig. 10. Optimization of the DP-572-8 laser source

Shown in Figure 10 is the optimization of the chosen laser source utilizing a 10 by 10 Shack-Hartmann wave front sensor and nominal system parameters. The key take away from this plot is that the optimization parameter remains at a small value for most operation designs and as the beacon is pushed farther from the source the design becomes more robust. Also, all optimal launch radius sizes are achievable as there is a maximum launch radius available on the candidate telescope system of 7.62 cm. It is important to check the photon return values for these ranges which resulted in 1660, 553, 332, and 166 photo-electron per sub-aperture for ranges of 1km, 3km, 5km, and 10km respectively. These are all favorable photon levels as they will result in detectable SNRs as summed noise levels can be assumed to be around 33 photo-electrons for camera used when operated in normal conditions in an uncooled fashion.

Another component of the design was to design the specifics of the Shack-Hartmann sensor. A summary of the chosen Shack-Hartmann wavefront sensor design is shown in Figure 11. [59] This sensor was built, tested and installed as part of the sensor system for the dynamic range Rayleigh beacon. Screen captures for laboratory based component testing of the Shack-Hartmann sensor are

shown in Figure 12. As part of the design for the Shack-Hartmann wave front sensor the wave front passed from the input of the telescope had to be considered. A simple Zemax model of the optical layout was created and is shown in Figure 13. The Zemax model shows the light rays that travel through the system and are imaged on the Shack-Hartmann wave front sensor. The resultant optical field is flat to within a 0.05 waves for a plane wave input. This shows a design for light routing to the camera that is possible and will not distort the measurements.

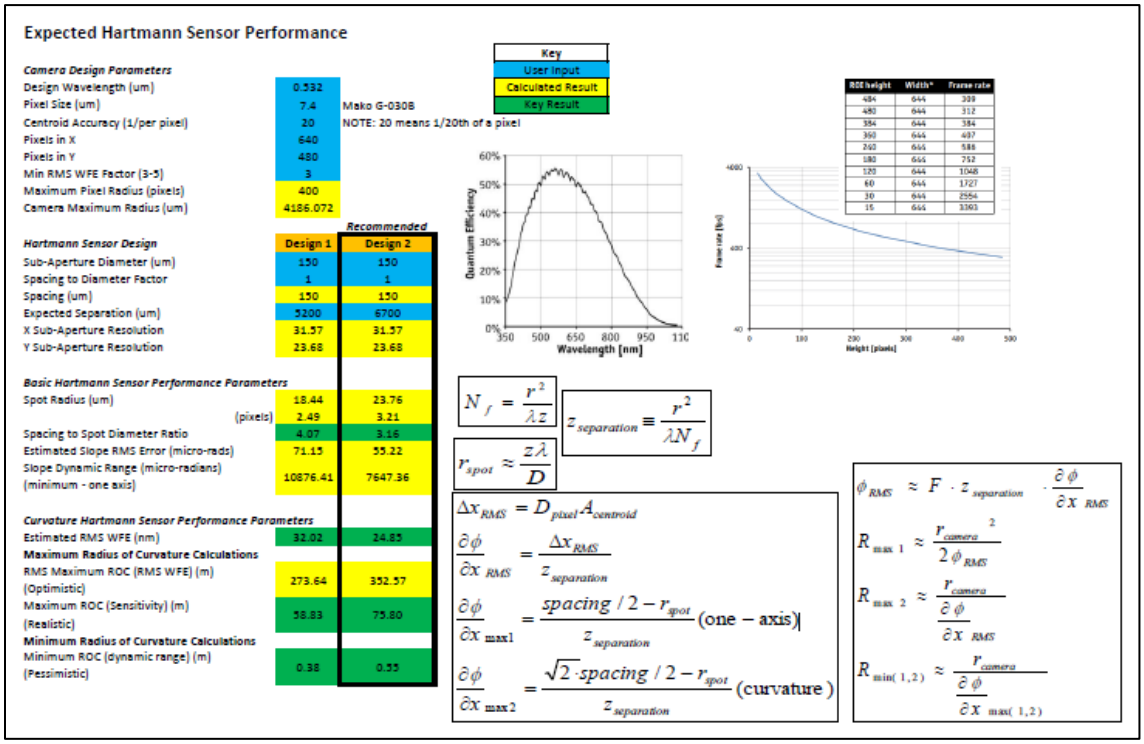


Fig. 11. Summary of Shack-Hartmann wavefront sensor design

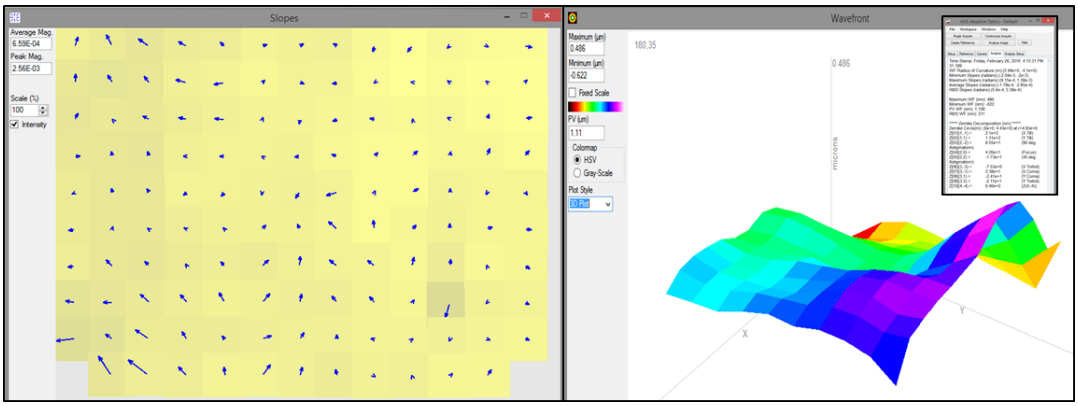


Fig. 12. Screen capture from component testing of the Shack-Hartmann wave front sensor

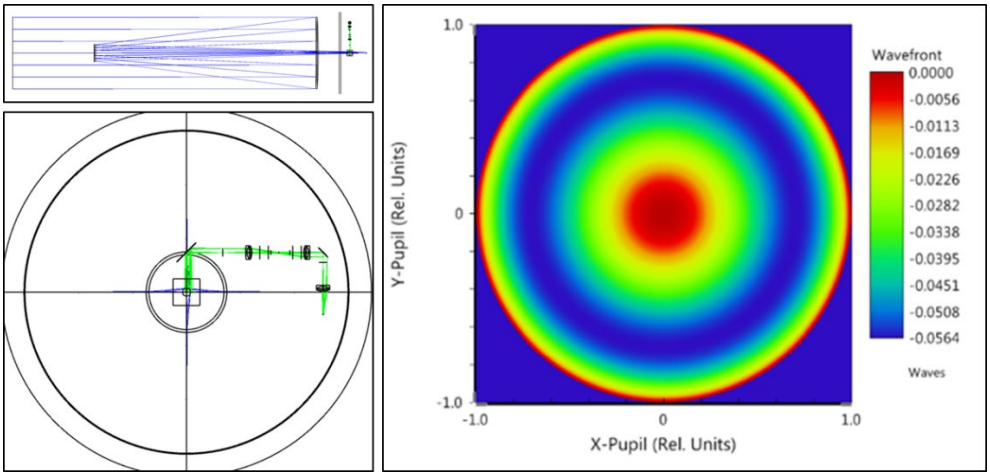


Fig. 13. Optical layout Zemax model of light rays traveling through system to sensor

To fit the optimization parameters identified, the next step was to design the beam launch system. For this a fiber based beam transport system was used to route the light to the side of the inner axis mount of the telescope system. Then collimation optics and a two stage beam expander was used. This ensured that beam expansion was done through optical components and minimized the effect of beam expansion through propagation. This had the effect of minimizing the far field divergence of the collimated beam which is what maintains the effect of creating a point source at multiple propagation ranges covering near the telescope to a point where the photon return becomes too weak to sense. The designed components for the beam launch system were chosen to increase

flexibility of the system, meaning a variable beam expansion system was used. This involves a complex multi-lens system that has to move in two major groups creating a 3 effective lens variable beam expander. The design of the beam expansion is shown in Figure 14 along with the system integration concept in Figure 15. [59]

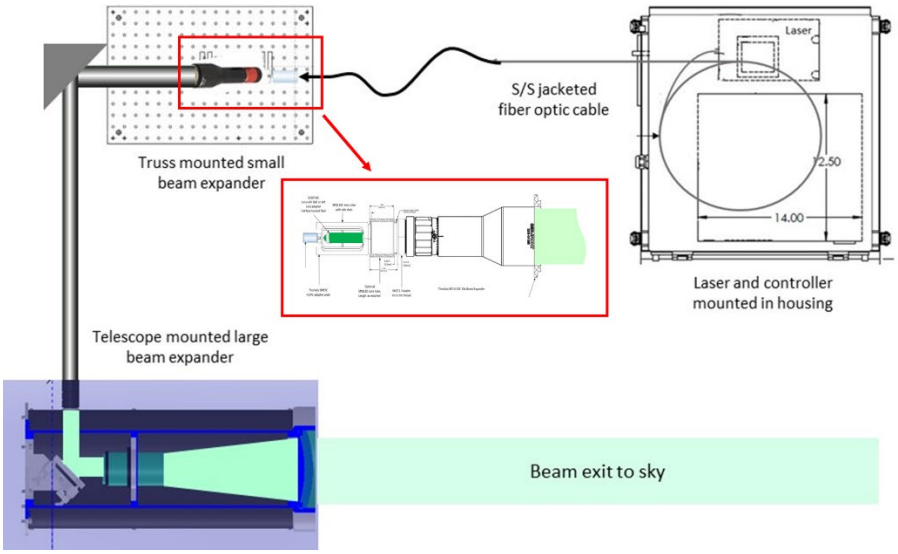


Fig. 14. Design concept for the beam collimation and expansion system

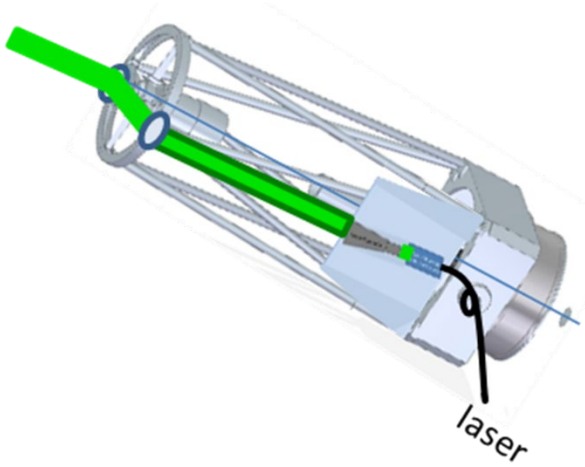


Fig. 15. System integration concept of the beam expansion system

When designing a system that will be required to change range dynamically it was important to design around a focus requirement such that optical components could remain static and still record focused points as seen by the Shack-Hartmann wavefront sensor system. For this the beacon has a minimum range it must be in order to be far enough away that the incoming light can be considered a plane wave. This is necessary as the beacon system creates a synthetic point source, and that point source propagates back towards the telescope system a spherical wave, which is distorted by the atmosphere. The wavefront seen in the pupil plane of the telescope is what is relayed through the system and imaged by the Shack-Hartmann wavefront sensor. The calculation used was the resolution equation for a diffraction limited spot. To account for turbulence the size of the effective aperture was scaled based on the Hufnagel-Valley 5/7 model. The results are shown in Figure 16. This figure shows the resolution limit vs the size of the beam as projected to the designated altitude range. The point of interest is at approximately 550 m. Here is where the projected beacon will be seen as a point source by the system. Below this altitude range it is possible for the beacon to be partially resolvable which could lead to larger spots on the Shack-Hartmann wavefront sensor. Centroiding of the spots will still be possible, but the SNR as seen by a pixel will be affected. Fortunately, at lower ranges the photon return levels are larger and the issue is partially circumvented. In the presence of strong turbulence as compared to a Hufnagel-Valley 5/7 model, the altitude at which the system sees a point source is at a lower altitude which will help the system in focusing the Shack-Hartmann produced spots in the presence of stronger turbulence. An additional mitigation that could be used is one similar to that being developed by the University of Arizona, which is a dynamic refocus system for the sensor. This would also ensure tight focused spots, but was not needed for the design of this system.

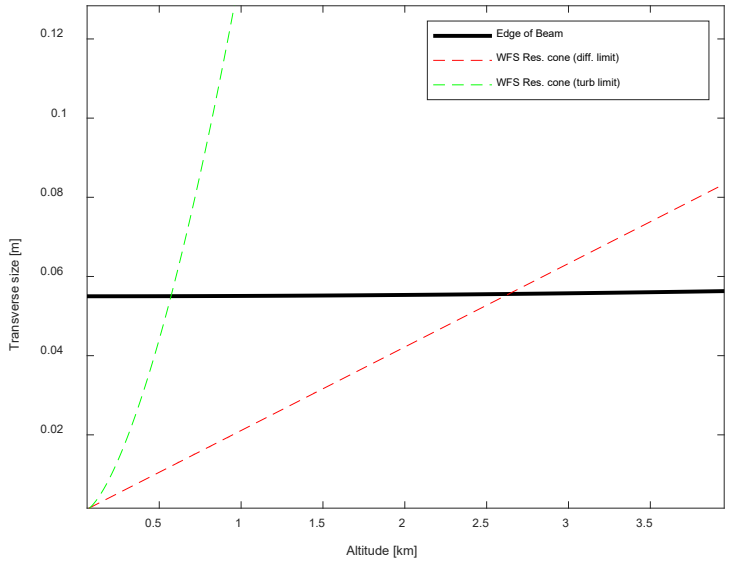


Fig. 16. Plot showing the resolution of the imaging system

## 4.2 System Components and Laboratory Testing

After the design considerations were finalized, components were selected, purchased, and assembled. At this point laboratory based testing of the components was conducted. This was done to verify the component functionality and also update the models with measured values. Additionally the sensing system was built and configured to fit into the required space such that the entire system could be mounted to the telescope. The first item tested was the laser and fiber system. The laser system was tested for pulse energy and beam quality. These are the two critical metrics for the laser system as the pulse energy will directly affect the SNR of the sensing signal and the beam quality of the laser will cause the laser beam to spread more as it is propagated. The laser pulse energy was measured to be 7.92 mJ when operated at full power, and the beam quality ($M^2$) was measured at a value of 1.82. These two measurements are suitable for the design of the system. Figure 17 shows the laser beam setup in the lab and an example of the measured beam profile. During this time the laser was also tested for improved fiber coupling efficiency by

inserting a lens system for focusing the light into the fiber instead of sending in collimated laser light from the laser source. It was proven that the fiber coupling efficiency could not be improved past 94% which was the value measured for the collimated laser input with the chosen fiber. Additionally, by focusing the light with such high pulse energies, when the system was at full power if proper alignment was not achieved the fiber tip would burn up. This was due to the high energy density achieved by a focused laser spot. This was non-optimal as the final system in the field would be subject to small vibrations and burning the fiber tips will cause a recurring maintenance cost. Additionally during lab based testing single mode high energy density damage threshold fibers were considered. Testing of these showed that achieving and maintaining proper alignment was difficult. The benefit of the single mode fiber would have been a smaller starting spot size at the output end of the fiber which could translate into larger beam expansion ratios and a smaller far field divergence angle. This would be desirable, but the system as measured in the lab would be suitable for the fielded demo system.

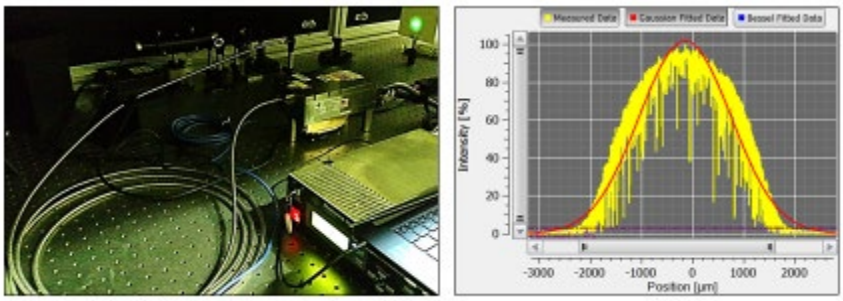


Fig. 17. (left) Image of the laser setup in the lab and (right) the measured beam profile with comparison to a pure Gaussian profile in red

The next item tested was the beam expansion system. This consisted of a two stage expansion and collimation system with the larger of the expanders being a dynamic zoom three effective lens system. This was done so that the system could be configured for any beam size desired. The resultant beam size was subjectively measured by propagating the beam to the ceiling of the high

bay laboratory and looking at the beam size as compared to a known ceiling object size. The beam projected to the ceiling is shown in Figure 18. The leftmost image in Figure 18 shows a spot size of approximately 6 inches. The beam was also propagated across the laboratory, approximately 20 feet, and measured at various distances. The beam size was approximately the same size at all distances showing suitable collimation of the beam.

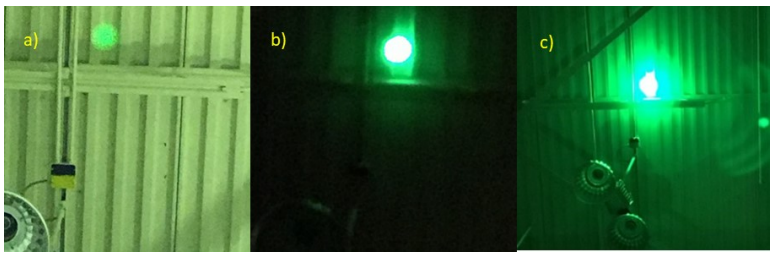


Fig. 18. Beam projection system under test in the laboratory showing the beam spot size on the ceiling of the high bay laboratory

The next component under test in the laboratory was the Shack-Hartmann wavefront sensor. The critical function that needed to be tested was the ability to produce focal spots. This was tested by inputting an optical wave from an expanded laser onto the sensor system and recording the spots. The focal spots from a flat wavefront are shown in Figure 19. Using software it is easy to convert between wavefront measured slopes, deviations from a known center in the focal spots, to construct a segmented wavefront. This wavefront is shown in Figure 20. It is this measured wavefront that will be used as the metric for calculating the profiled strength of the optical turbulence seen by the system.

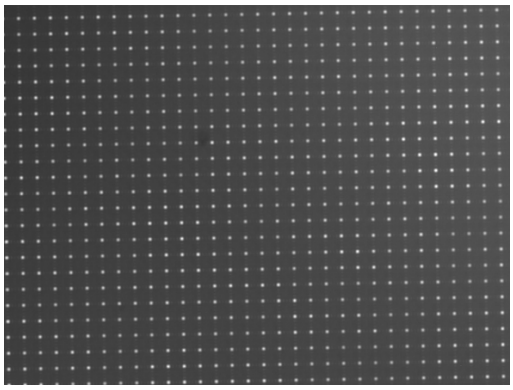

Fig. 19. Focal spots on the camera from a flat input wave as tested in the lab

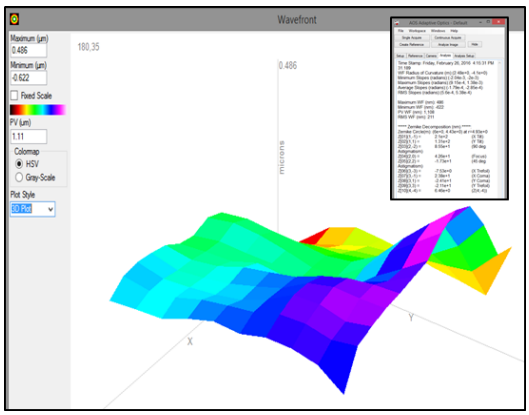


Fig. 20. Wavefront reconstructed from slope measurements on the Shack-Hartmann wavefront sensor

The next item tested was the Pockels cell. The Pockels cell provides the fast optical shutter needed for controlling the range in which the Rayleigh beacon operates. In order to utilize a Pockels cell as a shutter the configuration of two polarizers with the Pockels cell in between was needed, as shown in Figure 21. The Pockels cell rotates the polarization of the optical field when a high voltage is applied to the cell. Then with the configuration depicted an optical shutter between two crossed polarizers can be created. For this to function the Pockels cell has to be aligned precisely to the crossed polarizers and matched to its own rotation axis orientation. The process for setting

this up is to create what is known as an isogyre image when laser light is shown through the crystal. An example of this is shown in Figure 22. To show good blocking of the light Pockels cell voltage was turned on and off and the resultant images were recorded as shown in Figure 23. Using the alignment laser and looking at the center of the isogyre pattern it is shown that the Pockels cell blocks significant amounts of the light and allows for light to pass when turned on.

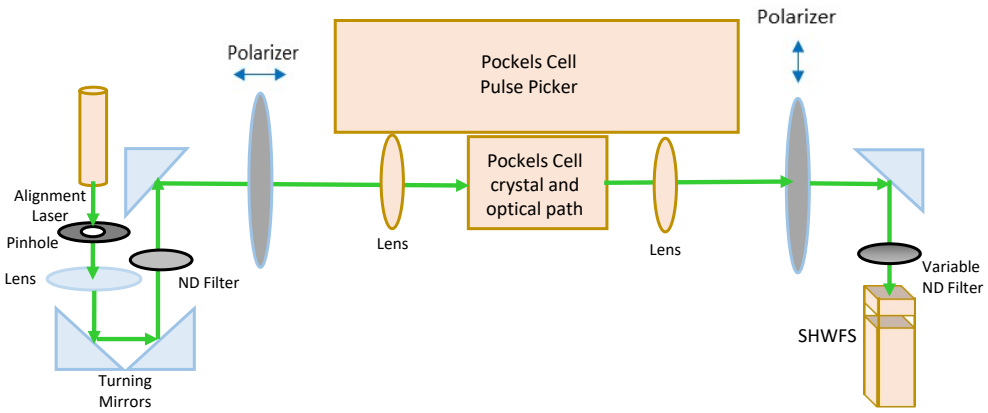


Fig. 21. Optical testing setup for characterizing the Pockels cell as a fast optical shutter

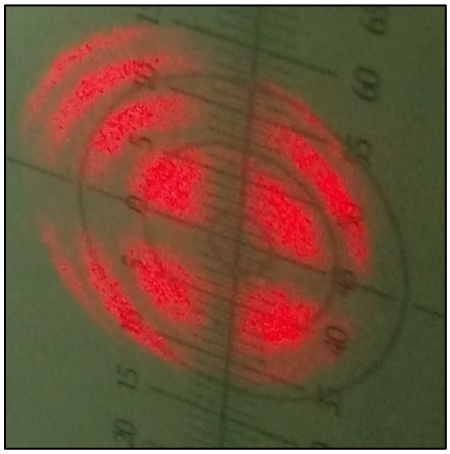

Fig. 22. Example of an isogyre with a significant cross pattern showing proper alignment of the Pockels cell to the polarizers

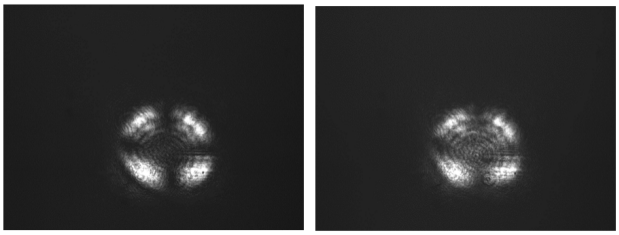

Fig. 23. (left) Pockels cell off and (right) Pockels cell on

The last piece tested in the laboratory was the control system that interconnected all the components. Everything is controlled by a central computer. The central computer has to synchronize all the components and make sure the proper control signals are sent to the appropriate components at the right times in order to control where in the atmosphere the Rayleigh beacon is sensed. That means that the computer talks to and controls the Shack-Hartmann wavefront senor, the delay timer, and the laser controller. In sequence the laser controller controls the laser cavity and firing timing, and the delay timer controls the Pockels cell which is the sensors optical gate. A depiction of the control flow is shown in Figure 24. Control communication was verified in laboratory testing between all components.

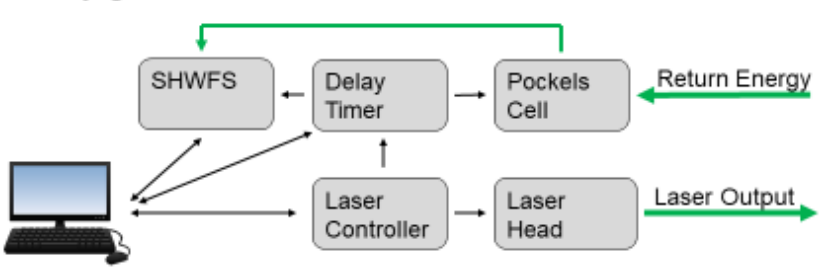


Fig. 24. Depiction of control flow for Rayleigh beacon

### 4.3 System Integration

The next step was to prepare the system in the laboratory for integration onto the proof of concept fielded system. The telescope selected and used is a 61 cm aperture telescope as shown in Figure 25. This telescope has to be prepared to accept all the components which meant its base configuration had to be altered. This resulted in new mounting plates on the back side of the secondary and primary mirrors along with a side mounting bracket. To go with these new changes, a new stress mechanical model for the telescope was developed to show the resulting impact of all the new added weight. This is shown in Figure 26.

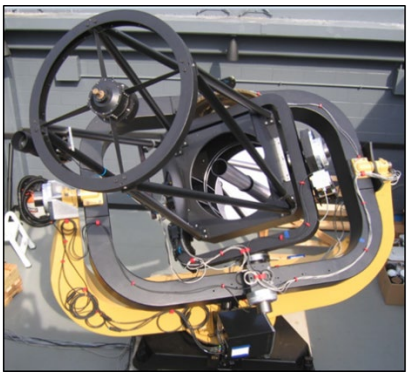

Fig. 25. Telescope system selection for integration of laboratory components

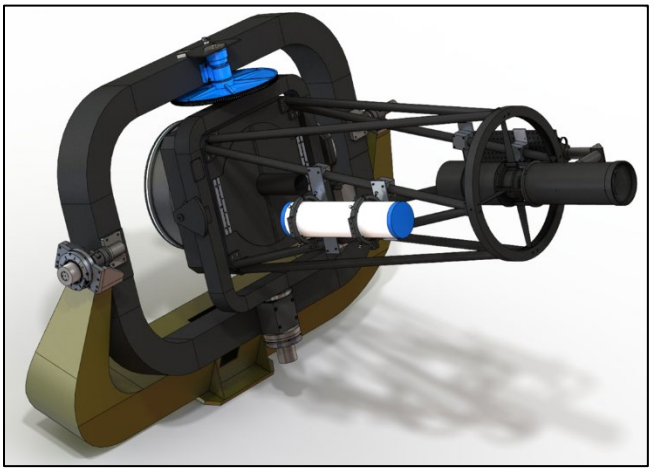

Fig 26. Model for the new components added to the telescope system

The components added to the telescope system were first drafted up in a CAD software package and the physical layout was determined. The final layout is shown in Figure 27. It is shown that all the components easily fit onto a little more than one quadrant of the optical breadboard. There is also a height restriction of 11 inches, so stacking optical components was not possible. This layout is an achievable layout that allows for additional space for the power strips, controllers, and other associated optical components and cords that will be present with the system. The final integrated system is shown in Figure 28.

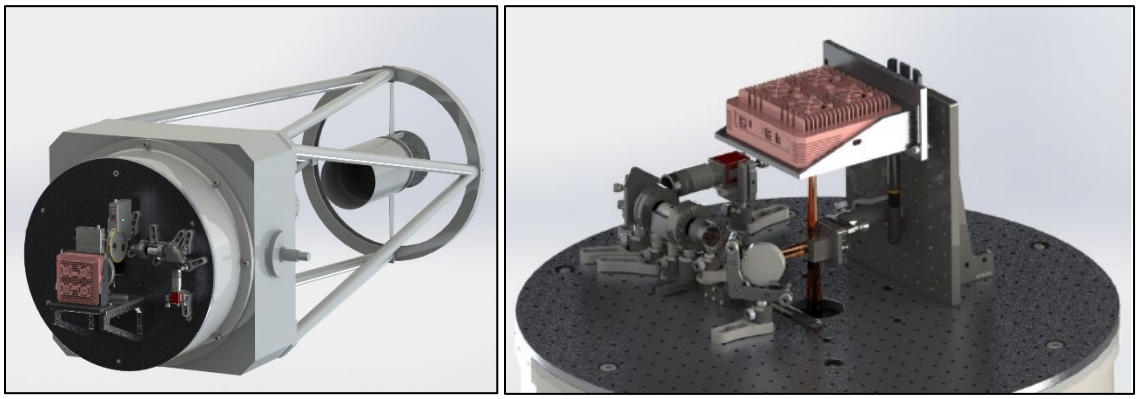

Fig. 27. (left) back view and (right) side view of the CAD mockup of physical components of the Rayleigh beacon sensing system

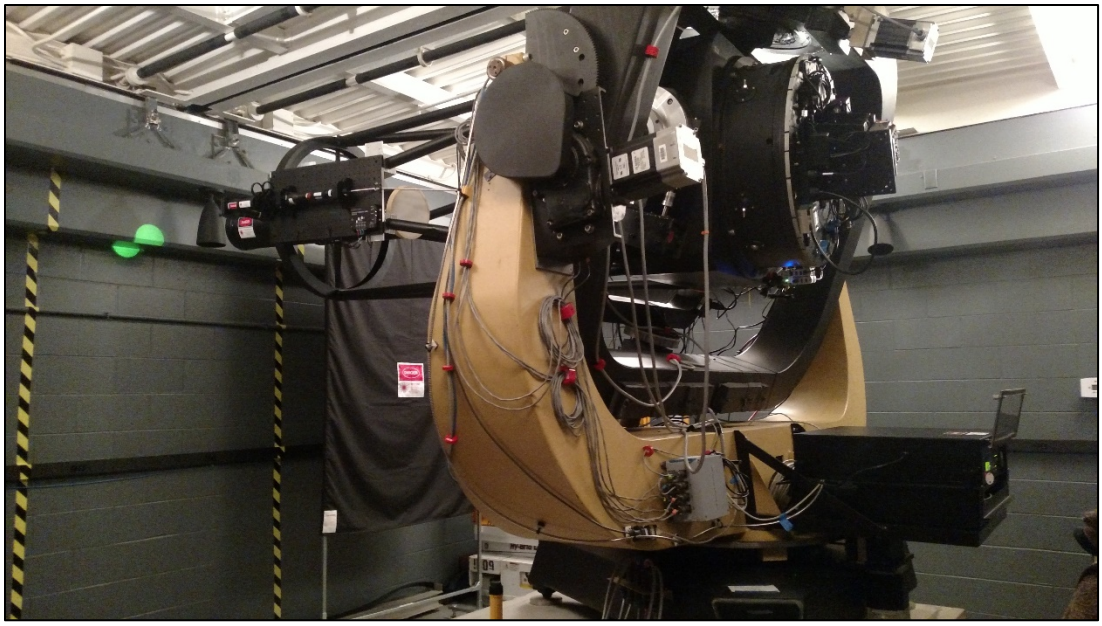

Fig. 28. Final integrated system with all components installed

## 4.4 $C_n^2$ Measurement Methodology

In order to go from a typical Rayleigh beacon system to a system that produces profiled measurements of optical turbulence a new methodology had to be developed. The base idea is fairly simple in concept, but challenging in implementation. The idea is to take normal Rayleigh beacon measurements, which are measures of a distorted wavefront, in rapid succession where each measurement comes from a varied range from the optical sensing system. The base concept with simplified calculation is shown in Figure 29. This concept formulation that was realized into a device was successfully accepted as a provisional patent, serial number 62/592,059. Later at the end of the 12 month lifetime of the provisional patent, a new patent application was submitted that built on the provisional patent for the conceptual design. This patent was filed on 31 January 2020 under the title, “Systems, Methods, and Apparatus for Measuring Atmospheric Turbulence” (AFD 1721) with serial number 16/778,424. From 31 January 2020, novel aspects of the turbulence measurement system, method, and technology are referenced as a “patent pending” invention.

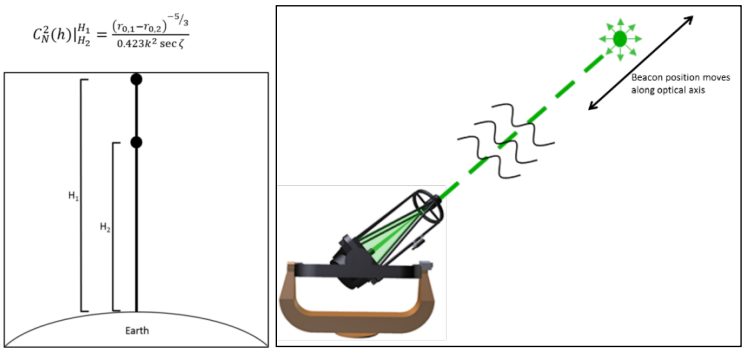


Fig. 29. Depiction of concept for achieving profiled measurements of atmospheric turbulence

The calculation of a profiled metric for the turbulence strength could be deduced in a couple similar, but slightly different ways with this system. The idea is to take path integrated measurements, $r_0$, and convert those into an atmospheric region specific $C_n^2$ value through differentiation. There is however a choice in how to apply this algorithm idea. The value of $r_0$ could be deduced from individual sub-apertures of the Shack-Hartmann wavefront sensor array, each of which account for neighboring parts of the atmosphere. An average effect of $r_0$ could be used as captured by the whole array of sub-apertures possibly fit to a smoothing wavefront measurement schema such as those described by Zernike polynomials. Lastly, a concept that takes earlier more base forms of the measured data, such as a deviated slope difference, could be used to capture the profiled effect of atmospheric turbulence. The plan was to build the system to collect data and then process the data with all three of these methodologies in mind. The ways that the data was saved allowed for any of these implementations to be used simultaneously in post processing.

The measurements produced by the dynamically ranged Rayleigh beacon system were compared to known models for profiled atmospheric turbulence. As an example, two models are shown in Figure 30. Figure 30, shows a standard Hufnagel-Valley 5/7 model along with the Tatarski model

that is inputted with typical atmospheric parameters. It is noted that there is a large disagreement between the models that spans multiple orders of magnitude, which is larger than the Gaussian random variable used around the average in the HV 5/7 model, as described in the theory section.

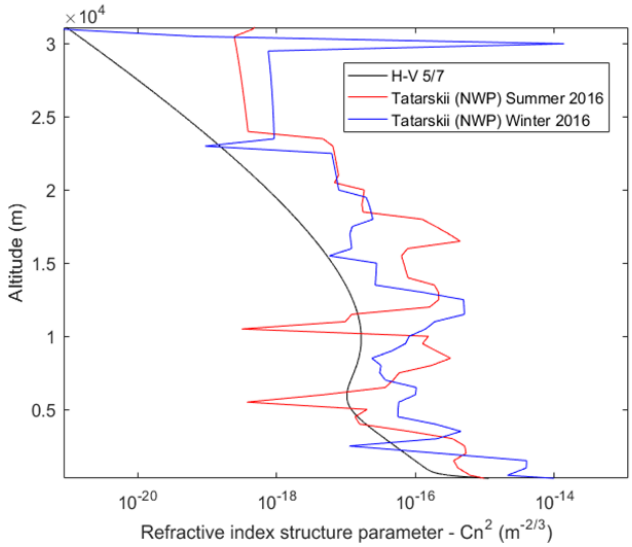


Fig. 30. Example models used for deducing the profiled strength of atmospheric turbulence

### 4.5 Physics Based Model

Alongside the design models, utilizing the designed components a physics based model was developed to simulate the full system and evaluate the effectiveness of the design concept. The physics based model is based off of wave optics propagation codes combined with system component modules. The flow of the model is as follows: 1) generation of the atmospheric turbulence environment which is based off of Kolmogorov phase screen generations, 2) propagation of the outgoing laser beam, 3) scattering of that beam to create the reference source for the sensing system, 4) propagation back through the same atmosphere, 5) mapping of the pupil plane of the telescope onto the propagated phase screen, 5) generation of a Shack-Hartmann wavefront sensor model, 6) modal gradient sensing of the wavefront seen in the pupil plane of the

telescope by the Shack-Hartmann wavefront sensor, and 7) analysis of the sensed atmospheric induced phase perturbations. This model has been incrementally developed using the coding basis provided in the book *Introduction to Fourier Optics* by Jason Schmidt. [20] Additionally, these codes have been developed in a modular fashion such that the collected on-sky data can be inserted into the analysis train by adding in a data formatting ingestion script so that modeled data can be directly compared to on-sky collected data.

Initial simulations were done to show the feasibility of the design concept and sensing methodology. The setup for this utilized 201 phase screens that were generated from a random realization of the atmospheric turbulence which was created from Kolmogorov theory utilizing a HV 5/7 profile for the turbulence strength. The beam inputs and sensor configuration matched the system described previously. The geometry considered for the initial simulated data generation entailed beacons ranging from 600 m to 14 km at 2000 m increments just to show the proof of concept. A series of propagations was used from each respective range using the integrated turbulence strength to generate a turbulence induced phase screen at the telescope pupil plane. An example of a sensed wavefront as seen by the Shack-Hartmann wavefront sensor with associated measured modal gradients is shown is Figures 31 to 33. The measured gradients were converted into values of $r_0$ as seen by the whole sub-aperture array. These value of $r_0$ were used and differenced from each other, and then converted into $C_n^2$ values. These were plotted against theory as shown in Figure 34. The small differences are likely due to the fact that the measured values were computed for a single realization of the turbulence using phase screens generated from HV 5/7 models for turbulence strength. If an ensemble of realizations were to be competed the two lines in Figure 34 would likely converge. None the less, this simulation shows potential in this technique to obtain an accurate measurement of the profiled turbulence strength.

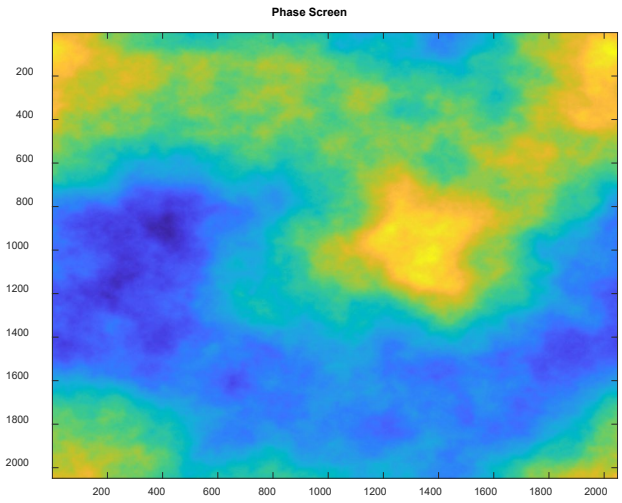


Fig. 31. Example of turbulence phase screen applied in simulation

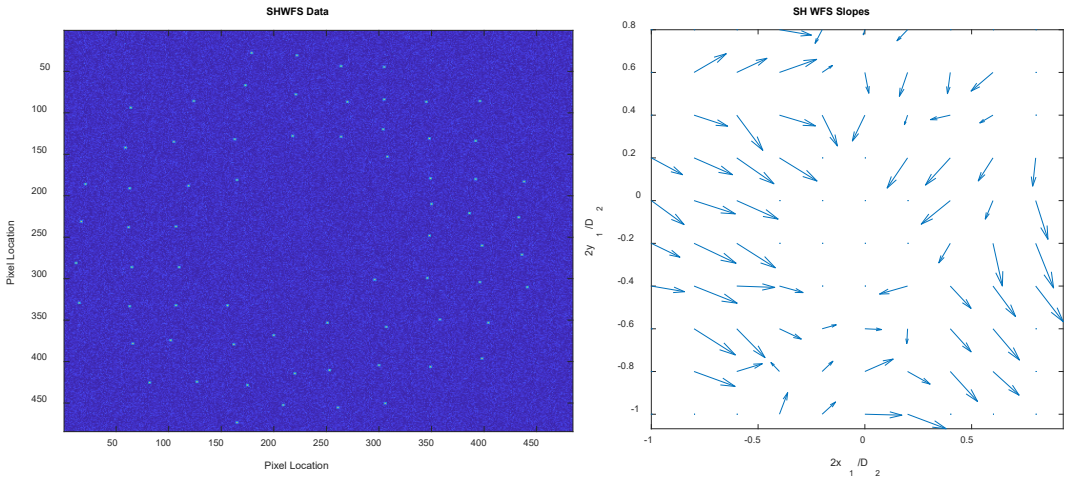


Fig. 32. Example of a (left) SHWFS image and (right) computed gradients

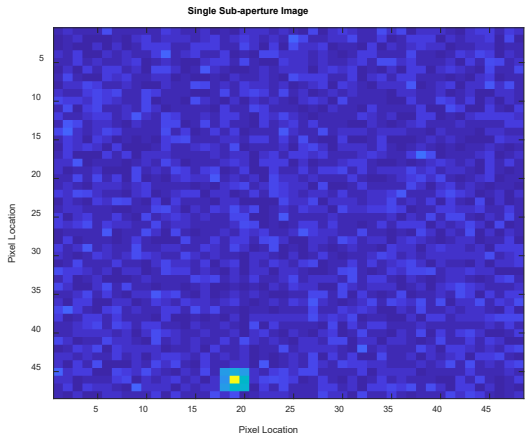


Fig. 33. Single sub-aperture image from the SHWFS showing the spot displacement due to sensed wavefront tilt induced by the simulated atmosphere

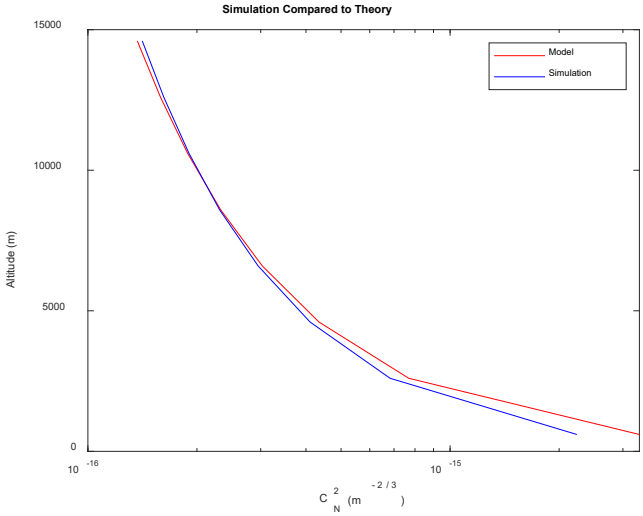


Fig. 34. Simulation compared to theory for measuring the strength of turbulence for a dynamic range gated beacon

## 4.6 Early Challenges and Implemented Solutions

During the system integration and testing phase of this research a few engineering challenges had arose. Those involved a malfunctioning laser, system timing, and SNR improvements. The first

challenge described will be the malfunction laser diagnostics. Under nominal operation condition the outgoing laser pulse into the atmosphere can be seen by an observer as shown in Figure 35. The beam is bright and easily seen. This is a requirement for the FAA and laser safety procedures for aircraft avoidance. During operation there was a noticeable loss in brightness. The laser system was taken back to the laboratory for diagnostics as a result of this. Under diagnostics it was noticed that the beam appeared to no longer be Gaussian in shape as shown in Figure 36. The laser was consequently sent back to the manufacturer for repair. It was determined that the laser crystal had cracked and needed to be replaced. The laser was returned in nominal operating condition from the manufacturer with a Gaussian outgoing beam.

Fig. 35. Image of laser operation when under first light testing (Photo Credit: Dan LeMaster)


Fig. 36. Laser beam shape (left) post-repair and (right) pre-repair after noticeable loss in outgoing power

As a result of the laser repair, the outgoing beam from the laser prior to being coupled into the fiber was slightly larger in size and no longer centered on the outgoing port of the laser box. This resulted in a 15% loss in fiber coupling efficacy. 15% is a significant loss in outgoing power and has a large impact on the overall photon budget. So a solution was implemented to have control over the fiber coupler position, and an addition of an inserted lens to improve the coupling efficiency. The lens reduces the beam size by 20% to 40% with adjustable precision and will allow for more light to make it to the end of the fiber. The new fiber coupler is shown in Figure 37.

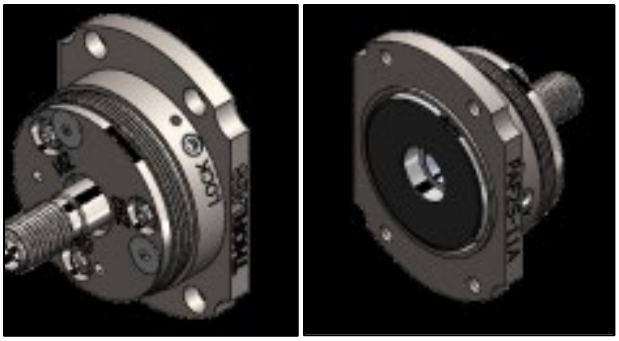

Fig. 37. New fiber coupler model used for increasing fiber coupler efficiency

The next challenge that was identified was the need for precise mapping of the system timing. It was discovered that some of the components as delivered had larger control delays than specified by their manufacturer. Consequently, precise mapping of the timing of all control signals was needed. This analysis was performed with an oscilloscope and some of the results are shown in Figure 38. With known system timing information the slice of the atmosphere sensed by the system is known to a higher precision and as a result the system will function with less uncertainty in the measurements. Additionally, this verifies that the integrated components communicate with each other in a quick enough response such that dynamic range gating will be possible.

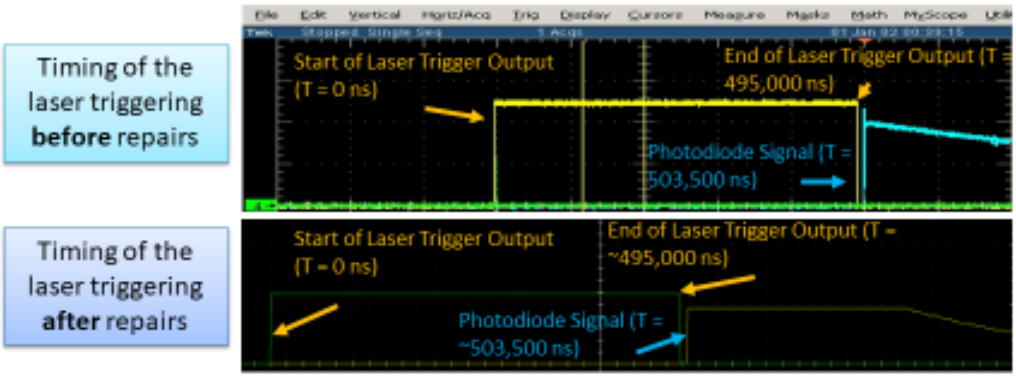


Fig. 38. Oscilloscope measurements of control timing for laser and sensing system

The last challenge that arose has to do with methodologies for improving the overall SNR of the system. This is important as signal levels as seen by the camera were discovered to be low as compared to initial theory. Information from testing was incorporated into the theory models and resulted in a more realistic assessment of the SNR environment and causes for decreasing in the overall signal. This lead to improvements. Improvements were categorized into two categories, signal strength improvement and noise suppression. Signal strength was improved by swapping components for higher throughput components. The major factor here was in the system polarizers which had a 74% throughput at the designed wavelength. With a newly selected part the throughput rose to greater than 90%. Cleaning the primary and secondary mirrors of the telescope helped as well. These were unmeasured, but estimated to be around 65% efficient due to be degraded. Cleaning has an estimated improvement to result in approximately 80% or greater reflectivity. Another option that was not implemented could be to recoat the mirrors which would improve the reflectivity to greater than 96%. However, the system would be non-functional for approximately six months, so this option was not implemented. Changing the polarizers had the additional benefit of selecting parts with higher extinction ratios which will lead to a better light blocking capability.

The signal strength of the sensing system was also improved by a redesign of the Shack-Hartmann sensor. A different lenslet array was chosen such that the total grid size was reduced to a 10 by 10 from a 20 by 20. This will effectively improve the SNR by a factor of four. With this design choice careful consideration had to be taken for the system to produce an accurate wavefront atmospheric tilt has to be the dominate wavefront aberration factor on each lenslet. For a 10 by 10 grid the effective diameter of a sub-aperture in the pupil plane is approximately 6 cm. Expected measurement values of $r_0$ are to be in the range of 5 cm or greater for most conditions with a nominal day $r_0$ for a full atmospheric path to be around 7cm. This will be sufficient for the main atmospheric turbulence produced aberration effect to be tilt, and thus the slope measurement

produced will accurately represent the wavefront produced by the collection geometry. Additionally, with the new lenslet array the focal points were chosen to map into a tighter spot. This improved the energy contribution in the central pixel while still having measurable energy in the wings to be used for centroiding. The schema chosen uses a 3 by 3 spot for centroiding which produces a very accurate sub-pixel slope measurement. Results from the new lenslet design are shown in Figures 39 to 41.

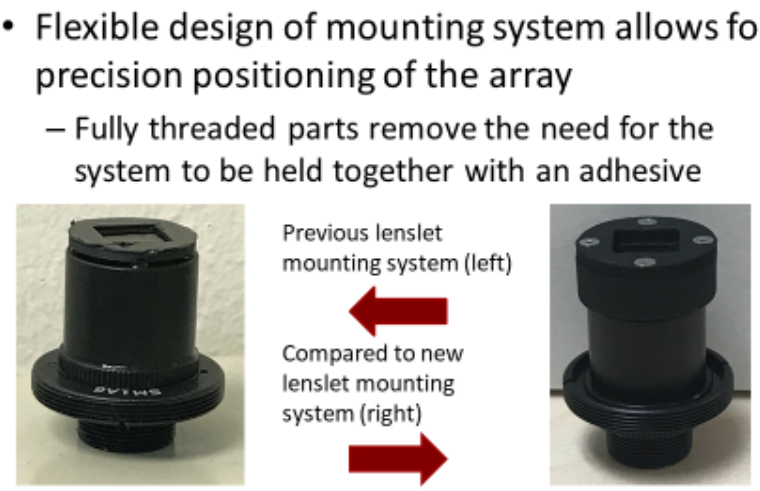


Fig. 39. New lenslet holder for more precision in mounting the lenslet in front of the camera

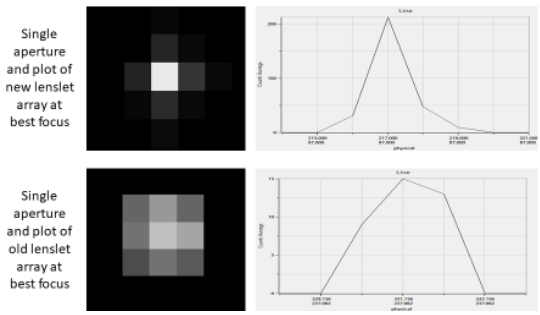


| Grid Size | % of signal (New Lenslet) | % of signal (Old Lenslet) |
|---|---|---|
| 1 x 1 | 46% | 14% |
| 2 x 2 | 69% | 35% |
| 3 x 3 | 89% | 80% |
| 4 x 4 | 95% | 87% |
| 5 x 5 | 100% | 100% |

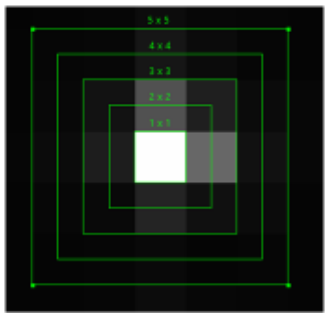


Fig. 40. New lenslet array focal spot improvement showing higher concentration of energy in central pixel

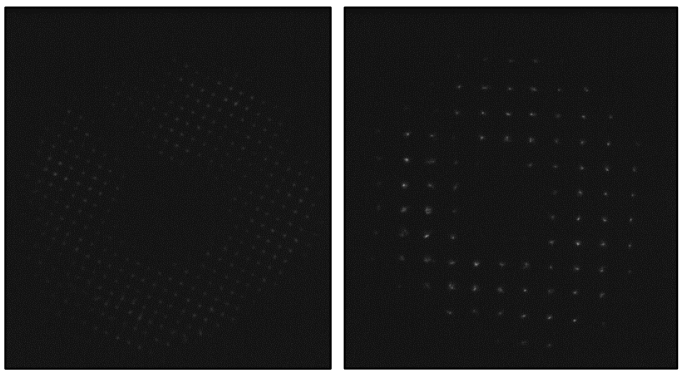

Fig. 41. Measured Shack-Hartmann wavefront sensor spots for Polaris from (left) old lenslet array and (right) new lenslet array

The final SNR improvement was a new camera choice which had better performance ultimately reducing the noise levels and improving the sensitivity. The new camera is the Mako-G40 which was a new and improved model for our current camera. This camera was a direct swap for the old

one as the housing and focal plane location was identical. This was a convenient and quick way to achieve an SNR improvement. The quantum efficiency of the G40 camera was an improvement from 55% to 65%. Also there was a dark current improvement from 13.4 electrons to 4.1 electrons which provides a boost to the overall SNR. Overall, using the new camera there was a noise decrease of approximately 140%. Utilizing all the SNR improvements the detectability of the returning laser light was greatly improved and ultimately allowed for first light measurement to be more easily achieved and in the long run allowed for farther range gated signals to be sensed.

## 4.7 Conclusions

The methodology section explains how the novel concept formulated for measuring the strength of turbulence along the propagation path was transformed into a realized system. Early design considerations informed the component choices and guided the part selection. The components were tested in the lab for functionality and lead to an integrated system. The integrated system was under initial testing while at John Bryan State Park Observatory for the early duration of the research effort and continues to remain at the observatory for testing and data collection after this dissertation research effort has concluded. In parallel a physics based model had been developed which was used as a tool for testing the system and adding levels of fidelity to testing the system design concepts. This model led to a full wave optics simulation with a high fidelity sensor model that captured the measurement schema. This resulted in simulated measurements that matched well with theory. Lastly, some early challenges were identified and the solutions implemented were discussed. This process is what has taken place and laid the foundation for the sensor design and processing algorithm for determining the strength of atmospheric turbulence along the propagation path.

# V. Data Processing Methodology

## 5.0 Introduction

The data processing methodology section explains how the novel concept formulated for measuring the strength of turbulence along the propagation path was implemented as a post-processing technique to produce estimates of the turbulence strength profile. This section was based on a SPIE Applied Optics Journal article [52] that was peer reviewed and published. To test the processing methodology, a wave optics simulation with a high fidelity sensor model that captures the measurement schema was developed. This resulted in simulated measurements that matched well with theory. This process is what took place and laid the foundation for the sensor design and processing algorithm for determining the strength of atmospheric turbulence along the propagation path.

Long-range optical imaging applications are typically hindered by atmospheric turbulence. The pseudorandom variations in the index of refraction are the physical observables resulting from atmospheric turbulence. This effect leads to unwanted optical blurring of the image. As a result, there is a need to understand how these pseudorandom variations in the index of refraction behave and evolve along the viewing path. Furthermore, knowledge of the profile strength of the index of refraction structure parameter can lead to mitigation strategies for combating the undesired effects. A previously presented conceptual strategy [54] has been developed for measuring the strength of the refractive index structure parameter profile utilizing a dynamically ranged Rayleigh beacon system. A dynamically ranged Rayleigh beacon system is a modification of a traditional Rayleigh beacon system design to allow for the originating location of the backscattered field to change in the range from the collecting aperture of the telescope. When this dynamically ranged methodology is employed, a new set of data processing algorithms can be used to extract information about

localized turbulence strength contributions as opposed to just a single volumetric estimation of turbulence strength, which is the output from traditional laser beacon systems. This paper presents an approach for extracting localized turbulence strength information based on the methodology employed by a dynamically ranged Rayleigh beacon; the associated data exploitation algorithm that has been developed and investigated can accurately produce tomographic refractive index structure parameter strength profiles. Two example cases are used in this section to highlight this capability.

Other similar methods for sensing the tomographic strength of turbulence over a path or overcoming turbulence effects in a discretized step manner using beacon-based measurements have previously been proposed, and those have provided an inspirational basis for the methods presented in this paper. One such method involves three-dimensional (3-D) tomographic projection where wavefront sensor measurements are used to directly measure the phase in a two-dimensional (2-D) plane orthogonal to the direction of propagation. Then measurements taken at various angles through the turbulent flow were used to reconstruct the 3-D structure of the index of refraction. [33] A second method is a byproduct of a proposed multiconjugate adaptive optics (MCAO) system in which multiple Rayleigh beacons are used to measure needed phase corrections over a wide field of regard. By intentionally choosing beacons at varied ranges, turbulent layer range misregistration in the MCAO system can be sensed and avoided. It was also proposed that intentionally varied ranges from multiple beacons could be used to find strong contributing turbulent layers, and thus reduce the effect of focal anisoplanatism and improve stability of the point spread function across larger field angles. [35] Additionally, wave-front sensor data from Rayleigh beacons have been used to produce propagated laser beams with improved performance using phase estimates to correct scintillation effects. This type of measurement and response has been proposed to increase the effective range of a laser weapon system through sequential compensation iterations within a

slowly changing or nearly static atmosphere. This proposes a laser beam projection system with a near-field phase retrieval method for delivering more power to a target at an extended range. [62] These works have provided inspirational aspects influencing the design concept of a dynamically ranged Rayleigh beacon system; however, each individual method presents differences that influence that way the collected data is analyzed to produce estimates of the strength of the refractive index structure parameter, associated turbulence-related metrics, or near-real-time phase correction. The concept of a dynamically ranged Rayleigh beacon system is unique compared to these because of its ability to control the backscattered field originating range on a pulse-by-pulse basis employed by a single on-axis beacon. This system design introduces a new set of possibilities for extracting localized turbulence strength information and consequently presents an opportunity for innovative algorithm development. Specific to this paper, the data exploitation algorithm that was developed is a new means for extraction of tomographic estimations of the refractive index structure parameter specifically tied to the dynamically ranged Rayleigh beacon-based data collection system.

There are multiple technologies for producing tomographic estimations of the strength of turbulence. These technologies did not provide inspiration for the system or processing techniques in this paper, but are the alternative technologies that aim at the same goal of estimating the profiled strength of turbulence along a viewing path. These alternative technologies utilize techniques involving slope detection and ranging (SLODAR), sound detection and ranging (SODAR), scintillation detection and ranging (SCIDAR), differential image motion LIDAR (DIM LIDAR), and multi-aperture scintillation system (MASS). Each technique has distinctive advantages and disadvantages as compared to the dynamically ranged Rayleigh beacon technique. SLODAR is an optical triangulation technique utilizing two or more beacon sources. Systems using laser beacon sources are still quite new, but more established techniques utilizing paired natural stars have been

implemented at select observatories for a number of years. The geometric regional overlap in the propagated waves from the two separated sources allows for estimation of $C_n^2$ relatively near the aperture in resolution bins defined by the spatial location of sub-apertures in the pupil plane relative to the geometric separation of the beacon sources. SLODAR processing is dependent on the statistical correlation between wavefront sensor slopes. [1, 11, 4] A dynamically ranged beacon system is similar in sensor design to a SLODAR system; however, the way in which the data are processed to produce a turbulence profile estimate is vastly different. A SLODAR system analyzes slope correlations from angularly separated beacons, whereas a dynamically ranged beacon system utilizes spatial variances and differentiation between sequential beacons from separated ranges along the optical axis of the sensing system. Next, a SODAR system utilizes sound waves in a similar way to radar and measures the structure constant of temperature $C_T^2$.The structure constant of temperature is then related to the structure constant of the index of refraction. [2] This is an inferred method for producing a profile estimation of atmospheric turbulence and does not directly measure any perturbed wavefront. SCIDAR is another optical triangulation technique similar to SLODAR, except the measurement taken is a scintillated intensity pattern, which is a second-order effect as it is dependent on the second derivative of the optical wavefront. From the intensity pattern, a scintillation index can be calculated through correlation of the multiple intensity patterns, and a resultant profile of turbulence strength can be estimated. [25, 27] An adaptation of a SCIDAR system is the MASS. The MASS was designed to overcome the deficiencies of a SCIDAR system, which include the requirement for a bright double star and a large aperture telescope. The MASS utilizes a single star and multiple apertures as spatial filters to sense the photon counts associated with scintillation. The mapping of the photon statistics in each aperture can be traced to turbulence effects originating from specific ranges. [7, 6] Finally, a DIM LIDAR is the incorporation of a DIM monitor and a LIDAR system. The DIM part utilizes a technique that measures the variance of the differential wavefront tilt by two or more spatially separated apertures. The variance statistics are

gathered over a relatively long timeframe to produce an averaged value of the turbulence strength between the collecting apertures and guide star. The LIDAR part comes from changing the range of the beacon. This allows for the discretization of the averaged turbulence strength estimates to build up a profile estimate. [16]

These alternative methods described have underlying processing techniques and inherent phenomenology characteristics that are distinctively different from those described by the methods proposed for a dynamically ranged beacon. Multiple methods rely on statistical spatial correlations to build up an estimate of turbulence strength. A dynamically ranged beacon system could exploit similar correlations under sub-aperture crossed-path geometries between two different range beacons; however, the methodology is not reliant on that to produce a turbulence strength profile estimate. Instead, a metric of wavefront variance across an aperture is used for volumetric estimates of turbulence strength and then a differentiation algorithm is employed based on the dynamically ranged beacon location to produce localized turbulence strength estimates. The dynamically ranged beacon system utilizes a series of direct measurements of the wavefront present in the system's pupil as the input to producing a profile estimate of the turbulence strength. This is inherently different from methods where associated measurements are made, such as $C_T^2$, and inferred relations are used to get back to an index of refraction structure parameter estimate. It is also inherently different from the case of building up variance statistics from a few apertures measuring modal tilts and applying DIM algorithms to assess turbulence strength. The fact that a wavefront is captured at a finer resolution so that the zonal tilts are the dominating aberrations in each section means a wavefront spatial variance statistic can be used to produce a near-instantaneous estimate of the integrated turbulence strength. This coupled with a rapidly changed beacon location can build up a turbulence strength profile.

The exploitation of measurements produced by a dynamically ranged Rayleigh beacon is based on the formulation of the Fried parameter. The estimation of the Fried parameter from each wavefront produced provides a metric for assessing the strength of the turbulence along the integrated viewing path. On an individual laser pulse basis and corresponding single measurement, this is nominal treatment for data of this type. [58] However, tuning the range gate timing for a turbulence profiling purpose or investigation of a concentrated layer's structure can be done to achieve further characterization than that of an integrated volume measurement. Moreover, under the assumption that the atmosphere is frozen between a measurement and the immediate next measurements in sequence within the specified fraction of a second time period, a discretized range resolved estimation of the strength of the optical turbulence can be produced. The data processing algorithm for constructing a turbulence strength profile, the basis for the algorithm's formulation, and the results from modeled scenarios are presented in this paper.

## 5.1 Key Concepts to Support Algorithm Development and Evaluation

### *5.1.1 Optical Turbulence Metrics*

Introduced by Fried (1966), the Fried parameter, $r_0$, defines the diameter of a circular pupil that would produce an equivalent diffraction limited full width at half maximum of a point source image as the atmospheric turbulence would with an infinite in extent mirror. This metric is correlated with the strength of the atmospheric refractive index fluctuations. The root mean square (rms) phase variation over a circular aperture of diameter $r_0$ is $\langle\sigma\rangle^2 = 1.03\, rad^2$. Spatial wavefront patches of size $r_0$ can be regarded as planar phase regions within the circular pupil. The pupil used for measurements should be divided into many sub-apertures that are smaller than $r_0$ in extent resulting in many individual planar regions that can be accurately measured by a conventional Shack-Hartmann wavefront sensor (SHWFS). The individual spot measurements of a Shack-

Hartmann wavefront sensor can then be used to reconstruct the non-planar phase of the pupil commonly known as the wavefront. This non-planar phase is used for estimation of the atmospheric $r_0$ for the sensed volume under the Rayleigh beacon. For a spherical wave, $r_0$ can be expressed in terms of a weighted integral

$$r_0 = \left[0.423k^2 \int_0^L C_n^2(z) \left(\frac{z}{L}\right)^{5/3} dz\right]^{-3/5} \tag{68}$$

where $k=2\pi/\lambda$ is the wavenumber, $\lambda$ is the wavelength, $L$ is the distance to the source, $C_n^2$ is the refractive index structure parameter. $C_n^2$ is a metric used to quantify the strength of turbulence at specified distances, $z$, along the viewing path. The units are in $m^{-2/3}$ and are typically in the range of $1 \times 10^{-13}$ to $1 \times 10^{-17}$ in the lower atmosphere, but turbulence can be stronger or weaker depending on the location and viewing scenario. For this treatment we will assume that $C_n^2$ power spectrum follows the Kolmogorov model form. [49]

The Earth's atmosphere refractive index structure evolves over time and space in a random fashion under the Kolmogorov statistical model. This causes light to be distorted as it propagates through the atmosphere. In most theories of atmospheric turbulence, turbulent flow kinetic energy is transferred from large eddies to small eddies in a cascading fashion until the energy is dissipated. The average size of the large eddies is the outer scale, $L_0$, and the average size of the smallest eddies is the inner scale, $l_0$. The range of eddy sizes between the inner and outer scales is called the inertial subrange. The Kolmogorov model only pertains to the inertial subrange, and ignores inner and outer scale effects. Electromagnetic propagation takes place within Earth's atmosphere at the speed of light. Therefore, within relatively short periods of time the refractive index changes present within regions of the atmosphere can be considered stationary in time and fixed in position. This is because the speed of light is comparatively fast, and light can travel much farther than even the

span of the largest of turbulent eddy cells. Consequently, the temporal properties of atmospheric turbulence can be regarded as static for these same short periods of time. [10]

In atmospheric propagation scenarios that are modeled using wave optics techniques, turbulence can be treated as a finite number of discrete layers. Each layer is represented by a phase screen that is a flattened projection representation of phase variations in a much larger volume. Each phase screen is a singular realization of the atmospheric turbulence experienced by the propagating wave for a designated volume. This effect can be summarized by dividing the total volume into discrete segments. According to Andrews and Phillips [32], the discrete sum version of the Fried parameter for a spherical wave is

$$r_{0,SW} = \left[0.423k^2 \sum_{i=1}^{n} C_{n_i}^2 \left(\frac{z_i}{\Delta z}\right)^{5/3} \Delta z_i\right]^{-3/5} \tag{69}$$

where $\Delta z_i$ is the thickness of the turbulence volume and $z_i$ is the location along the propagation path. A segmented form of an effective coherence diameter is

$$r_{0_i} = \left[0.423k^2 C_{n_i}^2 \Delta z_i\right]^{-3/5}. \tag{70}$$

This expression for the effective coherence diameter is the plane wave based solution which differs from the spherical wave solution. This removes the effect of weighting the metric towards the receiver. [32] Since the employment of the described algorithms is based on differentiation of subsequent measurements, the effects near the receiver are canceled out and the simpler form of a plane wave can be used. However, the physical nature of the wave propagation from a beacon is that of a spherical wave, so it is important to utilize spherical wave based equations for total integrated volumes. This can consequently be substituted into the discrete sum version of the Fried parameter for a spherical wave to yield

$$r_{0,SW} = \left[\sum_{i=1}^{n} {r_{0_i}}^{-5/3} \left(\frac{z_i}{\Delta z}\right)^{5/3}\right]^{-3/5}. \tag{71}$$

Since it is shown that the total path Fried parameter can be thought of as a sum of discrete segment measurements or estimates, it is consequently justifiable to utilize subsequent measurements of the Fried parameter where the atmosphere is considered stationary to derive the Fried parameter segment strength. This is represented mathematically as $r_{0_i} = r_{0_{j+1}} - r_{0_j}$ where $j+1$ and $j$ represent two measurements of $r_0$ from different beacon ranges. Under these conditions the Fried parameter segment strength can be used to calculate the refractive index structure parameter in discretized layers. This metric is calculated as

$$C_{n_{seg}}^2 = \frac{\Delta r_0^{-5/3}}{.423k^2\Delta z} \tag{72}$$

where $r_{0_i}$ is the Fried parameter segment for two subsequent path measurements. The refractive index structure parameter segments can then be recombined to build up the total profile based on the choices of ranges used as part of the concept of operations (CONOPS) employed by the dynamically ranged Rayleigh beacon system. This treatment lays the foundation for the simulation and evaluation of the profiled nature of atmospheric turbulence strength as measured by a dynamically ranged Rayleigh beacon system that operates utilizing *n* phase measurements configured such that structure effects are measurable.

### *5.1.2 Simulated Wave Propagation*

Simulations were carried out in a multi-step propagation method described by Schmidt [20] utilizing the metrics presented previously. For a dynamically ranged Rayleigh beacon system scenario, a point source is projected at distance *L*, and a multi-step propagation is performed where a sequence of *n* phase screens are utilized. The *n* phase screens used for simulation are chosen in number to at minimum match the resolution desired by the methodology described in Equation 72. The number of phase screens chosen in a simulation to match practice would be limited by the repetition rate of the laser system used and the assumed time in which the atmosphere can be

considered statistically frozen. Standard Fourier optic wave propagation methods were used to simulate the beacon projection and returned light field. This method accurately captured the modeled effects of the layered atmosphere and how a Shack-Hartmann sensor system captured the phase information present in the telescope's pupil plane from the returned optical energy originating from varied ranges. The data from multiple measurements were aggregated within an assumed time window constraint and were used to feed to the methodology associated with Equation 72 to form a profile estimate. Many Shack-Hartmann based measurements were collected to build up an ensemble of realizations for randomly different atmospheres all having the same turbulence strength injections. This collection of data was used to build up statistically significant metrics for utilizing atmosphere propagated wavefronts originating at strategically varied Rayleigh beacon ranges. This was done to ensure a specific Shack-Hartmann wavefront sensor based phase measurement of a single turbulence scenario was not an anomaly and was representative of how the methodology presented could perform. [51] Within the framework of a Fourier optic simulation of the wave propagation of a dynamically ranged Rayleigh beacon, accumulated measurements from individualized propagations can be used to provide measurement-based tomographic turbulence strength estimations

### *5.1.3 Shack-Hartmann Wavefront Sensor Measurements*

A Shack-Hartmann wavefront sensor is utilized to measure the incident phase on the collecting aperture of the sensing system. The SHWFS consists of a lenslet array mapped to the pupil plane of the collecting aperture and a camera that is placed at the focal plane of the lenslets. The lenslet focal length and spacing determines the systems sensitivity and dynamic range for sensing wavefront tilt. The number of lenslets in the array determine the resolution of the wavefront measuring system as projected to the pupil plane of the collecting aperture. Under the simulation scenario utilizing Kolmogorov turbulence statistics, the incoming wave has zonal phase tilt

aberrations that will produce a non-uniform grid of spots imaged by the Shack-Hartmann wavefront sensor system. The spot locations, one mapped to each lenslet, are used to evaluate the local gradient of the aberrated wave and can be reconstructed to produce a two-dimensional segmented version of the incoming wave. Measurement of local gradients and production of a resultant measured wavefront are formed utilizing tilt sensing methods and gridded optical path difference reconstruction matrices. The reconstruction matrices relate the measured local gradients to the wavefront nodes to produce an estimated wavefront fit to the uniform grid. [31]

Within the simulation, lenslet mapping sizes are chosen such that they are smaller than the smallest Fried parameter experienced. This is a key design parameter because if the lenslet mapping to the telescopes pupil plane were significantly larger than $r_0$ then the atmosphere induced tilt would no longer be the dominate aberration in each lenslet and then the measurements would not be representative of the true distorted wavefront present in the telescope's pupil. The Fried parameter and associated requirement for lenslet array size is pre-calculated after the chosen profile is generated and the atmospheric path propagation has taken place for the longest beacon range. In practice, the range of typical turbulence strengths for a measurement site is assumed and from this the lenslet mapping size can be determined. The lenslet mapping is typically a fixed value based on SNR constraints combined with desired spatial resolution required for accurately sensing the wavefront present in the pupil plane. For simulation purposes a 10 by 10 or larger grid of lenslets was used. This ensured enough measurements were made to reconstruct a meaningful wavefront and also matched well with the LIDAR equation based SNR model associated with the dynamically ranged Rayleigh beacon system. [51, 31]

*5.1.4 Profiled Turbulence Metrics*

In simulation, the turbulence strength modeled along the optical path and the phase screens used at each multi-step junction have known optical properties. These optical properties stem from an $r_0$ data metric which is calculated from an input $C_n^2$ strength profile applied to a controlled random phase screen generation. [49] These input metrics are used as truth data for comparison against the modeled data and outlined algorithm output. How well the algorithm's segmented $C_n^2$ outputs matched the input $C_n^2$ strength profile served as a merit function for evaluation. Two $C_n^2$ profiles used for simulation presented in this paper are shown in Figure 42.

From the simulated data, a method for exploitation of a dynamically ranged Rayleigh beacon system was evaluated. We utilized the Shack-Hartmann wavefront sensor zonal measurements to produce an $r_0$ metric based on the flatness of the wave, consistent with Fried's requirements for the measurement of $r_0$. This method is further explained by Equations 73 and 74 and the associated descriptions. We then utilized those metrics for estimation of $C_n^2$ based on subsequent layer measurements and Equation 72. This segmented estimate of $C_n^2$ was used as the final output and was compared against the simulation inputs. Due to the random nature of simulating phase screen representations of pupil distortions that result from a modeled turbulent volume one would expect small deviations between the estimated $C_n^2$ profile and the input data.

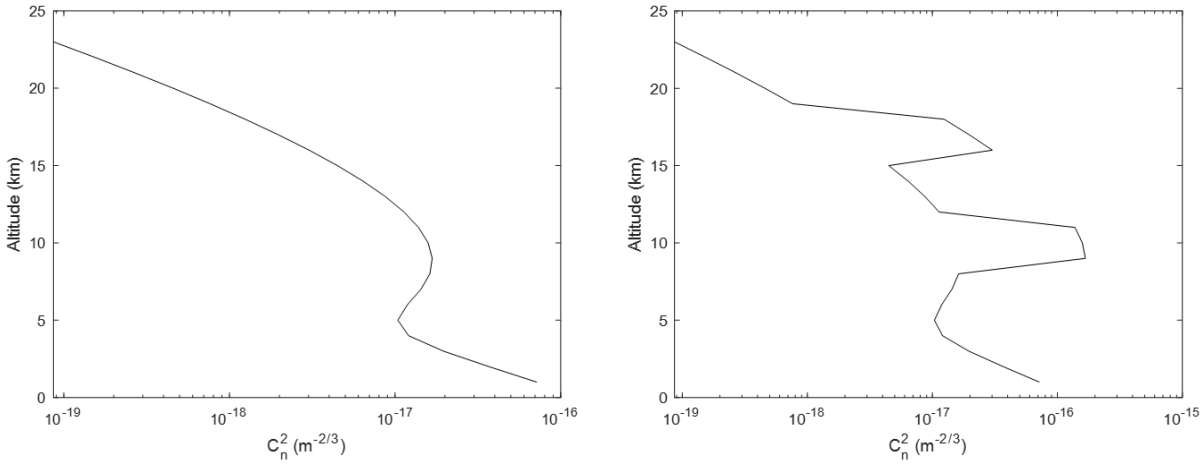


Fig. 42. The two turbulence strength profiles used for simulation

## 5.2 Algorithm Implementation and Evaluation

The data collection scenario consists of a dynamically ranged Rayleigh beacon where pupil plane wavefront estimation data is taken on a laser pulse by laser pulse basis in rapid succession such that the turbulent volume can reasonably be assumed to be stationary. Each individual pupil plane wavefront estimation data collect was done by a Shack-Hartmann wavefront sensor model and corresponds to a turbulent volume integrated along the viewing path. A projected phase screen was reconstructed from the Shack-Hartmann wavefront sensor data. Using the mean of the variance of the phase across the aperture $r_0$ can be estimated for the designated volume corresponding to the conic volume between the Rayleigh beacon and collecting aperture. Utilizing the collection of rapid succession measurements and Equation 72, $C_n^2$ segments can be estimated and combined to form an estimate of the $C_n^2$ strength profile.

### *5.2.1 Overview of Simulation Implemented*

The simulation consisted of an ensemble of 200 realizations for each input profile. Two of the profiles used are presented and are shown in Figure 42. The first is a standard Hufnagel-Valley 5/7

profile and the second is a Hufnagel-Valley 5/7 profile with enhanced turbulence strength localized in two altitude regions. The second profile is used to probe the algorithms effectiveness at locating strong changes in turbulence strength in neighboring stratified layers.

These refractive index structure parameters were used as the seed strengths for generation of pseudo-random Kolmogorov phase screens. The same random number generator seed was used for a single realization which consisted of many propagations from the beacon at the varied ranges to the collecting aperture. This assumption built into the simulation is intended for use of probing the algorithms effectiveness. In practice, the number of sequential measurements taken from varied path length ranges will depend on how long the atmosphere can be considered frozen, the speed of the optical shutter, the repetition rate of the laser system used, and the SNR of the returned laser light from a beacon making a phase estimation measurement possible.

The phase present at the collecting aperture was analyzed using a Shack-Hartmann wavefront sensor model. For the simulations presented in this paper a 10 by 10 lenslet grid was masked to a 60.96 cm circular aperture. This resulted in each sub-aperture's size extent being 6.096 cm which is smaller than any of the $r_0$ input values for a single beacon measurement. This ensures that wavefront tilt on a sub-aperture is the dominant aberration present. In the simulation, each lenslet region was approximately 100 pixels across and each resultant spot produced from a lenslet covered a 3 by 3 pixel box. The intensity distribution with the 3 by 3 box was used to estimate sub-pixel centroid location. The sub-pixel centroid, the location within the lenslet region of interest, and the lenslet focal length were used together to deduce the slope of the optical field present within a lenslet region. An example of the resultant slope vectors is shown in Figure 44. For this analysis focal shifts within the sensing system due to changing the range between the beacon and the aperture were neglected. In practice, changing the range of the beacon will shift the location of the

focus in a telescope system. The design of the optical relay and location of optical components such as the shutter used need to be chosen with careful consideration specific to the telescope used. It is possible under constraints to keep the Shack-Hartmann sensor in collimated space with mapped lenslet sizes remaining smaller than $r_0$. Therefore, for the simulated treatment this effect was ignored.

### *5.2.2 Zonal Measurements to Estimate $r_0$*

Each propagation produced one wavefront present at the collecting aperture. This was measured by the SHWFS. An example of the SHWFS system model used is shown in Figure 43 along with an example of the input wavefront seen by the sensing system which is the turbulence induced phase distortions present in the system's pupil used for analysis. Shown in Figure 44 is an example of the zonal gradients produced from the sensed wavefront and the resultant segmented reconstructed wavefront. The wave is sensed using a SHWFS which converts focused spots to local tilt measurements using a spot centroiding algorithm on the imaged focal plane. The resultant slopes from each centroid are representative of zonal tilts in the pupil. These tilts are used to reconstruct the wave using a matrix inversion reconstruction method. [31] From each reconstructed wave an estimate of the Fried parameter was produced based on wavefront variance statistics. In simulation, this was done by tiling the simulated phase present at the collection aperture with circular pupils representing the lenslets of the SHWFS. Each tile produced a tilt measurement that was converted into a zonal curvature through reconstruction. The mean of the variance of the phase across the aperture was then calculated to derive the Fried parameter. This is shown in Equation 73. The mean of the variance of the phase across the aperture is

$$\langle \sigma^2 \rangle = 0.134 \left( \frac{D}{r_0} \right)^{5/3} \tag{73}$$

where $D$ is the aperture diameter. [58] Manipulation of Equation 73 to solve for $r_0$ results in

$$r_0 = \frac{0.299D}{\langle \sigma^2 \rangle^{3/5}} \tag{74}$$

where this $r_0$ is a representative metric of the turbulence strength within the volume of a single beacon measurement, $D$ is the aperture diameter, and $\langle \sigma^2 \rangle$ is the mean of the variance of the estimated phase across the aperture that is built from the zonal tilt tiles reconstructed from the Shack-Hartmann wavefront sensor measured gradients. These single beacon measurements are accumulated and referenced as *1, 2, … j, j+1* where each measurement comes from a different beacon range. These are then used as inputs to Equation 72 to produce a segmented profile estimate of the atmospheric turbulence strength.

This methodology of using a SHWFS to estimate $r_0$ from a pupil image whose phase is corrupted by turbulence is susceptible to small errors that can propagate forward into the dynamically ranged Rayleigh beacon profiling algorithm. These errors could stem from the gridded lenslet array that is mapped to the pupil. Each lenslet provides a point estimate of the average tilt contour within the mapped region, which is the dominant aberration. However, high order aberrations do exist that are not captured by this methodology. Also, the mapping of the lenslets to the pupil inherently have discrete regions with sharp edges that may fall into non-ideal locations depending on the turbulence induced phase distortions present in the pupil. This has the potential to average a large tilt between two sub-apertures, thus reducing contributing terms to the variance. The opposite is also true, a large tilt may be entirely captured within one sub-aperture resulting in a large contributing term to the variance calculation. Since the turbulence induced phase distortions present in the pupil are random in nature, these effects should average out through many measurements. Additionally, the wavefront reconstruction process naturally reduces the influence of a single large spike in a local tilt measurement. However, the dynamically ranged Rayleigh

beacon profiling algorithm relies on a singular series of adjacent measurements to create a profile, and therefore is susceptible to small errors in singular turbulence strength profile estimations.

The phase incident on the collecting aperture associated with each realization is discretely sampled at a high rate as compared to the Fried parameter or number of lenslets in the sensing system. This is evident in comparing the example phase shown in Figure 43 to the reconstructed phase in Figure 44. The discretization level is chosen such that the width of a sub-aperture is smaller than the Fried parameter. This chosen region width mapped to the collecting aperture is equal to the physical diameter of a lenslet projected onto the primary mirror of the collecting telescope system. Due to the discretized down sampling nature of this physical process, small deviations from the truth metric could be induced. However, due to the constraints imposed, these small deviations should be minimized and will have minimal overall effect on the system.

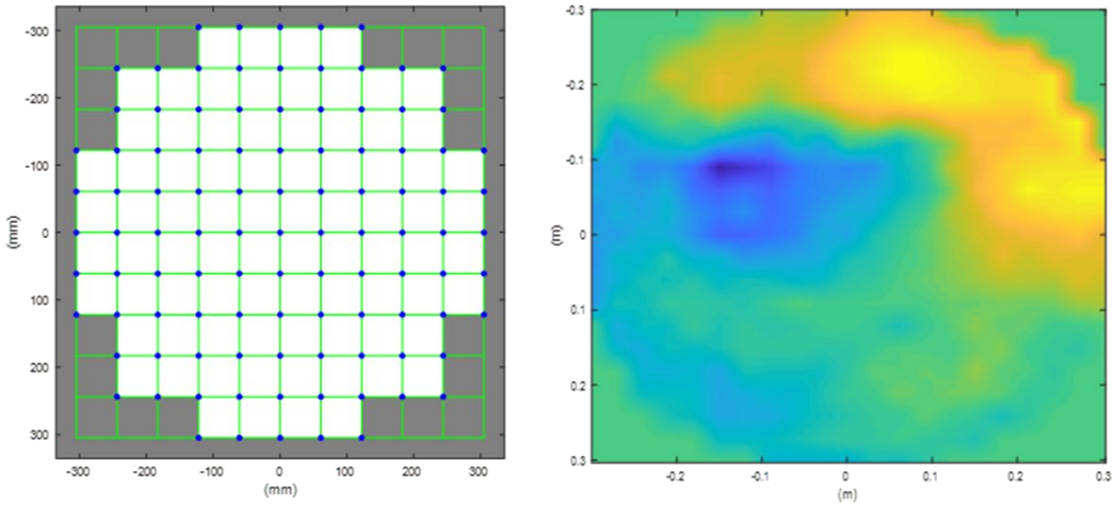


Fig. 43. (left) SHWFS model used for simulations, and (right) example of turbulence-induced phase distortions present in system's pupil

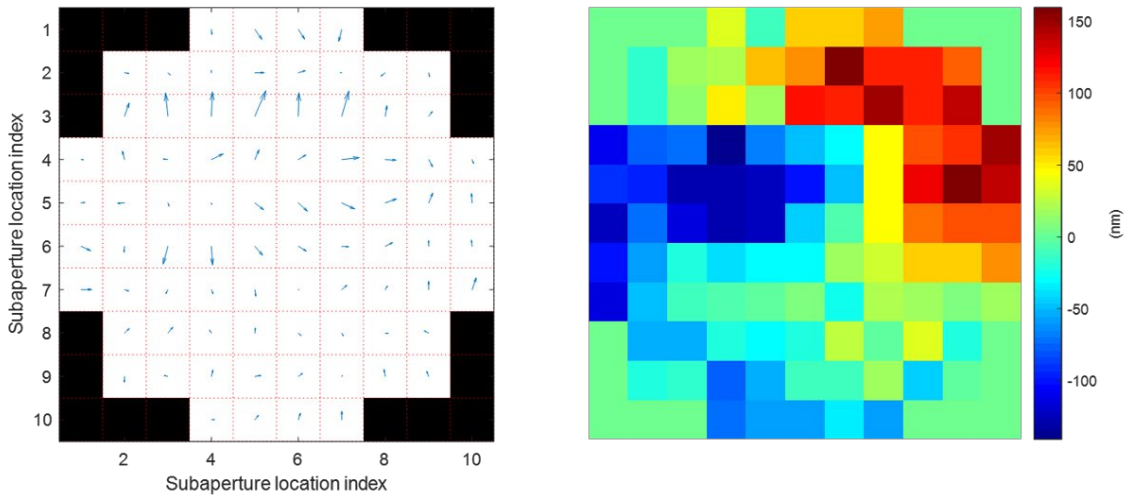


Fig. 44. Example of a wavefront (left) sensed and (right) reconstructed

From the measured zonal gradients and resultant reconstructed wavefronts the Fried parameter was estimated. Fried parameter estimates compared to true Fried parameters for the individualized beacon propagations are shown in Figure 45. Each data point in Figure 45 consisted of a propagation from a single altitude beacon to the sensing system. The sensing system then estimates an $r_0$ value from a reconstructed wavefront like that shown in Figure 44 to produce a single $r_0$ value. The $r_0$ value is estimated by manipulating Equation 73 to solve for $r_0$ as shown in Equation 74. Each black data point is from a series of $r_0$ estimates over the altitude range where the random number generation seed was controlled to be the same. The whole ensemble consists of 200 independent realizations each drawn as black data points. The true $r_0$ is plotted as a solid line and was used as the input metric for the simulation. The true $r_0$ is the approximate average of the estimated $r_0$ values comprising the whole ensemble.

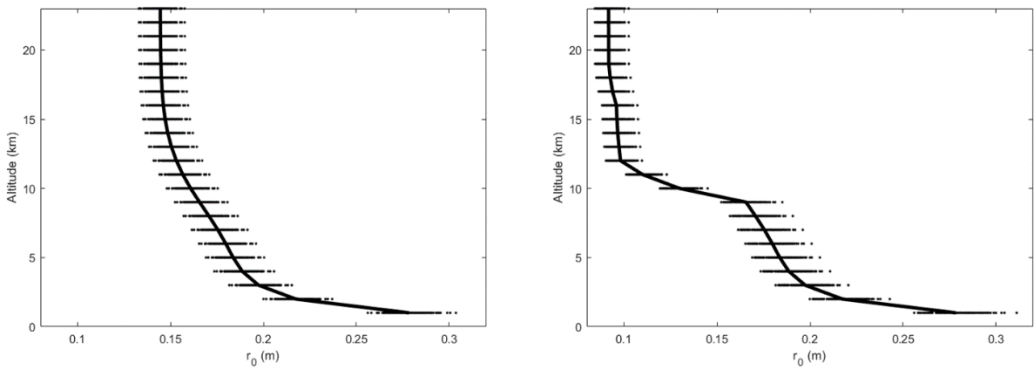


Fig. 45. Ensemble of $r_0$ versus altitude estimates (data points) compared to truth data (solid line). Note: $r_0$ decreases with altitude because the path length increases with each altitude step. (left) The standard Hufnagel-Valley 5/7 profile and (right) the Hufnagel-Valley 5/7 profile with enhanced turbulence strength localized in two altitude regions.

*5.2.3 Influence of Focal Anisoplanatism*

When choosing the locations of the dynamically ranged beacons, careful consideration needs to be taken to avoid negative effects associated with focal anisoplanatism. Focal anisoplanatism arises from the beacon geometry. The effects of focal anisoplanatism are typically minimized by placing the beacon as far away as possible. [31] However, for a dynamically ranged Rayleigh beacon system, the location of the beacon is intentionally varied and not at a maximized distance from the telescope. Additionally, the treatment of focal anisoplanatism is applied in a differential manner as opposed to the traditional treatment against a plane wave. This has to be done because of the unique dynamically ranged operation of the beacon system. Hardy [31] admittedly states that calculation of the focal anisoplanatism error has proved to be a difficult task, but provides a method developed by Belsher and Fried in 1994 [12] which has matched numerical evaluations within 1%. This metric for focal anisoplanatism error from a single beacon measurement is

$$\sigma_{FA}^2 = \left(\frac{D}{d_0}\right)^{5/3} \tag{75}$$

where D is the aperture diameter and $d_0$ is the diameter over the aperture in which the wavefront error due to focal anisoplanatism is less than 1 rad$^2$. For comparing subsequent dynamically ranged beacon measurements against each other while considering the effects of focal anisoplanatism $d_0$ needs to be derived. A single beacon $d_0$ can be described as

$$d_0 = \left\{k^2 \left[0.057\mu_0^+(H) + 0.500\frac{\mu_{5/3}^-(H)}{H^{5/3}} - 0.452\frac{\mu_2^-(H)}{H^2}\right]\right\}^{-3/5} \tag{76}$$

where H is the range to the beacon from the telescope, and $\mu_m$ is the turbulence moment described in terms of the upper and lower moments for m = 0, 5/3, and 2. The upper turbulence moment is

$$\mu_m^+(H) = \int_H^\infty C_n^2(z)z^m dz \tag{77}$$

and the lower turbulence moment is

$$\mu_m^-(H) = \int_0^H C_n^2(z)z^m dz. \tag{78}$$

Relating this to the dynamically ranged beacon scenario a differential metric can be developed which results in

$$\Delta d_0 = \left\{k^2 \left[0.057\left(\int_{H_k}^\infty C_n^2(z)dz - \int_{H_{k+1}}^\infty C_n^2(z)dz\right) + 0.500\left(\frac{\int_0^{H_k} C_n^2(z)z^{5/3}dz}{{H_k}^{5/3}} - \frac{\int_0^{H_{k+1}} C_n^2(z)z^{5/3}dz}{{H_{k+1}}^{5/3}}\right) - 0.452\left(\frac{\int_0^{H_k} C_n^2(z)z^2dz}{{H_k}^2} - \frac{\int_0^{H_{k+1}} C_n^2(z)z^2dz}{{H_{k+1}}^2}\right)\right]\right\}^{-3/5} \tag{79}$$

where k and k+1 represent two adjacent measurements from the dynamically ranged Rayleigh beacon system. This differential metric accounts for errors in focal anisoplanatism associated between subsequent beacon measurements, and can flow back into the treatment shown in Equation 75 to yield

$$\Delta\sigma_{FA}^2 = \left(\frac{D}{\Delta d_0}\right)^{5/3}. \tag{80}$$

It is shown in Equation 79 that the focal anisoplanatism error has a dependence on the integrated turbulence strength and beacon range. Without a priori knowledge of the turbulence strength profile it is difficult to calculate the effect that the focal anisoplanatism error will have on the

estimation accuracy of the segmented $C_n^2$ metric proposed by Equation 72. However, trends can be elucidated through ratio analysis. For subsequent dynamically ranged beacon locations that are in close spatial proximity the overall effect of focal anisoplanatism error is small. The backscattered field from the two beacons would experience nearly the same turbulence. If the distance between subsequent beacon measurement locations is large, the effect of focal anisoplanatism error could be relatively large. This could result in very different turbulence experienced by the backscattered fields from the two beacons, and consequently influence the accuracy of estimating the segmented turbulence strength along the path as described by Equation 72. To mitigate the negative effects of focal anisoplanatism, it is recommended that in the CONOPS planning for a data collect utilizing a dynamically ranged Rayleigh beacon the location choices for each individual beacon measurement be spaced in relatively close proximity to each other.

*5.2.4 Determination of Turbulence Profile ($C_n^2$)*

The refractive index structure parameter is estimated using the formulation shown in Equation 72 from data generated by the individual realization sequences that comprised a single random number generation seed. The $r_0$ data used is represented by the data shown in Figure 45. This resulted in values of the refractive index structure parameter that was compared to the initial data input in the simulation environment. The results are shown in Figure 46. The left graph is a Hufnagel-Valley 5/7 profile and the right graph is a Hufnagel-Valley 5/7 with two enhanced turbulence strength peaks. For the Hufnagel-Valley 5/7 profile the estimated $C_n^2$ profile data values have a mean absolute error of $4.00 \times 10^{-19}$ from the input data values. The mean of the estimated values is 0.11 standard deviations away from the truth input corresponding to a mean percent difference of 0.58%. These metrics show that the data processing algorithm agrees well with the input parameters.

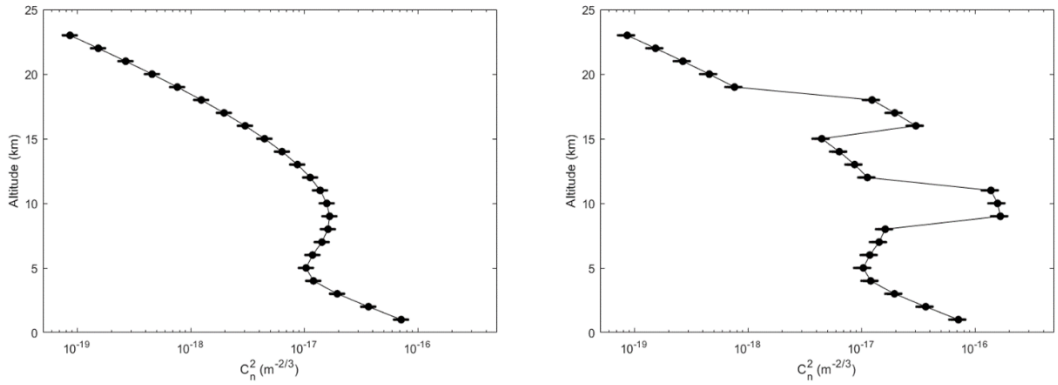


Fig. 46. Ensemble of $C_n^2$ estimates (data points) compared to truth input data (solid line). (left) The standard Hufnagel-Valley 5/7 profile and (right) the Hufnagel-Valley 5/7 profile with enhanced turbulence strength localized in two altitude regions.

## 5.3 Discussion

Utilization of individualized Fried parameter measurements in sequence to produce a discretized estimation of the turbulence strength profile is shown to produce quantitatively similar results in simulation to the inputted truth data. Analyzing the total ensemble of realizations, the $C_n^2$ estimates were only a fraction of a mean percent difference from the truth. This was expected based on the mathematical foundation of the profiling algorithm coupled with the small error that can propagate into the system from discretely modeling the wave propagations. These margins may grow for an operational system as larger errors in estimation may propagate through the system. Two examples of error creation sources are SHWFS centroiding imperfections in the presence of higher noise and unequal total SNR seen in the SHWFS spots for varied altitude range measurements.

The presence of localized turbulence strength spikes was realizable utilizing this framework as shown by the example case used in this paper. This example case was specifically designed with two high strength localized turbulence regions to test the proposed algorithm's ability to both

isolate the strength spikes and estimate their strength increases. This was achievable through simulation since prior knowledge of the location of the spikes was known and the dynamically ranged beacon altitude locations for subsequent wave propagations could be chosen such that the sampling and resultant profile resolution was adequate to capture the turbulence strength spike. In practice there could be practical limitations such as not knowing the location, thickness, or strength of a spike to capture the locational cutoff edges in range from the collecting telescope. Additionally, having a finite number of subsequent measurements achievable due to repetition rate limitations of the laser system coupled with the changing turbulence atmosphere time frames could bring the system outside of the frozen flow assumption. For example, if there are only 10 laser pulses available before the atmosphere changes to create a beacon source, then the measurements used will be few in number and will only be able to interrogate a fraction of the whole path in high resolution. To still have utility the system could be configured so that long benign paths could be set as a single integrated strength measurement since this methodology relies on the $r_0$ metric, and the part of the path where the profile structure exists could be configured to obtain closely spaced beacon measurements. This is a CONOPS choice an operator of a dynamically ranged Rayleigh beacon system would have to make. With proper CONOPS choices and small prior knowledge assumptions, it is possible to effectively utilize a low number of measurements in an efficient way to make measurement-based estimates of the turbulence strength profile utilizing the algorithm presented in this paper.

Furthermore, an algorithm like the one presented that is reliant on assessing the Fried parameter for the metric of merit may not be the most optimal solution, although it produces agreeable results. A dynamically ranged Rayleigh beacon system that utilizes wavefronts measured across the entire pupil of the imaging system at a resolution smaller than $r_0$ that also has an aperture that is many $r_0$ across inherently has spatial diversity in the tilt measurements. One could theorize that a hybrid

sensing algorithm could be employed that utilizes the differential-range measurements like those presented here enhanced by the use of the geometries of the spatial correlations of close and far neighboring tilt measurements on the SHWFS. The enhancement could come from treatment that is similar to that of a differential image motion LIDAR [16], but acting on the Shack-Hartmann slope measurements from differential range-stacked beacons. Alternatively, SLODAR-like processing could be employed, but the separation used to build up a measurement-based weighting function would come from sub-aperture separation and correlation from different range beacons. To accomplish this a new derivation of cross-path weighting functions would need to be developed and the consequences of beacon location choices would need to be considered. These methods could have an advantage of localized high resolution estimates of the $C_n^2$ parameter while also sweeping through a broad range of range gates. Employing these types of algorithms would make for a good follow-on research effort.

## 5.4 Conclusion

Atmospheric turbulence is known to be the limiting cause of image blur in many optical imaging systems. Consequently, a body of research has evolved over the years with ways to measure turbulence and mitigate its effects. As the imaging systems grow in resolution capability, overcoming turbulence effects will become all the more important. A crucial step to that will be understanding the profiled evolution of the turbulence along the viewing path. With this knowledge, advanced mitigation techniques and prediction techniques could be employed. To support future system capability trends, this paper presented an algorithm that could be applied to dynamically ranged Rayleigh beacon data to extract information about the strength changes along the propagation path. The modeling framework was created to investigate vignette scenarios that are represented of possible turbulence environments. Results were shown that supported correct

estimation of turbulence strength profiles and identification of localized strength spikes under properly configured range gated setups. In conclusion, the algorithm presented is able to adequately estimate the strength profile of optical turbulence along viewing path utilizing wavefront data obtained from a dynamically ranged Rayleigh beacon based system. [52]

# VI. Focal Anisoplanatism Influence on Dynamically Ranged Rayleigh Beacons

## 6.0 Introduction

Information presented in this section was taken from a sub-section of the SPIE peer reviewed Applied Optics Journal article [52] and a conference paper presented at the SPIE Unconventional Imaging and Adaptive Optics Conference in 2020. [53]

Long-range optical imaging applications are typically hindered by atmospheric turbulence. The pseudorandom variations in the index of refraction are the physical observables resulting from atmospheric turbulence. This effect leads to unwanted optical blurring of the image. As a result, there is a need to understand how these pseudorandom variations in the index of refraction behave and evolve along the viewing path. Furthermore, knowledge of the profile strength of the index of refraction structure parameter can lead to mitigation strategies for combating the undesired effects. A previously presented conceptual turbulence profiling system strategy [54] and measurement approach [52] have been developed for measuring the strength of the refractive index structure parameter path variations utilizing a dynamically ranged Rayleigh beacon system. A dynamically ranged Rayleigh beacon system is a modification of the traditional Rayleigh beacon system design to allow for the originating location of the backscattered field to change in the range from the collecting aperture of the telescope. When this dynamically ranged methodology is employed, a new set of data processing algorithms can be used to extract information about localized turbulence strength contributions. Whereas a traditional laser beacon system produced just a single volumetric estimate of the turbulence strength. When making multiple ranged based measurements in fast succession for use in a differential measurement schema, it becomes imperative to understand the influence of subsequent beacon focal anisoplanatism measurement effects. These effects, if not

appropriately mitigated for in the configuration of the dynamically ranged Rayleigh beacon system, could render the differential-based measurements inaccurate.

Rayleigh beacons used to sense the strength of the turbulence along an optical path are subject to undesirable effects on a measurement due to focal anisoplanatism. It is commonly referred to as the cone effect and manifests from unsampled turbulence at the edges of the pupil. The evaluation of focal anisoplanatism is fairly well understood for traditional Rayleigh beacon systems. However, for a dynamically ranged Rayleigh beacon system that utilizes beacon measurements from many varied finite ranges to build a tomographic profile of the turbulence strength, the understanding of focal anisoplanatism becomes all the more important and has not been thoroughly investigated. Focal anisoplanatism effects on a dynamically ranged Rayleigh beacon measurement system are presented to quantify the resultant influence on the accuracy of the beacon system's ability to produce tomographic turbulence strength profile estimations.

The scenario of interest is that of a dynamically ranged Rayleigh beacon depicted in Figure 47. Due to the finite range of the Rayleigh beacon the system will experience focal anisoplanatic effects. The analysis is similar to that of a static beacon at a finite range compared to a point at infinite range, which is the traditional analysis most commonly presented. However, since the beacon is not at a singular finite fixed range, the effects need to be compared against each measurement of the beacon showing the resultant overall effect on the system. The main effect analyzed further in the remaining portion of this paper is focal anisoplanatism. One can gain intuition about this by observing traits of the dynamic beacon from the graphic in Figure 47. Notice that each beacon will not experience all the turbulent layers, and how the cone produced by a single beacon takes up a slightly different volume as compared to a neighboring beacon. In the notional graphic example beacon one experiences three turbulence layers whereas beacon two only

experiences two. The number of layers of turbulence experienced by a beacon will be unique to the configured range of the specific laser pulse used to generate the beacon. [52] Also, notice that at turbulent layer two and three in Figure 47 that the area sampled by the beacon is smaller for the beacons that are closer to the collecting aperture. A smaller sampled area will manifest as lower order aberrations as seen by the sensing system. Therefore, the location of strong atmospheric layers of turbulence as compared to the dynamic beacon choices will have a large impact on the focal anisoplanatic effects seen by the system. A typical atmospheric turbulence scenario is described by Hufnagel and is shown to have two strong turbulent layers: one near the ground at the inversion layer and one at higher altitudes most commonly associated with a strong wind band. [41]

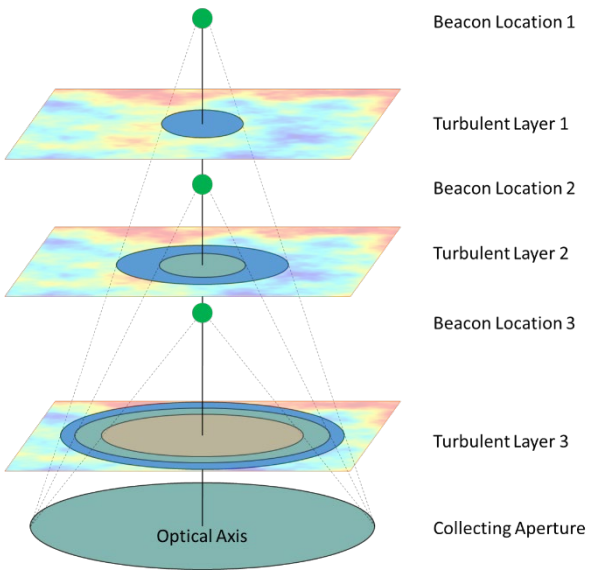


Fig. 47. Notional dynamic beacon collection scenario displaying a three beacon collecting scenario.

## 6.1 Key Concepts Supporting the Analytic Treatment

*6.1.1 Turbulence and Aerosol Research Dynamic Interrogation System (TARDIS)*

The Turbulence and Aerosol Research Dynamic Interrogation System (TARDIS) is a Rayleigh beacon based atmospheric turbulence measurement system. A notional depiction of TARDIS is shown in Figure 48. The output from this system is a sensed atmospheric turbulence distorted wavefront measured by a Shack-Hartmann wavefront sensor. From this wavefront an estimate of the Fried parameter, $r_0$, is possible. What makes TARDIS novel is the ability to perform dynamic ranging through the use of a programmable optical shutter system that is sequenced to the outgoing pulses of the on-axis laser launch system. Taking measurements in a rapid succession that the atmosphere can be assumed to be near-frozen as viewed by the light sensing system allows for utilization of multiple measurements within the short timeframe to produce an estimate of the profile of the atmospheric turbulence strength. [52] As depicted conceptually in Figure 47, sequential beacon measurements can have contributions to a measured wavefront that come from not just the region between the beacons, but also the edges of the sensed cone. This is a focal anisoplanatism effect that has to be minimized as to not influence the estimate of $r_0$ as produced by the Shack-Hartmann based wavefront measurement.

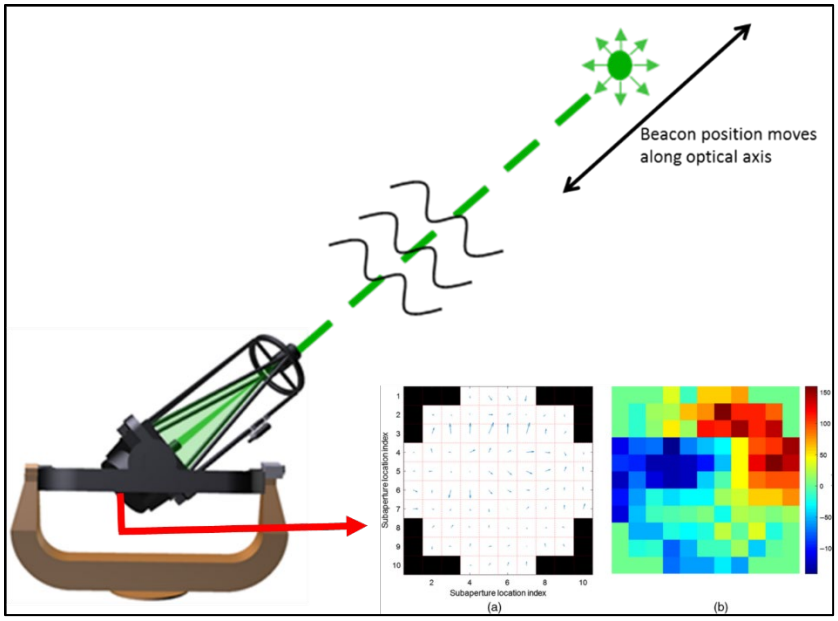


Fig. 48. Notional depiction of the Turbulence and Aerosol Research Dynamic Interrogation System (TARDIS).

*6.1.2 Focal Anisoplanatism*

Negative effects of focal anisoplanatism influence the choice of beacon locations as part of the TARDIS CONOPS setup. The focal anisoplanatism stems from the varied range beacon geometry. Traditional Rayleigh beacons minimize the effects of focal anisoplanatism by placing the beacon as far away as possible from the telescope. [31] However, TARDIS operation intentionally places beacons closer to the telescope to aid in mapping out localized strength change in the refractive index structure parameter $C_n^2$. [52] Additionally, TARDIS operation needs to take a different view towards focal anisoplanatism as compared to a traditional Rayleigh beacon. Since the range to each beacon is different when building up a turbulence strength profile, the beacon to beacon focal anisoplanatism needs to be considered.

The calculation of focal anisoplanatism error has been shown to be a tough task, as stated by Hardy [31], but Hardy does provide a method that has had proven success. This was developed by Belsher and Fried in 1994 [12] and matched numerical evaluation within 1%. The metric for focal anisoplanatism error from a single beacon measurement is

$$\sigma_{FA}^2 = \left(\frac{D}{d_0}\right)^{5/3} \tag{81}$$

where $D$ is the aperture diameter and $d_0$ is the diameter over the aperture in which the wavefront error due to focal anisoplanatism is less than 1 rad$^2$. Here $d_0$ can be described as

$$d_0 = \left\{k^2\left[0.057\mu_0^+(H) + 0.500\frac{\mu_{5/3}^-(H)}{H^{5/3}} - 0.452\frac{\mu_2^-(H)}{H^2}\right]\right\}^{-3/5} \tag{82}$$

where $H$ is the range to the beacon from the telescope, and $\mu_m$ is the turbulence moment described in terms of the upper and lower moments for $m$ = 0, 5/3, and 2. The upper turbulence moment is

$$\mu_m^+(H) = \int_H^\infty C_n^2(z)z^m dz \tag{83}$$

And the lower turbulence moment is

$$\mu_m^-(H) = \int_0^H C_n^2(z)z^m dz. \tag{84}$$

This treatment quantifies the focal anisoplanatism error for a singular beacon as compared to an infinitely far source. [31] However, for the TARDIS CONOPS $d_0$ needs to be derived for one beacon location compared to the next closest location. This will be referred to as $\Delta d_0$ and is calculated as

$$\Delta d_0 = \left\{k^2\left[0.057\left(\int_{H_k}^\infty C_n^2(z)dz - \int_{H_{k+1}}^\infty C_n^2(z)dz\right) + 0.500\left(\frac{\int_0^{H_k} C_n^2(z)z^{5/3}dz}{{H_k}^{5/3}} - \frac{\int_0^{H_{k+1}} C_n^2(z)z^{5/3}dz}{{H_{k+1}}^{5/3}}\right) - 0.452\left(\frac{\int_0^{H_k} C_n^2(z)z^2dz}{{H_k}^2} - \frac{\int_0^{H_{k+1}} C_n^2(z)z^2dz}{{H_{k+1}}^2}\right)\right]\right\}^{-3/5} \tag{85}$$

where $k$ and $k+1$ represent two adjacent measurements from the dynamically ranged Rayleigh beacon system. [52] $\Delta d_0$ can be inserted back into Equation 81 to

$$\Delta\sigma_{FA}^2 = \left(\frac{D}{\Delta d_0}\right)^{5/3}. \tag{86}$$

It is shown in Equation 85 and 86 that the focal anisoplanatism error has a dependence on the integrated turbulence strength and beacon range. Without a priori knowledge of $C_n^2$, it is tough to calculate the influence that the focal anisoplanatism error will have on the estimation accuracy of the segmented $C_n^2$ metric. Overall trends can be elucidated by performing a ratio analysis. This leads to stating that closely spaced beacons will have a relatively small focal anisoplanatism error, and the opposite is true for large separations. This makes physical sense as closely spaced beacons would experience turbulent volumes that are more similar than that of beacons with large separations. [52] The ratio analysis and physical intuition is helpful, but further insight is needed when setting up the TARDIS CONOPS. Since there is an influence of localized turbulence strength on measurement accuracy when the goal is to measure the localized turbulence strength, measurement setup can be challenging when needing to ensure measurements taken are accurate and have minimized the effects of focal anisoplanatism. Calculations presented and analyzed in this paper will provide a basis to quantify the coupled focal anisoplanatism error and turbulence strength influence on the turbulence strength profile estimation, providing a path forward to an operator designing the CONOPS for a dynamically ranged Rayleigh beacon system like TARDIS.

## 6.2 Turbulence Profiles Used for Analysis

Multiple turbulence models were used as part of this analysis, shown in Figure 49. The models chosen were constant strength profiles at $10^{-15}\,m^{-2/3}$, $10^{-16}\,m^{-2/3}$, and $10^{-17}\,m^{-2/3}$ to highlight errors due to focal anisoplanatism associated with turbulence strength magnitudes, and Hufnagel-Valley (HV) based profiles with $r_0$ values of 5 cm, 10 cm, and 15 cm and isoplanatic angles of 1.4 arc seconds, 2.1 arc seconds, and 2.5 arc seconds, respectively. The governing equation for the HV model is shown in Equation 87 using values from Table 3 as

$$C_n^2(h) = Aexp\left(-\frac{h}{H_A}\right) + Bexp\left(-\frac{h}{H_B}\right) + Ch^{10}exp\left(-\frac{h}{H_C}\right) + Dexp\left(-\frac{(h-H_D)^2}{2d^2}\right). \quad (87)$$

Table 3. Constants used in turbulence model in Equation 87.

| **A (E-15)** | **$H_A$ (m)** | **B (E-17)** | **$H_B$ (m)** | **C (E-53)** | **$H_C$ (m)** | **D (E-16)** | **$H_D$ (m)** | **$r_0$ (m)** | **$\theta_0$ (arc sec)** |
|---|---|---|---|---|---|---|---|---|---|
| **17** | 100 | 27 | 1500 | 3.59 | 1000 | 0 | - | 0.05 | 1.4 |
| **4.5** | 100 | 9 | 1500 | 2.0 | 1000 | 0 | - | 0.10 | 2.1 |
| **2.0** | 100 | 7 | 1500 | 1.54 | 1000 | 0 | - | 0.15 | 2.5 |

The last terms in Equation 87, denoted by the variable or subscript *D*, can be used to insert in a strong turbulent layer into the HV turbulence strength profile. The varied strength HV profiles were chosen as they add more realism as compared to a constant profile and will also be able to highlight the effects of focal anisoplanatic errors. In the non-constant profile it will be shown that stronger turbulence will have a stronger effect on the focal anisoplanatic error associated between two beacons that are separated with strong turbulence between them. This relation is also shown through ratio analysis with inspection of Equation 86.

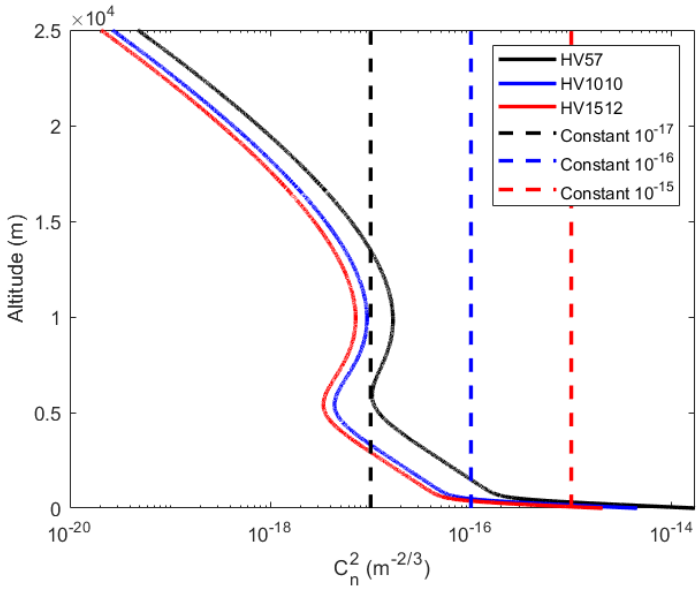


Fig. 49. Turbulence profiles used for analysis.

### 6.3 Evaluation of Focal Anisoplanatism Effects

An evaluation of the types of focal anisoplanatism effects that could be experienced by the TARDIS system were calculated. This was done to examine the focal anisoplanatism error (FAE) associated between two spatially neighboring pulses used as part of the TARDIS methodology for producing a tomographic profile of the strength of the atmospheric turbulence. The formulation of FAE using Equations 85 and 86 were used with turbulence strength inputs from Figure 49. This was done for varied separations of the spatially neighboring pulses used as part of the TARDIS methodology. Separation distances used were 0.25 km, 0.5 km, 1.0 km, 2.0 km, 4.0 km, and 8.0 km. This resulted in quantitative metrics for the FAE as well as $\Delta d_0$ which represents the aperture diameter over which the FAE is less than 1 rad$^2$. Results from these calculations are shown in Figures 50 through 55.

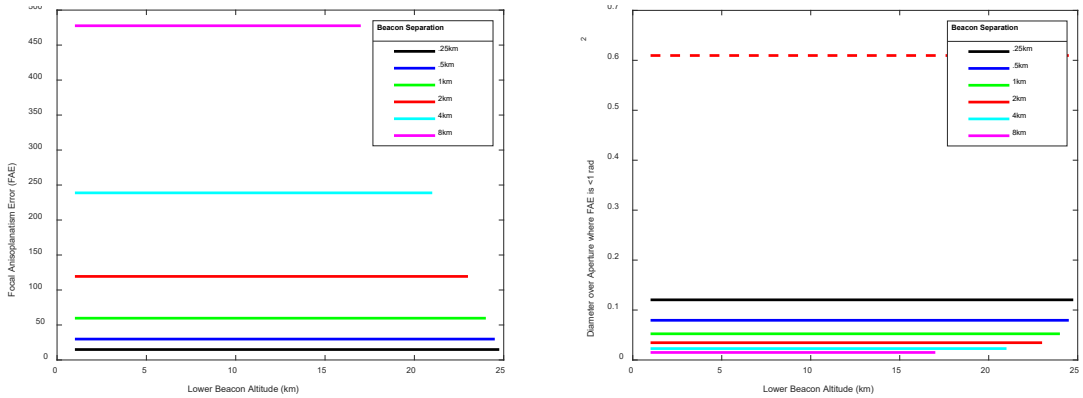


Fig. 50. (left) Focal anisoplanatism error and (right) $\Delta d_0$ for beacon heights plotted at the lower of the two beacon heights for varied beacon separations for an input constant $C_n^2$ profile of $10^{-15}$ $m^{-2/3}$. The dashed red line shows the aperture diameter of the TARDIS.

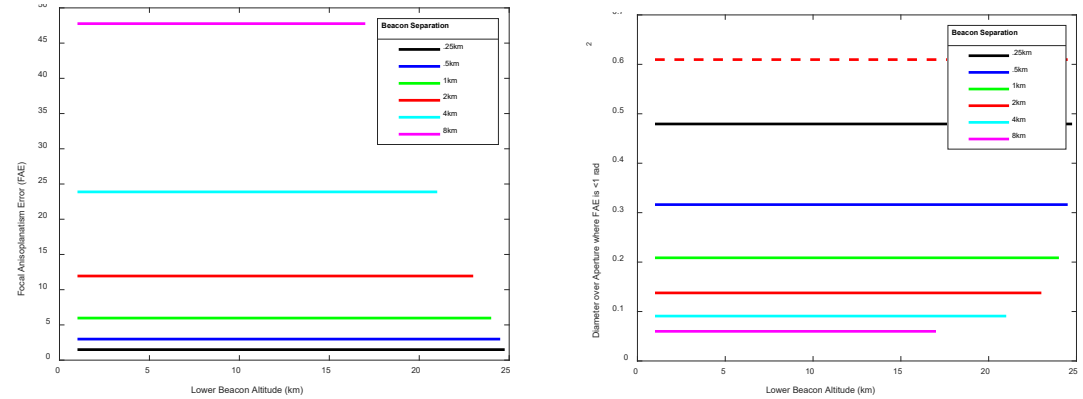


Fig. 51. (left) Focal anisoplanatism error and (right) $\Delta d_0$ for beacon heights plotted at the lower of the two beacon heights for varied beacon separations for an input constant $C_n^2$ profile of $10^{-16}$ $m^{-2/3}$. The dashed red line shows the aperture diameter of the TARDIS.

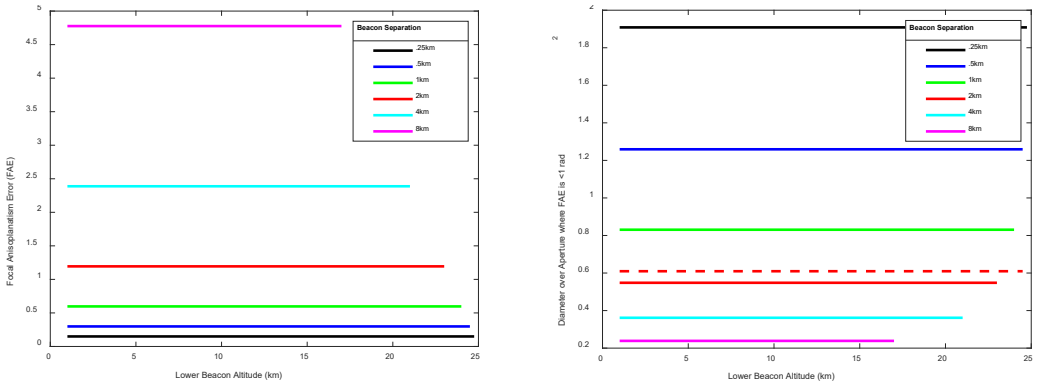


Fig. 52. (left) Focal anisoplanatism error and (right) $\Delta d_0$ for beacon heights plotted at the lower of the two beacon heights for varied beacon separations for an input constant $C_n^2$ profile of $10^{-17}$ $m^{-2/3}$. The dashed red line shows the aperture diameter of the TARDIS.

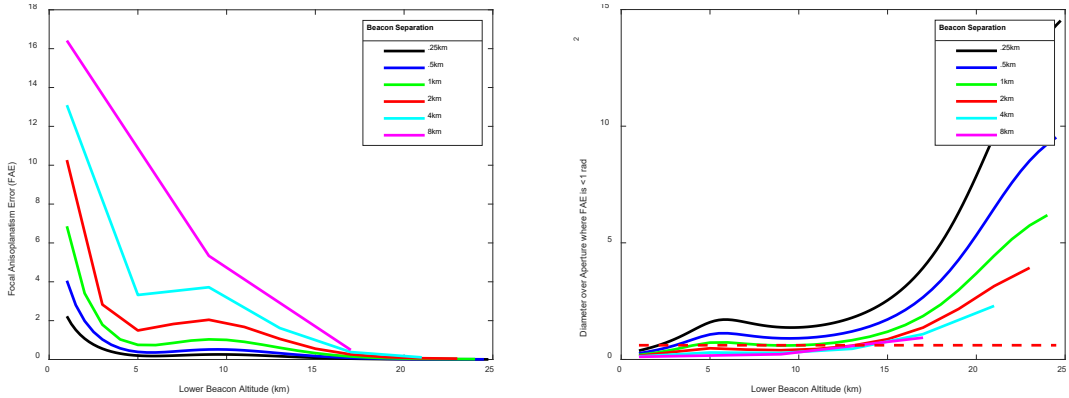


Fig. 53. (left) Focal anisoplanatism error and (right) $\Delta d_0$ for beacon heights plotted at the lower of the two beacon heights for varied beacon separations for an input Hufnagel-Valley $C_n^2$ profile with $r_0$ of 5 cm and an isoplanatic angle of 1.4 arc seconds. The dashed red line shows the aperture diameter of the TARDIS.

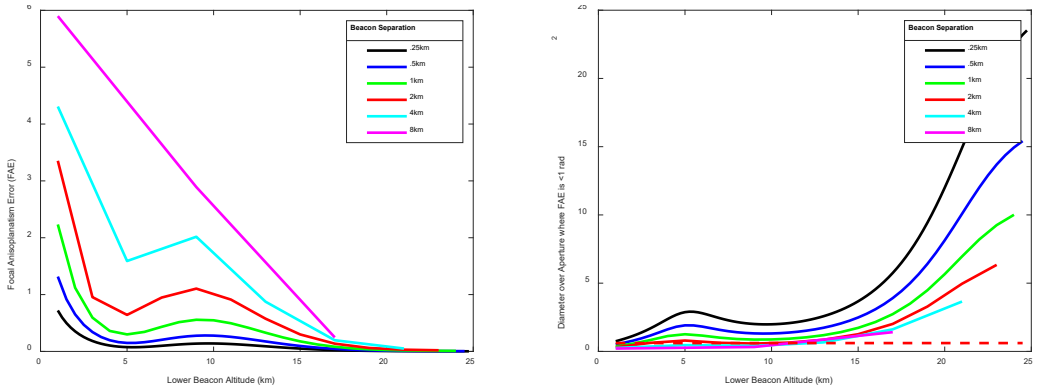


Fig. 54. (left) Focal anisoplanatism error and (right) $\Delta d_0$ for beacon heights plotted at the lower of the two beacon heights for varied beacon separations for an input Hufnagel-Valley $C_n^2$ profile with $r_0$ of 10 cm and an isoplanatic angle of 2.1 arc seconds. The dashed red line shows the aperture diameter of the TARDIS.

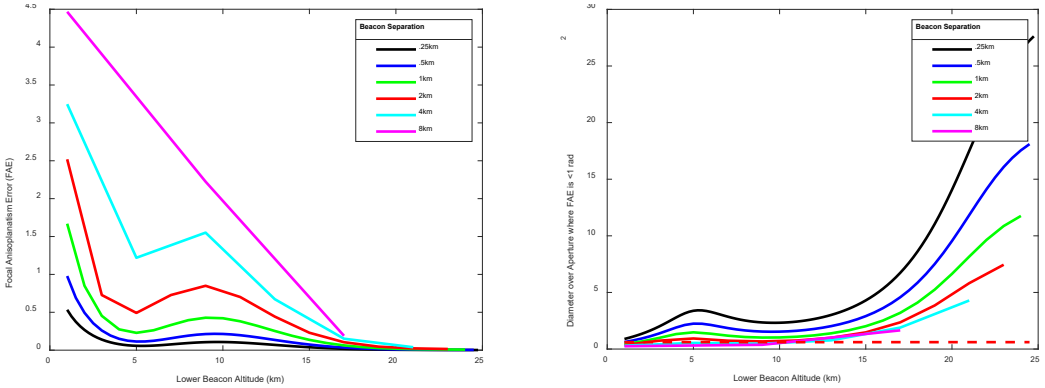


Fig. 55. (left) Focal anisoplanatism error and (right) $\Delta d_0$ for beacon heights plotted at the lower of the two beacon heights for varied beacon separations for an input Hufnagel-Valley $C_n^2$ profile with $r_0$ of 15 cm and an isoplanatic angle of 2.5 arc seconds. The dashed red line shows the aperture diameter of the TARDIS.

## 6.4 Discussion

When analyzing the results as shown in Figures 50 through 55 there are some noticeable trends associated with beacon separation and turbulence strength. The parameters $\Delta\sigma_{FA}^2$ and $\Delta d_0$ are the metrics used for merit. Both beacon separation and turbulence strength have an intertwined influence on these focal anisoplanatism error metrics. Constant magnitude turbulence profiles were used to investigate the effect of only the beacon separation. Three constant magnitude turbulence profiles, results in Figures 50 through 52, were used and represent mild, medium, and strong turbulence. Within all three of these setups, as beacon separation increased, the focal anisoplanatism error increased. In the $\Delta d_0$ plots within these figures the dashed red line represents the diameter of the TARDIS systems collecting aperture. For the mild turbulence, magnitude of $10^{-17}$ $m^{-2/3}$, the $\Delta d_0$ value is larger than the TARDIS collecting aperture for beacon separations of 1 km or smaller. For the medium and strong constant turbulence cases, the $\Delta d_0$ is smaller than the TARDIS collecting aperture for all separation cases investigated. However, constant magnitude turbulence profiles are not realistic and are only an indicator of the turbulence strength influence on the focal anisoplanatism error. Overall, the trend is the stronger the turbulence is, the larger the focal anisoplanatism error will be. Larger separations will experience more turbulence and consequently the focal anisoplanatism error will grow faster.

A turbulence profile that is closer to an average realistic profile the TARDIS system could experience is that of the Hufnagel-Valley $C_n^2$ profiles. Profiles used were HV57, HV1010, and HV1512, each having the similar profile structure at varied magnitude levels representing strong, medium, and mild turbulence scenarios. Results showing $\Delta\sigma_{FA}^2$ and $\Delta d_0$ for these profiles are shown in Figures 53 through 55. In the $\Delta\sigma_{FA}^2$ plots, these figures show the same trend for beacon separation; as the separation increases the focal anisoplanatism error increases. Of particular interest to users of the TARDIS, identifying beacon separations where the $\Delta d_0$ is larger than the

collecting aperture is of interest. HV57 is the most stressing case. Shown in Figure 53 there are key regions of the atmosphere where specific beacon separations have $\Delta d_0$ values that are larger than the TARDIS collecting aperture, shown as a dashed red line in the plots. A zoom in on the key section around the TARDIS collecting aperture size is shown in Figure 56. Above 2 km beacon separations, .25km have $\Delta d_0$ values above the TARDIS collecting aperture size. Similarly, the same effect is observed above 3 km for separations of .5km, 4 km for separations of 1 km, 13 km for separations of 2 km, 14 km for separations of 4 km, and 17 km for separations of 8 km. In Figures 53 through 56, the turbulence regional strength increase is noticeable at a central beacon altitude of 10 km. For TARDIS or a similar system, this regional strength increase in turbulence could play an important role in beacon separation choice. This is highlighted in Figure 56 by the green curve representing 1 km separations. Here the curve briefly drops slightly below the collecting aperture size of the TARDIS approximately at beacons located at 9 and 10 km. This is important as strength spikes in turbulence could lead to data measurement errors that stem from the focal anisoplanatism error resulting in inaccurate estimates of $C_n^2$ using algorithms similar to that previously presented. [54]

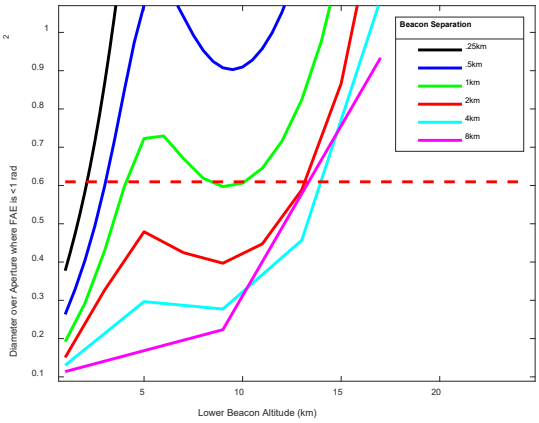


Fig. 56. Zoomed plot of $\Delta d_0$ for beacon heights plotted at the lower of the two beacon heights for varied beacon separations for an input Hufnagel-Valley $C_n^2$ profile with $r_0$ of 5 cm and an isoplanatic angle of 1.4 arc seconds. The dashed red line shows the aperture diameter of the TARDIS.

Relating trends on focal anisoplanatism error stemming from turbulence strength and beacon separation effects, a CONOPS framework can be developed that optimizes the dynamically ranged beacon configuration so that data collection results in an accurate estimation of the $C_n^2(h)$ parameter. As an example, an assumed profile can be the starting point, such as a Hufnagel-Valley average profile and another profile derived from local weather parameters. From this a calculation of $\Delta d_0(h)$ can be estimated for a range of beacon separations and compared against the systems collecting aperture. This informs an initial configuration of the dynamically ranged Rayleigh beacon CONOPS choices where a parameter such as beacon location can be chosen to have inter-beacon spacing well less than the predicted metrics. This study suggests at low altitudes closely spaced beacons are required, but as altitude is increased, the turbulence strength decreases and allows for beacon separations to increase. After initial measurements are made and an estimated profile of $C_n^2$ is developed, an adaptive beacon spacing could be used to reduce the amount of data collected and focus collection on regions where turbulence is strong. Additionally, these focal

anisoplanatism metrics will inform how many subsequent neighboring beacons can be used in a comparator algorithm to produce a $C_n^2$ profile. In cases where multiple beacon locations can be used together while keeping focal anisoplanatism errors low, the resultant estimation of $C_n^2$ will be enhanced. This methodology is a pathway towards guiding the CONOPS choices so that data collection is focused on regions of high interest where turbulence is locally strongest.

## 6.5 Conclusion

This section presented the framework for evaluating the data measurement errors associated with focal anisoplanatism for the data collection scenario of a dynamically ranged Rayleigh beacon. These errors have an influence on the estimation accuracy of $C_n^2$ and could potentially be present without an indicator in the data collected. Therefore, it is imperative that prior knowledge of the turbulent environment be known or an estimation of the profile be assumed so that a CONOPS configuration can be generated that is well within the bounds of significant error influence. The analysis in this paper provided a starting point specific to the TARDIS system using average Hufnagel-Valley profiles. These are realistic to what could be an average turbulence environment experienced by TARDIS. Results showed that beacon separation configurations existed that are well within the capabilities for TARDIS operation and could result in an accurate $C_n^2$ profile to be estimated. Additionally, this analysis showed that at higher altitudes the requirement for the separation of beacons that could be used could be relaxed. This is important as the returned flux of the signal for higher altitude beacons is weaker and a longer path integration of the beacon is required. Lastly, using this formulation of focal anisoplanatism error analysis in post-processing allows for selection of beacons that can be used for differential processing against each other. In some cases this could be more than two beacons which would add additional fidelity to the estimation of $C_n^2$ using differential $r_0$ measurements under a dynamically ranged beacon scenario.

# VII. Implications of Polarized Pupil Degradation Due to Focal Shifts in Dynamically Ranged Rayleigh Beacons

## 7.0 Introduction

This section is based on an accepted peer reviewed OSA Applied Optics journal article. [55] This journal article was chosen for an Editor's Choice Award and was one of the top ten OSA downloads for the month of February 2021.

A dynamically ranged pulsed Rayleigh beacon utilizing sensed wavefronts across the system's pupil plane is a novel method for tomographic quantification of the atmospheric turbulence strength. This method relies on relaying light from the telescope system's pupil plane to a wavefront sensor and having precise control of light-blocking mechanisms to filter out scattered light from the unwanted scattering regions along the propagation path. In order to accomplish this, unique design features were tested and incorporated into the sensing system. Dynamically changing the range of the beacon source created focal shifts along the optical axis in the telescope sensing system. This effect induced polarization degradation in the optical pupil. As a result, polarization non-uniformity within the Pockels cell resulted in light leakages that corrupted the sensed data signals. To mitigate this unwanted effect, a novel analysis of the polarization pupil had to be completed for the range of possible Rayleigh beacon source distances, relating the change in polarization to the ability of a Pockels cell to function as an optical shutter. Based on the resultant polarization pupil analysis, careful design of the light relay architecture of the sensing system had to be taken in order to properly capture sensed wavefront data from a series of intended ranges. Results are presented for the engineering design of the Turbulence and Aerosol Research Dynamic Interrogation System (TARDIS) sensing system showing the choices made within the trade space and how those choices were made based on the analysis of the polarization pupil. Based on what

was learned, recommendations are made for effectively implementing a polarization-based Pockels cell shutter system as part of a dynamically ranged Rayleigh beacon system.

### *7.0.1 Motivation*

Measuring atmospheric turbulence to correct for aberrations in an image has been of interest to the scientific community for a great length of time. Traditionally, a wavefront sensor is used to measure the corrections needed in the pupil plane of a system, but this provides no information about the turbulence strength profile along the path. It is a path-integrated measurement, but has been sufficient for adequate image correction historically. However, as ranges become farther, wide fields become desired, and as telescope apertures become larger the turbulence effects become more pronounced and path-integrated techniques fail to provide adequate image correction. [46] Born out of a need, vertical profiling techniques were conceived, modeled, tested, and integrated in adaptive optics assisted imaging programs. [30, 3, 5] Two well accepted techniques for producing vertical profile of atmospheric turbulence strength are SCIDAR and SLODAR. [40, 56] These methods, among others, inform systems and researchers to some level of the path resolved turbulence strength and aid in driving adaptive optics systems.

When scintillation and anisoplanatism become dominant effects, such as in deep turbulence, adaptive optics compensation becomes notably challenging. In deep turbulence, conventional adaptive optics schemes have inadequate performance. As such, new approaches need to be conceived. Tyler [17] provides a summarizing quantification of some of the leading approaches. Of significance, multi-conjugate adaptive optics (MCAO) technology holds promise. In theory, MCAO systems could reduce anisoplanatism and in the limit eliminate anisoplanatism. As a way to overcome the field of view limitations of conventional adaptive optics systems, Beckers (1989)

[19] proposed this concept of MCAO. Shortly after that, Tallon and Foy (1990) [37] introduced the concept of tomography to the problem set of atmospheric turbulence. The idea was to resolve turbulence strength with altitude from independent measurements from a number of reference sources. [43] Using these MCAO concepts three-dimensional turbulence representation can be obtained allowing for correction along any line of sight within the field of regard contained by the reference stars. [8] These techniques in conjunction with multiple laser guide star systems have been accepted and employed at a number of observatories where large aperture and field of regard telescopes exist. [34] However, atmospheric tomography where there is a desire to compensate in real time for the rapidly changing distortions has led to computational burdens [44], whether for adapting to deep turbulence or large telescope extended field of view requirements. With this in mind and using aspects from these concepts, a dynamically ranged Rayleigh beacon system concept was formulated with goals of producing profiled strength estimates of turbulence along the optical path with a significantly lessened computational burden.

### *7.0.2 Problem Description*

A method has been developed for sensing the tomographic strength of optical turbulence along the viewing path of a telescope system. [54] This method employs a novel dynamically ranged Rayleigh beacon and is referred to as a research system called the TARDIS. [51] The dynamically ranged aspect of this system resulted in engineering challenges that had the potential to limit the utility of producing tomographic measurement estimations of the turbulence strength present along the viewing path. One challenge involved maintaining high contrast ratio blocking by the optical shutter without light leakages for all dynamically ranged beacon configurations. Maintaining high contrast ratio blocking posed a challenge unique to this sensing methodology because changing the range to the beacon inherently shifts the focus within the sensing system. The shift in focus is inherent to any dynamically ranged Rayleigh beacon concept. Alternative concepts to those

employed by TARDIS exists. Most notable is that of a dynamic refocus system which does eliminate the light leakage problem [8, 28, 36] However, using a dynamic refocus system does include moving parts within the sensing system which could lead to a limiting factor in how fast a system like TARDIS could operate which would limit the tomographic range resolution for estimating turbulence strength. The TARDIS system does not focus the outgoing beacon at different ranges, but alternatively uses an on-axis collimated beacon where range to the beacon is controlled purely by an electronic shutter in the sensing system. This solution has no physically moving parts. The TARDIS system utilizes a Pockels cell and control of the polarization state of the light to act as a fast optical shutter for the sensing system. However, the focal point in the sensing system can move due to the selected range to the beacon. These different ranges can affect the Pockels cell's ability to precisely control the polarization state across the system pupil, and the light blocking is consequently degraded. How the Pockels cell degrades in its ability to create an effective shutter is analyzed by understanding the polarization state across the telescope's relayed pupil. Subtle changes in the polarization state at points within the sensing system's pupil can result in light leakages that are strong enough to overcome the desired signal from the beacon. This effect is presented through mathematical theory, Zemax analysis specific to the TARDIS, and laboratory-based measurements using the Pockels cell shutter system from the TARDIS.

The blocking power of the Pockels cell engineering challenge arises from changing the range to the beacon source. Traditional beacon-based systems that do not intentionally change the range to the beacon, but still employ a Pockels-cell-based shutter do not have this problem because the optical component layout can be optimized for one specific range. Also, systems without a Pockels-cell-based shutter do not have this issue. [31] However, producing uniquely configured dynamically ranged beacon-based profiles without a Pockels-cell-based shutter would become more challenging due to the relatively fast timing requirements. Other solutions have been explored

as well. It has been proposed that Rayleigh beacons that are used as part of a constellation based scheme for MCAO can be effectively used in conjunction with a dynamic refocus sensing system. The refocusing system is used so that the return from each laser pulse can be sensed at a pre-calculated range dependent sharp focal point. This technique will allow for increasing the brightness of the returned light to an optimal level and will potentially allow for higher altitude beacons than previously possible with traditional range gating techniques. [21, 28] This technique can provide enhancements to a dynamically ranged Rayleigh beacon system; however, it adds to the complexity of the system, requires mechanically moving parts, and is not absolutely required for performing dynamic-range gating. Alternatively, a novel sensing methodology has been proposed by Lloyd-Hart [36] that suggests using the image-plane intensity distributions to extract pupil-plane phases. This methodology exploits the instantaneous Point-Spread Function (PSF) of the atmosphere and telescope optics in the down going path from the beacon. Phase recovered in this methodology from the extra-focal images is a good measure of the pupil-plane distortions of the return path light from the beacon. This methodology was shown as feasible through simulation; however, it was mentioned that it would be reliant on a fast optical shutter such as that created by a Pockels cell. Consequently, since beacons from multiple ranges are required for this methodology to function, a similar issue will likely be discovered in practice. The main body of this paper will discuss the Pockels cell's ability to function as an optical shutter in the presence of a dynamically ranged Rayleigh beacon.

A dynamically ranged Rayleigh beacon system presents an engineering challenge of a shifting focus within the system. Particularly, this shifting focus can cause light leakages in a Pockels cell based optical shutter. This leakage arises from the ability of the Pockels cell to rotate the polarization field uniformly across the entire cross-section of the relayed light between two crossed polarizers within the system. The Pockels cell’s ability to function as an optical shutter is addressed

in the remainder of the paper by analyzing the polarizing pupil in the system at key points along the optical path through simulation. These effects are further explored through experimentation with results demonstrating the Pockels cell blocking contrasts for multiple beacon ranges. From this, a recommendation is presented that will allow for mitigating changing focus effects on the Pockels cell's ability to function as a fast optical shutter. The analysis presented along with the recommendations provided a path forward for effectively using Pockels cells as fast optical shutters in the presence of a shifting focus within the sensing system. This allows for dynamically ranged Rayleigh beacon systems to produce higher resolution tomographic estimates of the turbulence strength along the viewing path produced from high speed measurements not limited by physically moving parts.

## 7.1 TARDIS System

The TARDIS is an optical sensing system that is based on dynamically changing the range between the collecting sensor and Rayleigh beacon during a static period of relatively unchanging turbulence-induced wavefront perturbations. A notional collecting scenario is shown in Fig. 57, where the idealized circular "beacons" are the air molecule and aerosol particle backscatter images captured at different distances from the collecting aperture based on laser pulsing and camera shutter speed. The TARDIS system utilizes an on-axis collimated outgoing pulsed laser beam where range to the beacon is controlled through an electronically driven fast optical shutter. It is shown that there are overlapping and non-overlapping atmospheric turbulence regions that affect the wavefront perturbations seen in each of the backscatter beacon images. These are used as part of an algorithm to deduce a discretized version of the refractive index structure parameter that is segmented based on the choice of beacon locations. [52] The TARDIS is comprised of a beam projection system, collecting telescope, and a sensor system. Within the sensor system, there is a beam relay and conditioning system that collimates and controls the size of the sensed light, a

Pockels cell that acts as a fast shutter, and Shack-Hartmann wavefront sensor that is comprised of a lenslet array and camera. These systems function in unison to control the light from the Rayleigh beacon so that the camera senses light from the desired ranges. [54]

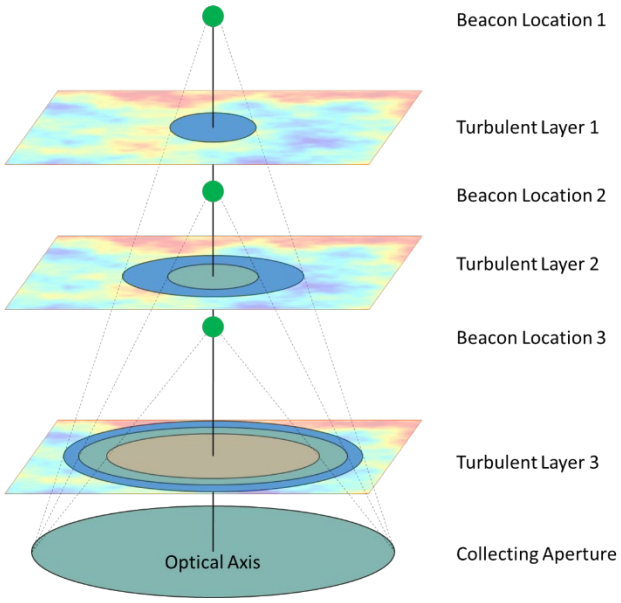


Fig. 57. Notional dynamic beacon collection scenario displaying a three beacon collecting scenario where the beacon is placed at different ranges along the sensing system's optical axis.

Key components of the sensing system are shown in the layout diagrams in Figure 58. The flip mirror is aligned to the optical axis and folds light traveling through the telescope's central annulus. M1 through M5 are flat, turning mirrors used for folding the light within the confined space. An iris is used to block unwanted light. Ln is a negative lens that conditions the beam to an appropriate size. L1 and L2 are relay lenses that collimate and refocus the beam for relay through the polarizers, P1 and P2, and the Pockels cell, PC. L3 collimates the beam at a reduced size for input into the Shack-Hartmann wavefront sensor (SHWFS). Alternatively, for Signal-to-Noise Ratio (SNR) investigations and increased sensitivity, the SHWFS can be replaced by a focusing lens and photodetector, labeled L4 and PD.

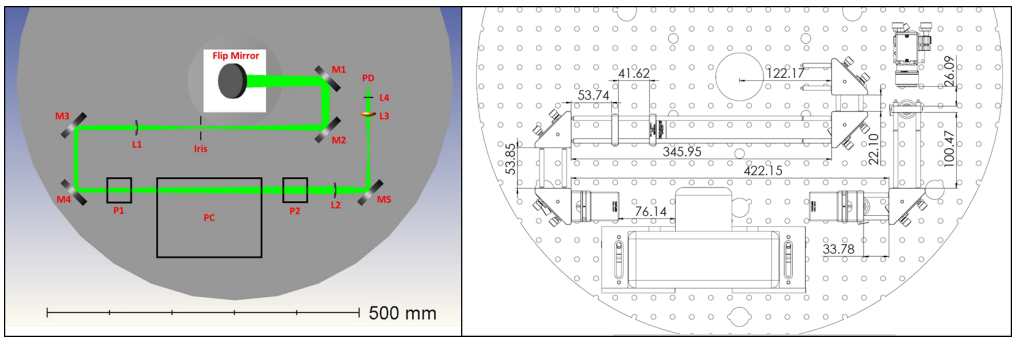


Fig. 58. (left) Sensing system light path and (right) physical layout of the TARDIS sensing system

The Pockels cell used as a fast optical shutter is a crucial component that enables dynamic ranging of the Rayleigh beacon source. The Pockels cell can be configured and controlled electronically using predefined configurations utilizing inputs from a function generator in conjunction with the manufacturer's provided control software. [15] For the Pockels cell to function properly, the precise timing needs to be understood and the light-blocking contrast needs to be high for rejecting light from undesired ranges from the sensing system. The ability of the Pockels cell to function as a shutter is dominated by the uniformity of the electric field within the crystal, light leakages caused by unwanted birefringence within the crystal, quality of the polarizers used, the accuracy of the orientation of the polarizers used, and the divergence of the incident beam traveling through the Pockels cell. [42] For the TARDIS, the uniformity of the electric field was controlled well, resulting in a minimal effect. Birefringence within the Pockels cell crystal was unnoticeable. The quality and orientation accuracy of the polarizers was measured and controlled precisely. These qualities had minimal negative effects on the Pockels cell system's ability to function as an optical shutter. However, the divergence of the incident beam did play an important role, and consequently, the resultant light leakage effects had to be measured and mitigated. Ideally, the light should pass parallel to the crystal's optic axis for uniform field rotation to occur. Beams that have a finite

divergence will not be uniformly retarded and light leakages will occur. [42] This effect can be understood further by analyzing the polarization pupil within the Pockels cell system for a range of possible divergence angles. A notional graphic of this effect is shown in Figure 59. This analysis was done in Zemax. [65] Additionally, for the TARDIS, the ability to block light was measured from an experimental setup that simulated propagated light from a range of beacon distances. This was done by using a lens system to emulate the telescope collection optics and a re-imaging lens to shift the focal point to emulate the dynamic-range beacon. The TARDIS sensing system was set up along the optical axis of this lens system such that the same effects could be measured in the laboratory as in the operational collection system. Results from both the mapping of the polarization pupil vs. divergence angle and the systems measured ability to block light from a range of beacon distances are presented in subsequent sections in this paper.

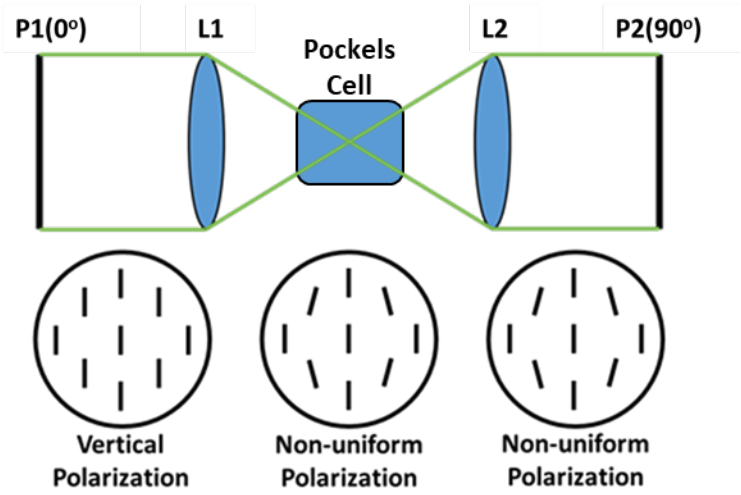


Fig. 59. Notional effect of converging or diverging beams on the polarization pupil

The SHWFS is used to measure the resultant phase of the incoming wavefront by zonal tilt, also known as slope measurements. [28] For the SHWFS to function for this use, the incoming light is required to have temporal brevity such that a single focused spot is produced by the lenslet array of the SHWFS. This temporal brevity is controlled by the Pockels cell shutter system. If the shutter system is unable to block light from outside the desired time window effectively, light leakages

will result in all pixels on the detector to become overtaken by unwanted light, effectively making SHWFS spot measurements impossible. This happens because the system is based on Rayleigh beacon technology, where the laser beacon energy is produced at the sensing system and is propagated along the optical axis of the system. Laser energy scattered from closer ranges to the sensing system will be stronger in intensity. One model that describes this is the LIDAR equation. The LIDAR equation can be expressed symbolically as

$$N(z) = \left(\frac{E\lambda}{hc}\right)(\sigma_B n(z)\Delta z)\left(\frac{A_R}{4\pi z^2}\right)(T_o T_A^2 \eta) + N_B \tag{88}$$

where $N(z)$ is the expected number of photons detected, $E$ is the laser pulse energy, $\lambda$ is the optical wavelength, $h$ is Plank's constant, $c$ is the velocity of light, $\sigma_B$ effective backscatter cross-section, $n(z)$ number density of scattering particulates at range $z$, $\Delta z$ is the receiver range gate length, $A_R$ is the area of the receiving aperture, $T_o$ is the transmission of the optical components, $T_A$ is the one-way transmission of the atmosphere between the telescope and the beacon, $\eta$ is the quantum efficiency of the detector, and $N_B$ is the number of background and noise electrons. The Rayleigh backscatter cross-section and atmospheric density product is given by

$$\sigma_B n(z) = 3.6 \times 10^{-31} \frac{P(z)}{T(z)} \lambda^{-4.0117} \tag{89}$$

where $P$ is the atmospheric pressure at range $z$ in millibars and $T$ is the atmospheric temperature at range in Kelvin. [31] Modeled values using the TARDIS system parameters are shown in Table 4. Transmission through the system was measured to be 27.24%, and the atmospheric transmission was modeled as 78%. The detector quantum efficiency was taken from the camera data sheet and modeled as 64%. A 12 by 12 sub-aperture array is used for this example case. It is important to recognize that the TARDIS system is a proof of concept system and that the photon count could be increased by utilizing a stronger laser source, which are commercially available but weren't used

due to cost, choosing a shorter wavelength, increasing the collecting aperture size, or increasing the receiver range gate length.

## 7.2 Focal Shifts Due to Dynamically Ranged Beacon Locations

In order to take Rayleigh-beacon-based measurements and produce a tomographic estimation of the turbulence strength, the TARDIS is reliant on changing the range to the sensed beacon. This is done through an electronically configured shutter system that controls the timing of the light-blocking mechanisms while laser light propagates into the atmosphere along the optical axis of the sensing system. [54] Changing the range to the sensed beacon induces a focal shift in the sensing system that needs to be understood for effective measurements to be taken. The optical beam relay was modeled in Zemax for the expected range of configurations. [65] Examples of some of the key configurations are shown in Figures 60, 61, and 62. A plot of the focal shift induced by the different ranges of beacon sources is presented in Figure 63. The area to focus on in Figures 60, 61, and 62 is between the two polarizers where the Pockels cell resides, also depicted in Figure 58. For a Pockels cell to function properly as an optical shutter, the light passing through the Pockels cell's aperture must be collimated or close to collimated. [42] For the TARDIS configuration set for beacon ranges from approximately 1.5 km to an infinite range, light rays passing through the Pockels cell are close to collimated. An infinite range and 5 km range is shown in Figures 60 and 61. In both cases, the light is near collimated, with light rays only having minimal divergence. However, Figure 62 highlights the 1 km range to the beacon which does significant focusing and diverging light rays within the Pockels cell. This divergence will consequently cause a non-uniform polarization state in the polarization pupil as described in the *Mathematical Interpretation* section and similarly highlighted by the polarization pupil image in Figure 65. For the TARDIS, this will manifest as light leakages that do not effectively become shuttered for the close to the sensing system ranges, and will consequently have to be blocked by other means.

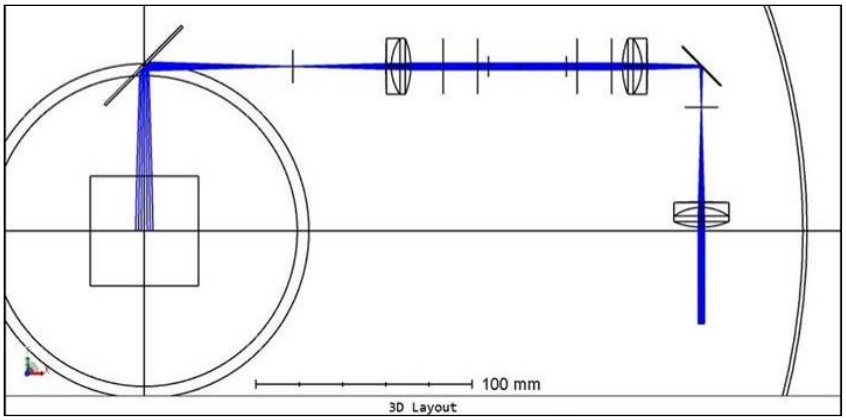


Fig. 60. Zemax ray analysis for the sensing system with light originating from an infinite range

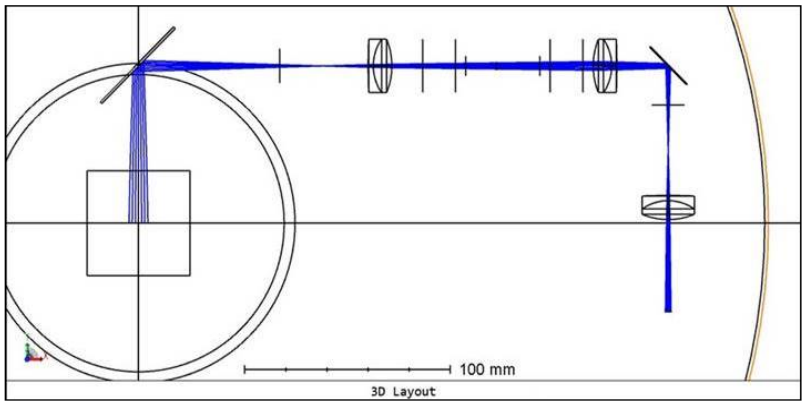


Fig. 61. Zemax ray analysis for the sensing system with light originating from a 5 km range

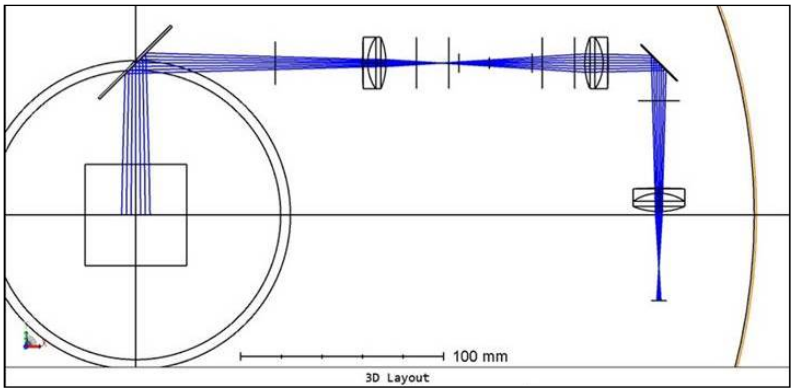


Fig. 62. Zemax ray analysis for the sensing system with light originating from a 1 km range

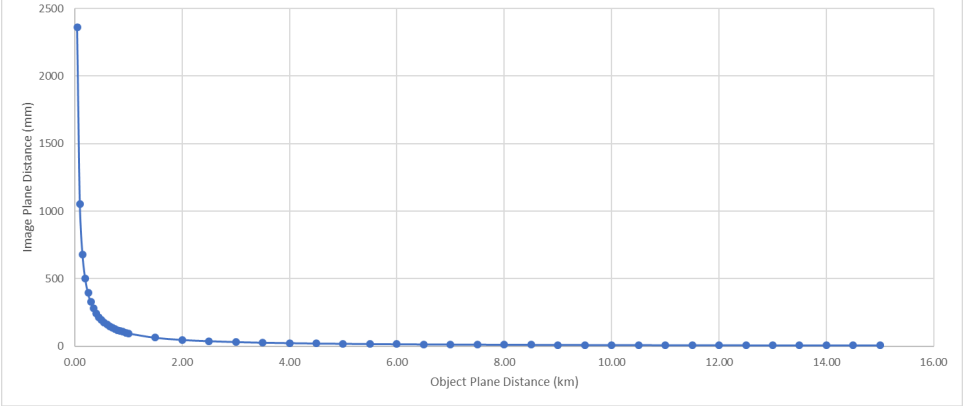


Fig. 63. Plot of the change in image plane location for beacons originating from varied distances showing significant movement at 1.5 km and below

## 7.3 Polarization Pupil Analysis

*7.3.1 Mathematical Interpretation*

The wavefront curvature through the Pockels cell must be minimized in order for the Pockels cell to perform well as an optical shutter, implying that the beam passing through the crystal must have minimal angular divergence or beam focus. Light beams that have a finite divergence or focus will not be uniformly retarded by the Pockels cell. Consequently, the operation of the Pockels cell as an optical shutter will degrade due to light leakages. These light leakages can be strong enough to overcome the signal from the returned Rayleigh beacon. [42]

The polarization pupil within the Pockels cell can be analyzed using Jones calculus following the methodologies presented by Ruoff [29] or Chipman [39]. A convenient way to describe a polarized field is by its Jones vector, **J**, which is comprised of the transverse electric field components $E_1$ and $E_2$,

$$\mathbf{J} = \begin{pmatrix} E_x \\ E_y \end{pmatrix} = \begin{pmatrix} A_x e^{i\delta_x} \\ A_y e^{i\delta_y} \end{pmatrix} = A e^{i\delta_x} \begin{pmatrix} cos\theta \\ sin\theta e^{i\delta} \end{pmatrix}, \tag{90}$$

where $A_i$ are amplitudes and $\delta_i$ are the phases, respectively. Pulling out the overall amplitude and arbitrary phase factor the Jones vector is written in the last form with $A_x = Acos\theta$, $A_y = Asin\theta$, and $\delta = \delta_y - \delta_x$. If $\delta = 0$, the light is linearly polarized with angle $\theta$ describing the orientation of the vibrational plane of the electric field. If $\delta \neq 0$, the polarization state is elliptical. [29] This is important for the Pockels cell to rotate the polarized field uniformly; the field needs to have uniform linear polarization across the whole pupil within the Pockels cell.

Converging or diverging light in a system can be viewed as coming from a lens. Analysis of the polarization pupil of this optical element can be thought of as a product of two well understood optical elements: a linear retarder and a linear partial polarizer. These are used in their rotated forms as

$$\mathrm{J_{pol}}(d, \psi_p) = \begin{pmatrix} 1 + dcos2\psi_p & dsin2\psi_p \\ dsin2\psi_p & 1 - dcos2\psi_p \end{pmatrix} \tag{91}$$

$$\mathrm{J_{ret}}(\phi, \psi_r) = \begin{pmatrix} cos\phi - isin\phi cos2\psi_r & -isin\phi sin2\psi_r \\ -isin\phi sin2\psi_r & cos\phi + isin\phi cos2\psi_r \end{pmatrix} \tag{92}$$

where the orientation angles are $\psi_p$ and $\psi_r$. The polarizer is characterized by the mean amplitude, t, and the relative amplitude difference, *2d*. The retarder is characterized by the global phase factor, $\Phi$, and the global phase retardation, $2\phi$, with the fast axis corresponding to $(J_{ret})_{11}$. The Jones matrix for a lens is consequently represented as

$$\mathrm{J} = te^{i\Phi}\mathrm{J_{pol}}(d, \psi_p)\mathrm{J_{ret}}(\phi, \psi_r). \tag{93}$$

For the optical system, the Jones matrix is also a function of the pupil coordinates, commonly referred to as the Jones pupil or polarization pupil. [29] Using the described decomposition treatment for a lens, the Jones pupil within the Pockels cell can consequently be analyzed for the

changing focal point effects that result from the operation of a dynamically ranged Rayleigh beacon.

The desired Jones pupil state within the Pockels cell is that of uniform linear polarization. At P1 in Figure 58, the polarization is converted to a uniform linear polarization field. However, depending on the range to the Rayleigh beacon, the telescope's focal point in the sensing system will shift and consequently create converging or diverging light rays between the two polarizers, P1 and P2. Consequently, this affects the Pockels cell's function of uniformly rotating the full pupil of light and results in possible light leakages. These light leakages could be strong enough to raise the background noise levels to a point where the desired signal on the SHWFS is no longer detectable. To understand the effect of converging or diverging light rays, let us individually look at how a set of possible orientation angles affect the terms in Equation 93 when applied to linearly polarized light. The partial polarizer and retarder are then governed by

$$\mathrm{J_{pol}}(d,\psi_p)\begin{pmatrix}1\\0\end{pmatrix}=\begin{pmatrix}1+dcos2\psi_p\\ dsin2\psi_p\end{pmatrix} \tag{94}$$

$$\mathrm{J_{ret}}(\phi,\psi_p)\begin{pmatrix}1\\0\end{pmatrix}=\begin{pmatrix}cos\phi-isin\phi cos2\psi_r\\ -isin\phi sin2\psi_r\end{pmatrix}. \tag{95}$$

Analyzing orientation angles between 0 and 90 degrees, the polarization direction in the partial polarizer can result in a rotation. For the retarded, the polarization state can become elliptical. To summarize, when the incoming light is not parallel to the fast or slow axis for the partial polarizer or the bright or dark axis for the retarder, the polarization state of the light will become rotated or take on an elliptical form. [29] This outcome will further be shown through Zemax based analysis focusing on these two observed effects in the polarization pupil.

*7.3.2 Ray Tracing Polarization Pupil Analysis*

The OpticStudio software produced by Zemax [65] was utilized to demonstrate how the polarization state can change across a pupil when light rays become converging or diverging. This analysis was designed to investigate a set of possibilities that would be analogous to convergent or divergent rays experienced by the TARDIS system due to the focal point shifting in the sensing system as a result of changing the range of the beacon. The analysis was set up for a wavelength of 527 nm with a uniform vertical polarization set to the entire entrance pupil. The polarization pupil function within the OpticStudio software was utilized to evaluate how the polarization changes at the exit pupil of the system. An ensemble of simulations was set up to investigate convergent and divergent rays for a series of f-number lens setups. Changing the f-number had the effect of showing the enhanced effect on peripheral rays, showing the susceptibility to deviation from linear polarization. Figure 64 shows the default state for a system that is perfectly collimated, where all rays have vertical polarization. Figure 65 shows an example case of how rays towards the edge of the system's pupil stray from linear polarization and become tilted and elliptical.

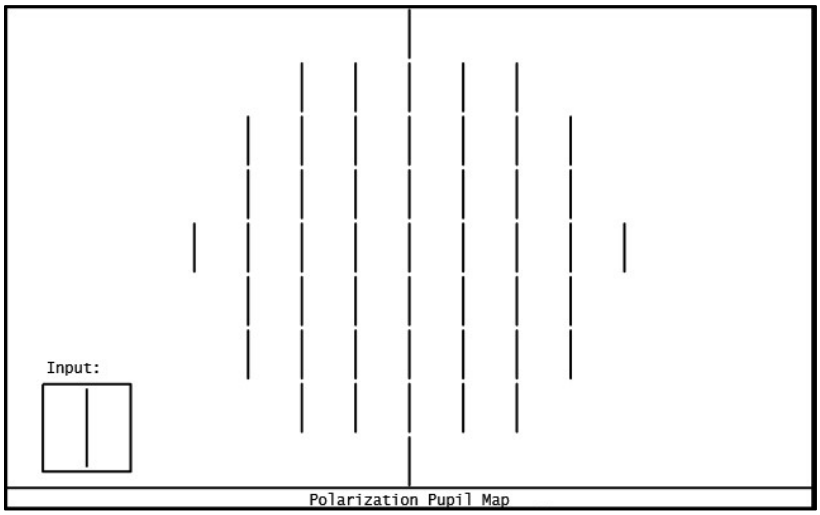


Fig. 64. Zemax polarization pupil map for a collimated beam subjected to vertical polarization input

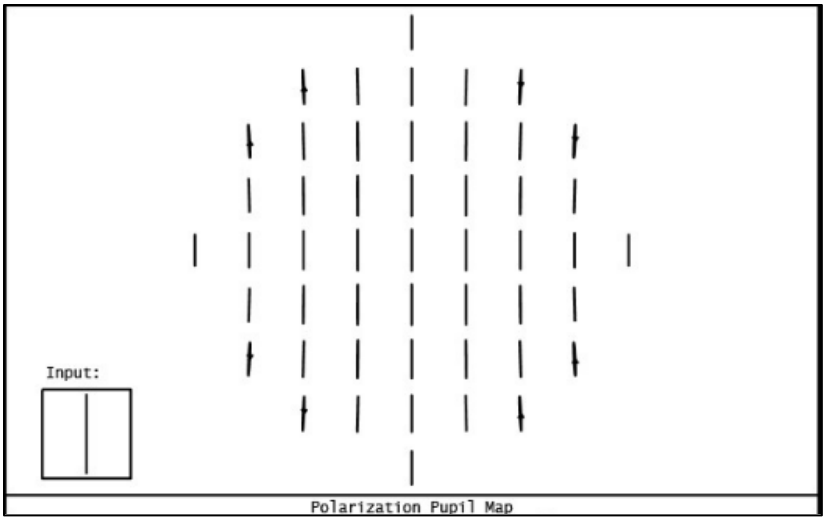


Fig. 65. Zemax polarization pupil map for a convergent beam subjected to vertical polarization input

Within the OpticStudio software, multiple data fields can be used to quantify the polarization change from the input to the exit pupil of the system. The polarization data fields of $E_x$ and $E_y$ were used for this analysis. For vertical polarization, $E_x$ will equal 0 and $E_y$ will equal 1. Any deviation from these values will indicate that part of the pupil no longer has pure vertical polarization and has become tilted with a small degree of elliptical polarization. Since convergent and divergent rays across the system's pupil do not change in polarization uniformly, the metrics of average and standard deviation of the vertical polarization values were used. Figures 66 and 67 shows the change of these value vs. f-number of the system. The mean difference and standard deviation from the linear polarization state were calculated from the ensemble of discrete points for each f-number system. Examples of the discrete points sampled are shown in Figures 64 and 65. This data presents a trend; the higher effective f-number systems deviate less from the input state of uniform vertical polarization across the system's pupil.

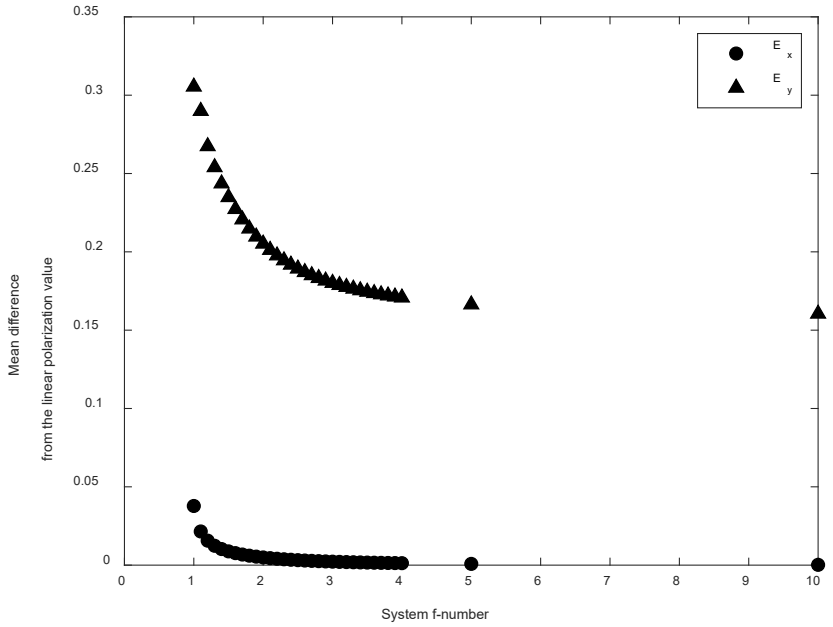


Fig. 66. Mean difference of $E_x$ and $E_y$ from the linear polarization value for system f-numbers from 1 to 10

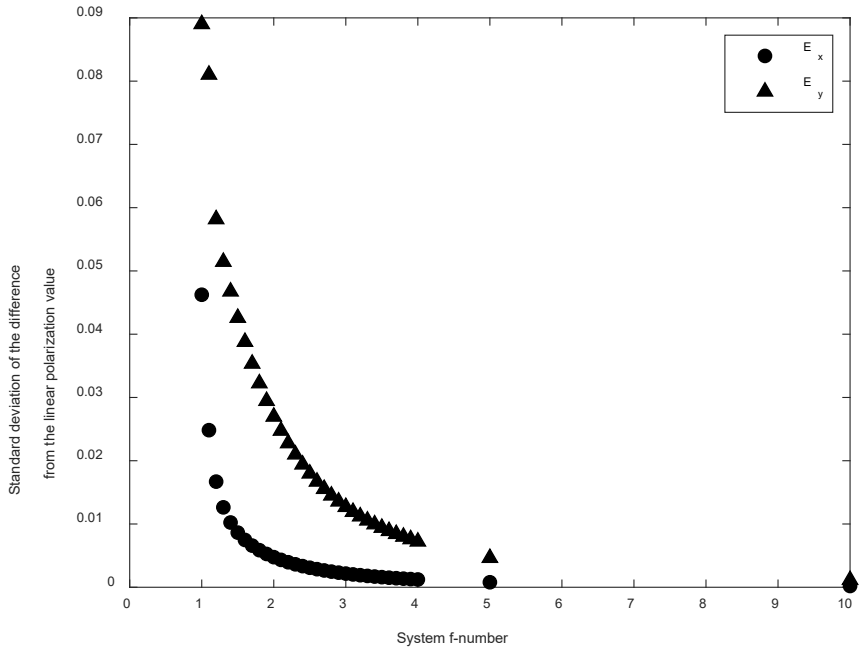


Fig. 67. Standard deviation of $E_x$ and $E_y$ from the difference from the linear polarization value for system f-numbers from 1 to 10

## 7.4 Sensing System Laboratory Measurements

Laboratory measurements were taken looking at the light throughput to analyze the ability of the Pockels cell to function as an optical shutter in the presence of focal point shifts in the sensing system. A light relay system was set up to mimic the input to the sensing system in Figure 58. Input laser lights were injected into this system with a re-imaging system such that the focal shifts of incoming light due to changing the range to the beacon could be emulated. Emulated ranges under test were 1000 m, 1200 m, 1500 m, and near-infinite. A near-infinite range was used as it is in the part of the curve in Figure 63, where a minimal change in the system's focal point is exhibited.

Data was collected using this setup with the Pockels cell in the shuttered mode for these emulated ranges by recording the power measured by a photodiode and calculating the voltage by

$$V = \frac{P \times R}{R_S} \tag{96}$$

where $P$ is the power measured in watts, $R$ is the selected resistance in ohms on the device, and $R_s$ is the responsivity of the photodiode in watts per ampere. Multiple measurements were taken for each range setting, and each measurement was averaged for a long enough period on the device to reach a stable state. The results are shown in Figure 68. The Pockels cell was chosen to be in the shuttered mode to achieve a measurement representative of the blocking ability. The idea behind this was that when the light is near collimated like that for an infinite range setup, the light-blocking ability should be high and would yield a small value on the photodiode. Conversely, the blocking ability would be lessened when light rays are converging within the Pockels cell. This hypothesized trend is shown in Figure 69. The error bars are two standard deviations from the mean of the measured data. A non-zero value is present for a near-infinite source setup. This is likely due to

the high-intensity light source used in the laboratory and small imperfections and orientation errors in the Pockels cell and the polarizers.

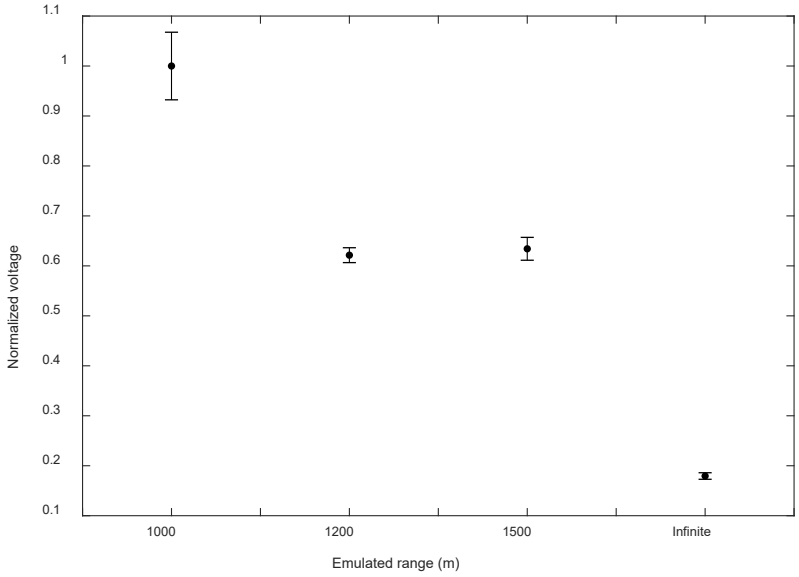


Fig. 68. Plot showing the results from laboratory measurements of the throughput of the sensing system for emulated ranges of 1000 m, 1200 m, 1500 m, and near-infinite.

## 7.5 Discussion

Our laboratory setup allowed for measuring the optical throughput of a 527 nm laser through the sensing system with a re-imaging system input to simulate the beam focusing conditions of the dynamically ranged Rayleigh beacon of the TARDIS. This experiment measured the light-blocking ability of the sensing system based on changing the convergence or divergence of the light rays as they traveled through the Pockels cell. Alterations for a laboratory-based setup were made as compared to an on-sky TARDIS device. These included increasing the laser power injected to enable easily quantifiable and distinguishable measurements, and the use of a photodiode in place of the Shack-Hartmann wavefront sensor. These two laboratory accommodations are not believed

to influence the resulting trends. It was observed that shorter emulated ranges exhibited larger measurement values, indicating that less light was able to be blocked by the Pockels cell shutter system.

Since the Pockels cell shutter system relies on manipulating the state of polarization between two linear polarizers, it was theorized that the state of the polarization pupil between the two linear polarizers within the Pockels cell aperture was not uniform. The Zemax modeling of the system supports this. As the focal point shifts towards the Pockels cell, the light rays become less collimated as they pass through the Pockels cell. Particularly the light rays that are furthest from the optical axis are most effected and exhibited a change of state from vertical linear polarization to tilted elliptical polarization. This elliptization was quantified through the Zemax models by extracting the change in the $E_x$ and $E_y$ terms for each data point within the polarization pupil. From this, a trend could be gleaned. As the focusing power increased, the change in the polarization terms away from the optical axis had a greater magnitude change. This focusing power is analogous to the sensing system beacon ranges that are close to the collection aperture for the TARDIS. Consequently for these scenarios, the light will not be effectively blocked by the Pockels cell based shutter system.

Without alternative mitigation techniques, the beacon ranges of which a dynamically refocused Rayleigh guide star based turbulence profiling system is functional will be limited. The farthest beacons will be limited by the SNR limitations of the system, and the near beacons will be limited by light leakages produced from the polarization-based optical shutter not being able to maintain a uniform polarization state across the pupil. Unwanted light from outside the beacon range can be blocked by the use of special filters and lower speed physical or electronic shutters. Then the Pockels cell shutter only has to block light from a sub-range closer to the intended beacon range.

Specific to the TARDIS, ranges that are below approximately 1500 m start to exhibit light leakages, so dynamic ranging will be difficult, and the signal will have to overcome a more substantial source noise.

There are alternative mitigation techniques and system design choices that can help lessen the negative effect of light leakages stemming from non-uniformity in the polarization pupil. Suggested by Georges et al., a dynamic refocus system can alter the angle of the light rays and maintain collimation between crossed polarizers within a Pockels cell based fast optical shutter. This system eliminates the light leakage issues and also effectively extends the useful range of possibilities for utilizing Rayleigh beacons. [21] However, this comes at the cost of added complexity and moving parts within the sensing system. There are also simpler measures that can be taken to lessen the effective light leakages due to non-uniformity in the polarization pupil. One such method would be to utilize longer focal length relay lenses that are oversized and designed to handle Rayleigh beacons from both near and far ranges. This does not eliminate the problem, but it can lessen its effect. If employing this mitigation concept, the close ranges will likely result in a beam that is relayed through the system with a large effective beam radius. Many clear apertures of Pockels cells are quite small by design so that the high voltage induced polarization rotation can be enacted across the whole beam. The sensing system's beam reduction optics must be balanced to accommodate for close Rayleigh beacon ranges and the size of the mapped lenslets, which must be smaller than the effective Fried parameter, $r_o$, of the environment being sensed. These criteria can be utilized to produce an accurate $r_o$ estimate. [52]

## 7.6 Conclusion

Induced focal shifts in the TARDIS sensing system between subsequent neighboring beacons due to the process of changing the range to the Rayleigh beacon caused potential degradation from linear polarization of the polarized pupil present within the Pockels-cell-based optical shutter. This degradation from linear polarization manifests itself as a slightly rotated elliptical polarization state and was characterized by Jones calculus applied at each discrete point within the pupil. The amount of change was calculated using Zemax-based software specific to varied converging ray angles representative of what the TARDIS system could experience, especially at very low altitude beacon range choices. The trends found through the Zemax-based analysis was verified through an experimental setup that simulated beacon ranges where the polarization state change would be detrimental to the Pockels-cell-based optical shutter to adequately block light. The light leakages through the optical shutter under low altitude beacon ranges proved to be large enough that they could overwhelm a Shack-Hartmann wavefront sensor measurement by increasing the background signal. Based on understanding gained through the analysis in this paper, strategies have been developed to minimize the unwanted effects leading to light leakages. Easiest, a configuration choice during data collection operations of keeping the lowest beacon above 1500 m will mitigate the light leakage effects. However, interesting turbulence strength changes can happen slightly below 1500 m, specifically around the boundary layer where a turbulence strength inversion typically occurs. As a recommendation, a minor design change of extending the focal length of the lenses in the relay system and effectively stretching the light relay to lessen the converging ray angles within the Pockels-cell-based optical shutter could be implemented that would also mitigate the cause of the light leakages and lower the effective beacon range where data could be collected. This would have a small negative effect specific to the TARDIS as space on the optical breadboard is limited and this strategy would physically take up more space. Lastly, methods suggested by researchers at the University of Arizona of utilizing a dynamic refocusing system would correct for

all identified causes of light leakages due to focal shifts in the system. This strategy does add significant complexity to the system and also would take up too much space on the TARDIS breadboard. However, for future TARDIS-like sensors that are not limited by breadboard space a dynamic refocusing element that could operate at the same speed as the range changes employed by dynamically ranging the Rayleigh beacon would be ideal.

# VIII. Data Collection and Results

## 8.0 Introduction

This section is based on an anticipated peer reviewed SPIE Applied Optics journal article and two soon to be published conference papers. The first conference paper describes the current TARDIS system used for profiling turbulence strength and is part of an invited talk at the OSA Propagation Through and Characterization of Atmospheric and Oceanic Phenomena conference. This paper will be published in late July 2021. The second conference paper describes the preliminary results from the first data collections, and is going to be presented at the SPIE Unconventional Imaging and Adaptive Optics 2021 conference that is part of SPIE Optics and Photonics West. This paper will be published in August 2021.

The effect of turbulence on a long range imaging system manifest as an image blur effect usually quantified by the phase distortions present in a system. The blurring effect is conceivably understood on the basis of the measured strength of atmospheric optical turbulence along the propagation path and its impacts on phase perturbation statistics within the imaging system. One method that has been proposed for obtaining these measurements is by use of a dynamically ranged Rayleigh beacon system that exploits strategically varied beacon ranges along the propagation path, effectively deducing estimates of specific path segment contribution of the blurring aberrations affecting an optical imaging system. A system utilizing this technique has been designed, and a prototype has been constructed for testing at John Bryan Observatory, Yellow Springs, OH. This system is called TARDIS, which stands for Turbulence and Aerosol Research Dynamic Interrogation System. This section will describe the TARDIS system, make reference to tomographic turbulence estimation methodology of previous sections, and provide analysis of first data collected by TARDIS.

### *8.0.1 Motivation*

Estimating or measuring atmospheric turbulence to correct for aberrations in an image has been of interest to the scientific community for a long time. Traditionally, a wavefront sensor is used to gather measurement based estimates of the image correction needed to compensate for the total integrated volume atmospheric turbulence induced blur. Historically, this has been sufficient for adequate image correction. However, there has been a growing desire within the scientific community for longer imaging ranges, wider fields of view, and larger telescopes to enable increased sensitivity. These three main desires pronounce the effects of atmospheric turbulence on an image, and path-integrated correction techniques fail to provide adequate image correction. [46] Born out of a need, path-resolved turbulence profiling techniques were conceived, modeled, tested, and integrated into adaptive optics assisted imaging programs. [30, 3, 5] Two well accepted techniques to produce path-resolved atmospheric turbulence strength estimates, among others, are scintillation detection and ranging (SCIDAR) and slope detection and ranging (SLODAR). [40, 56] These methods inform systems of the locations where turbulence is likely strong, and this knowledge aids to some extent in driving adaptive optics systems.

When scintillation and anisoplanatism become dominant effects, such as in strong turbulence, adaptive optics compensation becomes notably challenging and the resulting correction applied to an image is inadequate. Consequently, new approaches were developed. Tyler [17] summarizes leading techniques and provides quantification of how well they perform. Of the leading techniques presented, multiconjugate adaptive optics (MCAO) technology holds promise. In theory, MCAO systems could reduce or possibly even eliminate aberrations induced on an image from turbulent layers along the viewing path. MCAO was first introduced by Beckers in (1989) [19] to overcome field of view limitations. Shortly after that, Tallon and Foy in (1990) [37] introduced the concept

of tomography to the problem set of atmospheric turbulence. The concept was to utilize multiple reference sources in a way that allows for resolving turbulence strength with altitude from a series of independent measurements. [43] Utilizing MCAO concepts, three-dimensional turbulence representations of an environment can be constructed which allows for correction concepts along any line of sight within the field of regard constrained by the volume enclosed by the reference sources used. [8] MCAO concepts in conjunction with laser guide star systems have been accepted as common practice and have been incorporated into a number of observatories where large aperture telescopes exist. [34] Even with these substantial advances in atmospheric tomography where the desire is to compensate in real time for the rapidly changing distortions, new research has introduced computational burdens for adapting to very strong distributed turbulence and large telescope extended field-of-view requirements. [44] Building upon these concepts and advances in measurement technologies, a dynamically ranged Rayleigh beacon system concept was formulated with the goal to produce profiled strength estimates of turbulence along the optical path with a significantly lessened computational burden. Additionally, the need to get away from natural guide star constraints has led to utilizing laser guide star technology in new ways that enable highly adaptable beacon placements along the viewing path that are programmable on an individual laser pulse basis. [54, 51, 52, 53, 55]

### *8.0.2 Background*

There is a need to understand the image degradation effects of optical turbulence on long range imaging systems. One method is to quantify the phase distortions and associated statistical properties introduced by the atmosphere along the viewing path. One system that has been proposed for obtaining measurements to quantify the phase distortions and estimate the associated statistics is by use of a dynamically ranged Rayleigh beacon system that exploits strategically varied beacon ranges along the propagation path, effectively deducing measurement based

estimates of specific path segment contributions of the phase distortions affecting the optical imaging system. [52] A system utilizing this technique has been designed, and a prototype has been constructed for testing at John Bryan Observatory, Yellow Springs, OH. [51] This system is called TARDIS, which stands for Turbulence and Aerosol Research Dynamic Interrogation System. TARDIS was designed around a pulsed laser beacon and electronically controlled fast optical shutter that were both aligned to the optical axis of a telescope. [54] Utilizing this system a novel algorithm was theorized [52] and analyzed such that the TARDIS system could be optimized for obtaining accurate estimates of path resolved turbulence strength estimates. [53] The remainder of this chapter will summarize the TARDIS system, present the tomographic turbulence estimation methodology, and analyze the first data collected at John Bryan Observatory.

## 8.1 TARDIS Design Methodology

### *8.1.1 TARDIS System Description*

The TARDIS is an optical sensing system that is based on dynamically changing the range between the collecting sensor and Rayleigh beacon during a static period of relatively unchanging turbulence-induced wavefront perturbations. A notional collecting scenario is shown in Figure 69, where the idealized circular "beacons" are the air molecule and aerosol particle backscatter images captured at different distances from the collecting aperture based on laser pulsing and camera shutter speeds. The TARDIS is comprised of a beam projection system (BPS), collecting telescope, and a sensor system. The BPS utilizes an on-axis collimated outgoing pulsed laser beam. The collecting telescope is a 61cm, F17 Ritchie-Chretien telescope that has 207x pupil relay magnification. The sensor system's main components are a pupil relay system, polarization control system, Pockels cell based fast optical shutter, and a Shack-Hartmann wavefront sensor. Data is captured on a Shack-Hartmann wavefront sensor from backscattered laser light and used in a novel algorithm to deduce turbulence strength profiles. [52] The key components of the sensing system

and their configuration to optimize the total system's functionality have been previously described. [55] Modeled values using the TARDIS system parameters are shown in Table 04.

Table 04. Input parameters and resultant photon counts for example beacon

| Parameter | Value |
|---|---|
| Pulse Energy (mJ) | 8 |
| Wavelength (nm) | 527 |
| Atmospheric Pressure (mbar) 1 km, 2 km, 5 km, 10 km | 898.75, 794.95, 540.2, 264.36 |
| Atmospheric Temperature (K) 1 km, 2 km, 5 km, 10 km | 281.65, 275.15, 255.65, 223.15 |
| Area of receiving aperture ($m^2$) | 1.17 |
| Range (m) | 1000, 2000, 5000, 10000 |
| Receiver range gate length (m) | 100, 200, 500, 1000 |
| Expected photons at detector aperture | $3.70 \times 10^5$, $1.67 \times 10^5$, $0.49 \times 10^5$, $0.14 \times 10^5$ |
| Expected photons per subaperture | 3302, 1495, 437, 123 |

*8.1.2 TARDIS Data Processing Methodology*

Obtaining measurement based estimates of the turbulence strength profile from TARDIS is based around collating segmented refractive index structure parameter, $C_{n_{seg}}^2$, values traced to specific layers of the atmosphere as shown in Figure 69. These $C_{n_{seg}}^2$ values are developed from Fried parameter segments, $r_{0_i}$, which are deduced from neighboring measurements on the Shack-Hartmann wavefront sensor.

$$C_{n_{seg}}^2 = \frac{{r_{0_i}}^{-5/3}}{0.423k^2\Delta z_i} \tag{97}$$

where $r_{0_i} = r_{0_{j+1}} - r_{0_j}$ with $j+1$ and $j$ representing two measurements of $r_0$ from neighboring beacon ranges, $\Delta z_i$ is the thickness of the turbulence volume, and $k$ is the wavenumber. A single value of the Fried parameter is estimated from the mean variance of the phase present on the sensing system's collecting aperture as

$$r_0 = \frac{0.299D}{\langle\sigma^2\rangle^{3/5}} \tag{98}$$

where this $r_0$ is a representative metric of the turbulence strength within the volume of a single beacon measurement, $D$ is the aperture diameter, and $\langle \sigma^2 \rangle$ is the mean of the variance of the estimated phase across the aperture that is built from the zonal tilt tiles reconstructed from the Shack-Hartmann wavefront sensor measured gradients. [54]

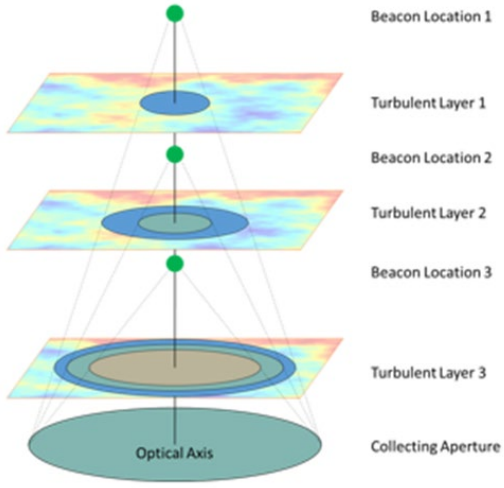


Fig. 69. Notional dynamic beacon collection scenario displaying a three-beacon collecting scenario where the beacon is placed at different ranges along the sensing system's optical axis.

When taking these subsequent measurements of $r_0$ to build up a turbulence strength profile it is important to consider focal anisoplanatism influences as error sources could manifest into the localized turbulence strength estimates. Focal anisoplanatism in TARDIS is a product of beacon placement choices relative to one another and collecting aperture size. In short, it is best practice to keep beacon location choices in close proximity to one another, and build up a full profile from many closely spaced measurements. Full details on focal anisoplanatism influences on dynamically ranged Rayleigh beacon measurements have been presented previously. [53]

## 8.2 Laboratory Measurement Data Collections

Prior to taking on-sky data, a proof of concept laboratory experiment was conducted. This experiment was done using simplified cost-effective equipment and materials. The base setup is shown in Figure 70. The optical source was a hand-held laser pointer operating at 532nm, a 2 lens beam expander, phase screens that were made with glass plates sprayed with hairspray, and a Shack-Hartmann wavefront sensor. A picture of the experimental setup and a zoomed in view of one of the phase screens is shown in Figure 71. The use of hair spray to make a cost-effective phase screen that distorts a wavefront was based off of prior similar experimental work by Thomas. [50]

Data was collected using three phase screens in this experimental setup. First, data was taken with each phase screen in the beam path individually. This served as the truth, measurement for each layer of induced random phase distortion. Then data was taken to mimic the data collection operations of TARDIS. Data was taken with all three screens, then two screens, then just one, and finally no screens. This was intended to replicate, in a simplified sense, the type of data that TARDIS would collect on-sky. Data with no phase screens in the path was used to create a center reference on the Shack-Hartmann wavefront sensor for each lenslet, shown in Figure 72. This was used to calculate slope measurements in the data processing steps. During the experiment, care was taken to place the phase screens in the same repeatable locations as screens were interchanged. However, even with great care taken imperfections in placement are possible which are difficult to quantify using the simple tools available. This is one possible source of error that could influence the resulting data results.

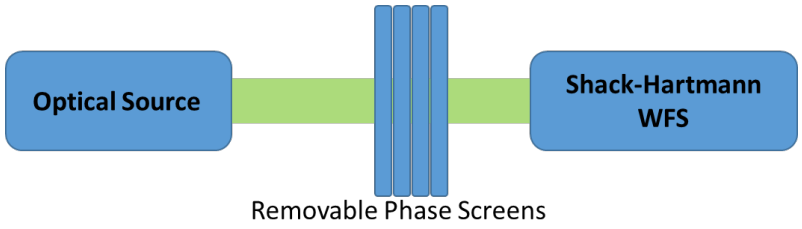


Fig. 70. Depiction of experimental setup for proof of concept lab experiment

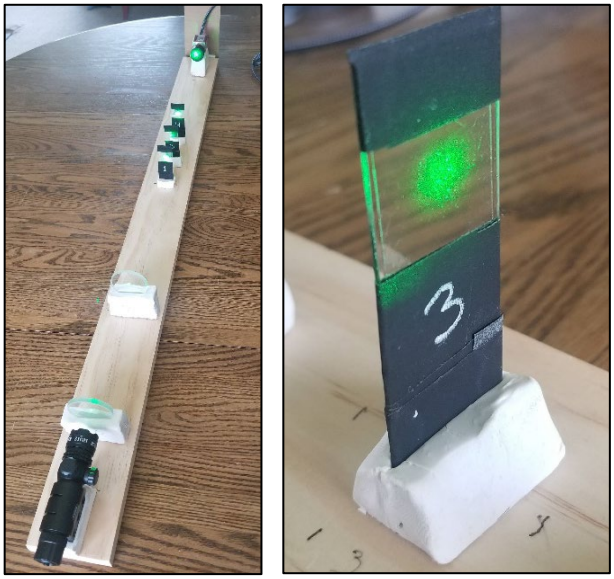


Fig. 71. Photograph of experimental setup for proof of concept lab experiment with zoom in of one of the phase screens used

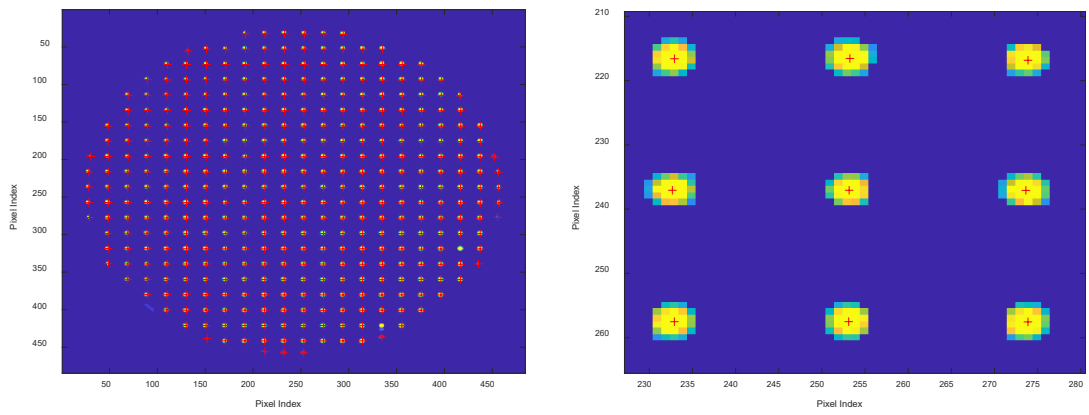


Fig. 72. (left) Reference image from Shack-Hartmann wavefront sensor and (right) zoom in view of the spots

An example of the data collected is shown in Figure 73. Notice in the zoomed in view of the spots that the energy distribution in each spot was not uniform looking. This is representative of an induced phase distortion that is manifested as a spot locational shift within the Shack-Hartmann wavefront sensor. The small red cross in each image is the centroid location that is based on the distribution of the encircled energy. This centroid location as compared to the same regionally assigned reference centroid is what was used to calculate a phase slope. The mean of the variance from the ensemble of calculated slopes was then used to calculate a Fried parameter, $r_0$. This is described by equation 99 as

$$\langle E^2 \rangle = 0.134 \left(\frac{\delta}{r_0}\right)^{5/3} \tag{99}$$

where $\langle E^2 \rangle$ is the mean of the variance from the grid of slope vectors calculated in radians and $\delta$ is the grid spacing. When analyzing the data, some spots were difficult to centroid and were excluded. However, for all calculation a minimum of 345 spots were used. This allows for sufficient data to compute a mean of the variance across the Shack-Hartmann wavefront sensor array.

Results from the experiment are summarized in Table 5. This table shows the measured Fried parameter value for each phase screen individually, which serves as the truth measurement, and compares that to the calculated Fried Parameter based on the TARDIS methodology as summarized by Equation 97. Looking at the phase screens that are further away from the source, screens 2 and 3, are what is used to demonstrate the processing methodology and quantify the capability to show proof of processing concept. It is shown that there are relatively large differences in percent error, 18.90% and 20.00% respectively. This was deemed acceptable due to the simplified nature of the experiment and the likely errors induced on the wavefront from non-perfect phase screen placement between individual measurement and layered measurement. Additional benefits from this experiment include: development of computer processing software that is more robust to non-perfect data that is collected as compared to pure M&S data, and analysis of difficult to centroid spot filtering that will translate into benefits for analyzing the on-sky data.

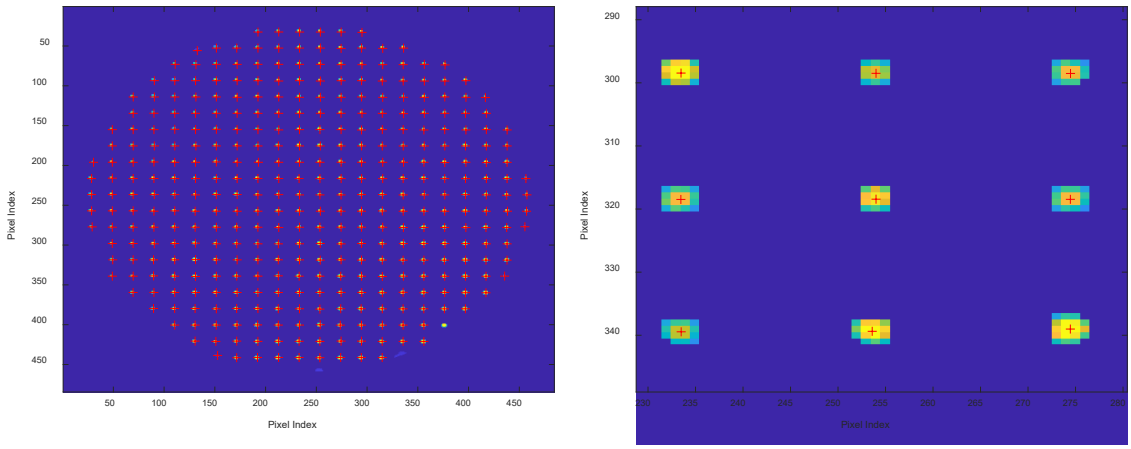


Fig. 73. (left) Example image from Shack-Hartmann wavefront sensor with phase screens in the path, and (right) zoomed in view of the spots

Table 05. Measured $r_0$ values for each screen individually and calculated using TARDIS methodology

| | Screen 1 | Screen 2 | Screen 3 |
|---|---|---|---|
| **Calculated** | 0.0134 | 0.0119 | 0.0084 |
| **Truth** | 0.0134 | 0.0148 | 0.0105 |
| **Difference** | 0 | 0.0028 | 0.0021 |
| **Percent Error** | 0 | 18.90% | 20.00% |

## 8.3 First Atmospheric Measurement Data Collections

Prior to collecting dynamically ranged Rayleigh beacon data, starlight data was collected. This was done to test out the sensing system beam relay, the quality of the spots on the Shack-Hartmann wavefront sensor, the ability of the data processing algorithms to estimate $r_0$, and to get a sense of the relative strength of the turbulence local to the John Bryan Observatory. An example of the starlight data captured by the Shack-Hartmann wavefront sensor is shown in Figure 74. Here you can see a relay of the collecting telescopes pupil, a circle with a central obscuration. Also you can see the focused spot from each lenslet in the Shack-Hartmann sensor system.

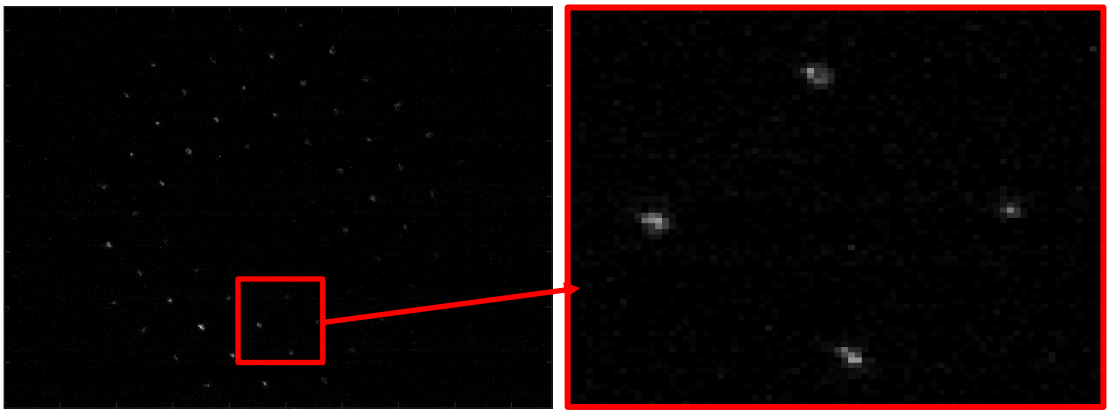

Fig. 74. (left) Star data captured on the Shack-Hartmann wavefront sensor, and (right) zoom in on four spots to show intensity variations representative of zonal wavefront tilts in the system's pupil plane

Next, the centroid of each individual spot from the star data was determined. These centroids were compared against a calibrated center location for each lenslet. The difference between this spot centroid and true center was used to calculate the mean of the variance in radians, an angular difference based on the lenslet focal length. An example of the calculated spot centroids is shown in Figure 75.

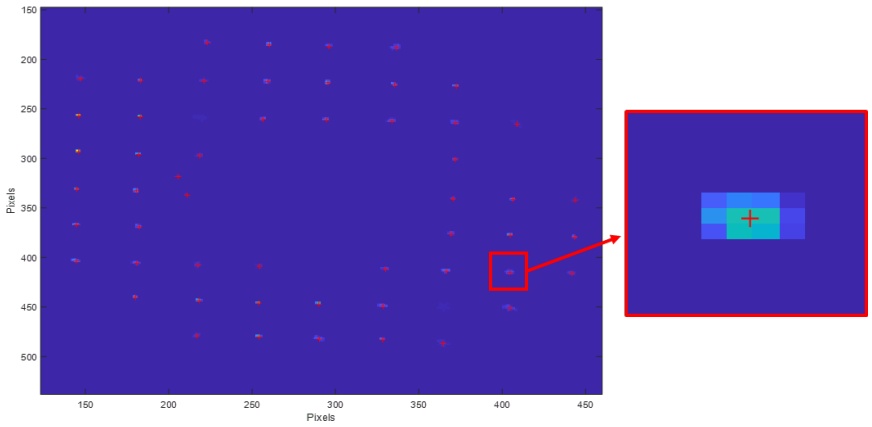


Fig. 75. Star data spot centroid example. Red plus sign is the calculated sub-pixel center.

A set of 200 Shack-Hartmann wavefront sensor images were captured over the course of 10s of seconds. Out of these 200 images, 5 frames were removed due to poor data quality. Poor data quality constituted of identified mean of the variance calculations that were outside of expected bounds, and after investigation these data files had too few spots visible above the background threshold. This could be due to weather conditions and clouds. On the night of this data collect many wispy high altitude clouds were present. It is even evident in Figure 75 that some spots did not produce a centroid. This is because the spot energy was either not present or too weak to calculate an exact energy center. Within each frame, a minimum of 46 spots were used for each calculation of $r_0$. For the calculation of $r_0$ it is not important if a few spots are missing, or even if in each frame different spots are missing. Since $r_0$ is based on the mean of the variance of all the spatially separated spots, assuming phase tilt is the main contribution to spot deviation from center,

the only requirement for an accurate calculation is to have enough data points that outlier data points can be filtered out without dramatically effecting data quality. To ensure the sample size is sufficient we assigned a confidence level and used the standard sample size calculation found in most statistical models. An alternative approach would be use to the generalized simple rule of 10 samples per independent variable. The equation used to calculated sample size is

$$n = \left(\frac{Z\sigma}{E}\right)^2 \tag{100}$$

where $n$ is the sample size, $Z$ is the value from the table of probabilities of the standard normal distribution for the desired confidence level 1.96 for 95% in this case, $\sigma$ is the standard deviation of the outcome of interest, and $E$ is the margin of error that is specified as acceptable. For this analysis, the standard deviation from the data was used after it was collected, and an acceptable margin of error was determined to be half the standard deviation. This results in a sample size of at least 16 samples as a minimum. The alternative generalized approach results in only 10 samples required. In either case, four to five times the required sample size was obtained as a minimum. The results of the calculated $r_0$ from the star data is summarized in Figure 76. Figure 76 shows the resultant $r_0$ value from each captured Shack-Hartmann wavefront sensor, along with a horizontal solid blue line indicative of the mean and two dashed red lines that equate to one standard deviation from the mean. The data collected on the star produced a mean $r_0$ of 0.0675 m with a standard deviation of 0.0134 m, a maximum of 0.116 m, and a minimum of 0.0392 m.

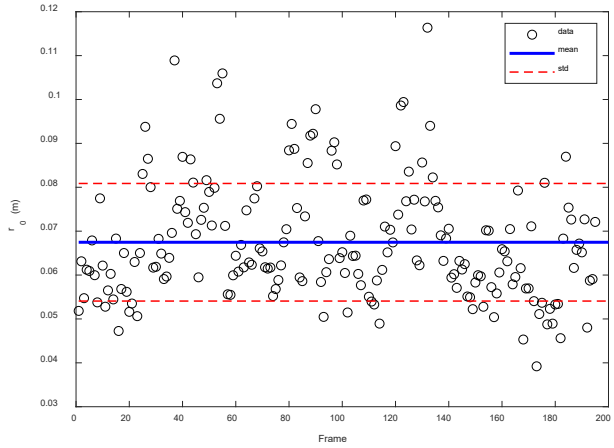


Fig. 76. Resultant $r_0$ estimated from starlight data collected with the TARDIS sensing system

First atmospheric turbulence measurements were taken during a data collection campaign that took place from January 2021 through June 2021. During this time, adjustments were made to the TARDIS that lead to a successful proof of concept data collect. These adjustments were targeted to increase signal strength and involved conditioning the polarization state of the returning scattered laser light and adding pupil relay optics to further condense light sent into the Shack-Hartmann wavefront sensor. This lead to obtaining single pulse data from varied beacon heights that were taken in rapid succession at 200 Hz. Each of these individual measurements produced an estimate of the total path integrated turbulence strength between the beacon location and collecting telescope. Since each laser pulse produced a sensed beacon from a different height and they were taken in rapid succession such that the atmosphere could be considered unchanging, these individual measurements could be used to produce a turbulence profile estimate as outlined by Equations 96 and 97 in this section, further described in previous sections, and described in detail in the listed references.

The proof-of-concept data collections presented here were taken on the night of May 12th, 2021 to the morning of May 13th, 2021 at the John Bryan Observatory utilizing TARDIS. On this night laser operations were substantially long in duration so that ample data could be collected. This data consisted of Shack-Hartmann wavefront sensor data as shown in Figure 77 that was indexed to a sequence of frames where each frame was from a distinctly different range. The ranges used are shown in Table 06. These ranges are not fixed, but chosen by the data collection user. Here, the ranges were chosen for high return signal strength to highlight the turbulence profile estimation methodology as well as to show the range of the beacon before SNR is no longer detectable. These are both single examples, but shed light on the capabilities of the TARDIS system and methodology. Figure 78 shows the beacon in operation as viewed from inside the telescope room, (left image depicted) and from the lawn exterior to the observatory building (right image depicted). Figure 79 shows the TARDIS telescope and beam launch system as configured for the proof-of-concept data collects (left image depicted) and the sensing system on the back of the telescope (right image depicted). This sensing system was assembled to optimize the spot size and collimation through the beam relay system such that laser energy from all altitudes tested were able to produce spots on the Shack-Hartmann wavefront sensor that were measurable. As shown in Figure 79, spots on the wavefront sensor were not perfect circular spots, but instead has shape and structure. This made it difficult to produce accurate centroids for many of the spots. However, after using a 35% threshold filter and conducting a localized region of interest signal filter spots were captured and used for turbulence profile estimation. Many poor data quality images were discarded for this analysis, but enough were used to prove the concept of dynamic ranging with TARDIS to provide an estimate of the turbulence strength profile.

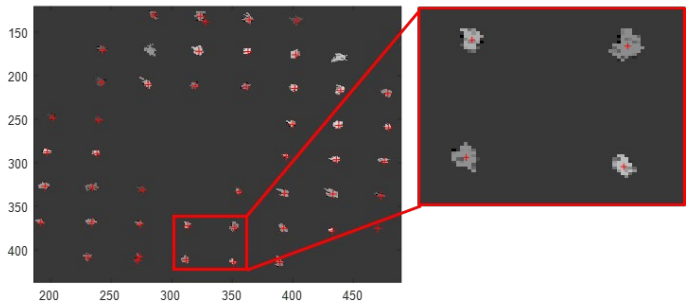


Fig. 77. Example Shack-Hartmann wavefront sensor image used as a single range beacon measurement

Table 06. Listing of ranges used for turbulence profile estimation

| | Ranges (m) | Slant Angle (degrees) | Data Quality (poor, average, good) |
|---|---|---|---|
| **Data Collect 1** | 800, 1000, 1100, 1200, 1300, 1400, 1500, 1600, 1700, 1800 | 45 | Average |
| **Data Collect 2** | 300*, 600, 900, 1200, 1500, 1800, 2100, 2400, 2700, 3000, 3300 *Poor data quality due to defocused SHWFS spots | 45 | Poor*, Average |
| **Data Collect 3** | 500, 900, 1300, 1700, 2100, 2500, 2900, 3300 | 45 | Good |

Fig. 78. Captured images of the TARDIS laser beacon (Photo Credit: Steven Zuraski)

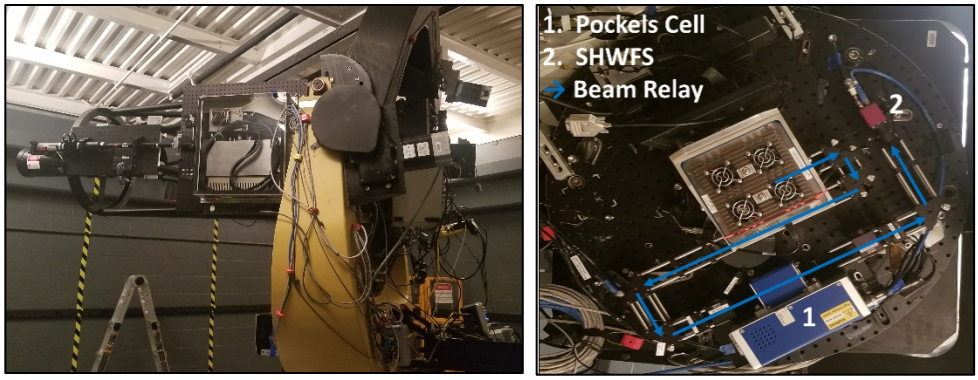


Fig.79. (left) TARDIS Beam Launch System and (right) TARDIS Sensing System

For Data Collect 1, as designated in the Table 6, dynamic ranges from 800m to 1800m were used with a range depth of 450m. This data was taken on May 12th, 2021 from 23:32 UTC to 23:36 UTC and consisted of 20,556 frames of data. Approximately 50% of the collected data was used for the analysis presented in Data Collect 1. The range depth and shorter range to the beacon created large overlaps in each range bin, but was chosen to provide high SNR data. This overlap in range depth as compared to center ranges in a dynamic sequence act like a smoothing filter, effectively lessening the estimation of turbulence strength between each range center. Doing this cancels out any localized turbulence strength peaks, showing more of a turbulence strength profile average-like change with altitude. Specific results are shown in the Figures 80 to 82 in Section 8.4. The camera settings used for this data collect were 19ms exposure time and a 40dB gain. The camera exposure time was not critical as the Pockels Cell operates as a fine shutter for the camera.

For Data Collect 2, as designated in Table 6, dynamic ranges from 300m to 9900m were used with a range depth of 450m. This data was taken on May 13th, 2021 from 00:57 UTC to 01:03 UTC and consisted of 37,691 frames of data. Approximately 30% of the collected data was used for the analysis presented in Data Collect 2. The lower percentage of data used was due to the chosen ranges and SNR. At farther ranges the SNR becomes too low to detect a signal and thus many

Shack-Hartmann wavefront sensor images were discarded out of the dataset. Additionally, at middle to far beacon ranges centroiding the spots on the Shack Hartmann wavefront sensor was difficult. This contributed to more data being filtered out, resulting in used data from ranges of 300m to 3300m. Improved SHWFS spot signal processing could increase the range to approximately 7800m as spots were faintly visible to the human eye, just at a very low contrast with lots of noise across the image. Overall, there was still plenty of data to show the extended range utility of the TARDIS system.

For Data Collect 3, as designated in Table 6, dynamic ranges from 500m to 3300m were used with a range depth of 450m. This data was taken on June 6$^{th}$, 2021 from 03:43 UTC to 03:52 UTC and consisted of 59,132 frames of data. The gamma setting on the camera was changed from 0.4 to a value of 1.0 for this data collection. This reduced the background noise and allowed for a threshold filter of 15% to be used; effectively producing more accurate spot centroids as compared to prior data collections. Approximately 50% of the collected data was used for the analysis presented in Data Collect 3. The 50% not used was from ranges farther than 3300m and was discarded due to dim signals. Shack-Hartmann wave front sensor spot signals were present however, and may be exploitable with advances in the spot thresholding and centroiding techniques. Data collected from the lowest range of 500m displayed a small amount of defocus in the Shack-Hartmann wavefront sensor spots. It is likely that centroiding accuracy and resultant $r_0$ estimates have possible errors. It is recommended that further research be conducted into spot centroiding in the presence of defocus aberrations.

### 8.4 Results from First Data Collections

Results from Data Collection 1 are shown in Figures 80 and 81. Figure 80 displays the calculated $r_0$ from every 11th frame used for analysis from the first data set, and every 34$^{th}$ frame from the second analyzed data set. This was done just to take a quick look at the data quality to see if $r_0$ values seemed reasonable prior to calculating $C_n^2$ values. From this quick look, the average of the data is shown by the blue line and is approximately 10.5cm and 9.6cm, respectively, with a span from a minimum of approximately 4cm to a maximum of approximately 19cm. This seemed reasonable as the short ranges would effectively produce large $r_0$ estimates correlating to weaker turbulence, and the longer ranges would produce small $r_0$ values correlating to stronger turbulence. It is important to remember that the $r_0$ values are calculated as described by Equation 98, which specifies that $r_0$ is calculated from the mean of the variance from the spatial grid of slope vectors derived from the calculated spot centroids in the Shack-Hartmann wavefront sensor image. Any external influencing function, such as elevated background noise, that contributes to spot centroid inaccuracies and effectively a larger or smaller overall variance mean calculation could bias the $r_0$ calculation towards greater or weaker turbulence strength. This is explored further in Section 8.5 when comparing Data Collect 1 and 2 vs. Data Collect 3.

Figure 81 shows the calculated $C_n^2$ values from Data Collections 1 and 2. $C_n^2$ is calculated as described by Equation 97, where neighboring $r_0$ values are used to generate a segmented $C_n^2$ estimate. It is important to analyze the TARDIS setup, specifically how it relates the range and range depth assignments to $C_n^2$ segments. Depending on the choices, the $C_n^2$ segments could be insensitive to localized rapidly changing strength spikes in the turbulence strength profile. Approximately 10,000 and 11,000 Shack-Hartmann wavefront sensor images went into the data analysis contributing to the plots shown. The black dots show the calculated mean for each altitude region with a dashed trend line connecting them. The red triangle bars show one standard deviation

within the data that corresponds to that altitude region. From Data Collection 1, it is interesting to notice that there is a larger standard deviation in the middle altitude regions on this plot, specifically those from 700m to 900m in altitude which corresponds to beacon ranges of 1000m to 1300m. For this data collection the lens relay system was optimized around a beacon range of 1250m, which means that beacon ranges near here produced the tightest focused spots in the system. It is likely that measurements around the optimization range for the TARDIS system are most sensitive, and thus capture the instantaneous localized turbulence strengths effects best. Outside the optimized range, Shack-Hartmann spots are still produced and capable of being centroided, however, further work should be conducted to quantify the influence on centroid accuracy of larger slightly defocused spots in a Shack-Hartmann wavefront sensor. Overall, as shown in Figure 81, the data collected was able to produce a reasonable turbulence strength profile. This serves as a proof-of-concept data collect that the TARDIS system can function to produce estimates of the turbulence strength profile based on direct measurements of the turbulence induced perturbed wavefront from the backscattered Rayleigh beacons taken in rapid sequence from varied ranges.

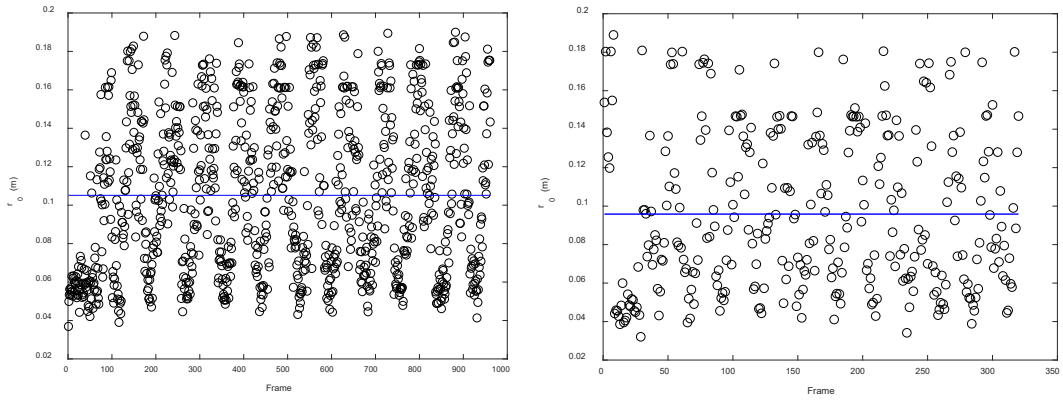


Fig. 80. Plotted $r_0$ vs frame showing data collected on May 12th, 2021. (left) Data shows every 11th frame from a sweep of dynamic ranges from 800m to 1800m with a step size of 100m. (right) Data shown is every 34th frame from a sweep of 300m to 3300m with a step size of 300m; the blue lines shows the average $r_0$

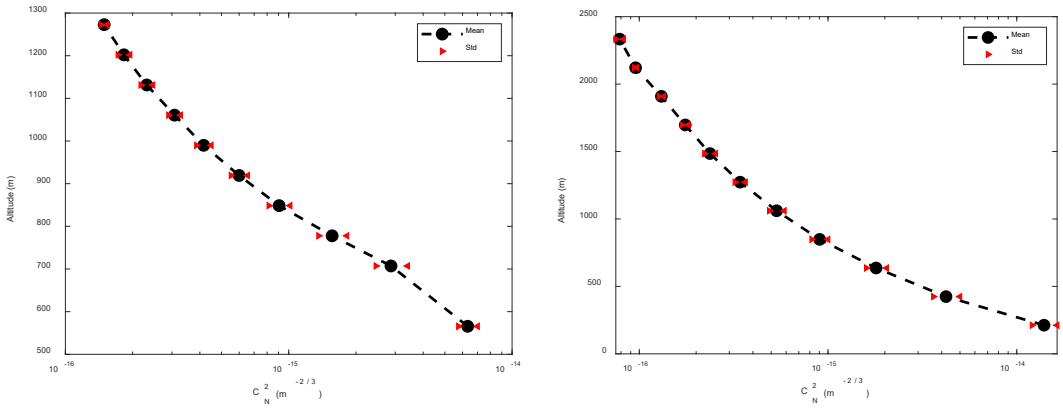


Fig. 81. (left) Analyzed collected turbulence strength data from May 12th, 2021, 23:32 UTC to 23:36 UTC consisting of 20,556 frames with 19ms exposure time, 40dB gain, taken from TARDIS pointing at 45 degrees in elevation to the West. (right) Analyzed collected turbulence strength data from May 13th, 2021, 00:57 UTC to 01:03 UTC consisting of 37,691 frames with 19ms exposure time, 40dB gain, taken from TARDIS pointing at 45 degrees in elevation to the North.

Data Collect 3 was taken at a later date on June 6th, 2021. Improvements were made to the system for this data collection as compared to the prior collects from May. Most notably was the change in the gamma setting on the camera from a value of 0.4 to 1.0. This resulted in lower noise present in the images, but also made the peak signal strength fainter. Overall, this change likely improved the processing in the centroiding algorithm as the threshold used was able to be lowered to 15% from 35%, and likely increased the centroiding accuracy. By observing the data, the variance in the spatially varied Shack-Hartmann wave front sensor spots decreased. This resulted in weaker turbulence estimations, using the algorithm previously described. [52] It is possible that this specific data collect happened on a day where the turbulence strength was weaker, however, analysis presented in the 8.5 Discussion section may indicate otherwise.

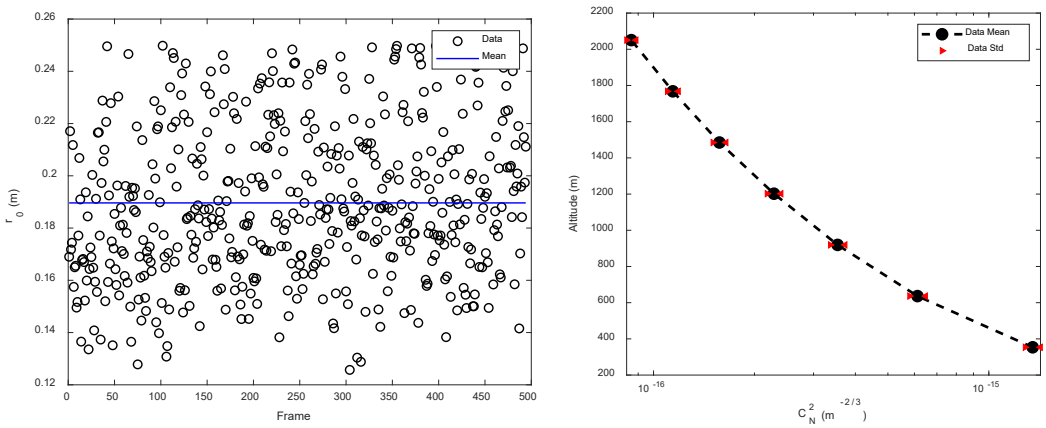


Fig. 82. (left) plotted $r_0$ vs frame showing data collected on June 6th, 2021. (right) Analyzed collected turbulence strength data from June 6th, 2021, 03:43 UTC to 03:52 UTC consisting of 59,132 frames with 19ms exposure time, 40dB gain, taken from TARDIS pointing at 45 degrees in elevation to the Northeast.

### 8.5 Discussion

Looking at the data, it is important to compare it to theory to see if some of the base trends match well with established models. These comparisons are shown in Figure 83. In Figure 83, the data is plotted against the Hufnagel-Valley 10-10 model with modified ground layer terms and a weather parameter derived model utilizing Tatarski's equations for estimating $C_n^2$ from $C_T^2$. The Hufnagel-Valley 10-10 model was chosen as a starting point as the average of the collected data had an $r_0$ value close to 10 cm. The weather model has data derived from a Numeric Weather Prediction (NWP) that stems from satellite data captured within 3 hours of each data collection from a gridded location in proximity of the John Bryan Observatory, 39.79 degrees North and 83.86 degrees W.

Data Collection 1 is shown in the left plot of Figure 83. Here the Hufnagel-Valley 10-10 model, the green solid line curve, was plotted. This model is described by Equation 23, except turbulence

strength was added within the boundary layer to match the data more closely. This was done by manipulating the $A$ coefficient to $9 \times 10^{-15}$ and the $H_A$ coefficient to 300m. Further manipulation of the Hufnagel-Valley model could yield better results. The blue dashed line curve is a weather parameter derived model. Here the modeled values were multiplied by a factor of 40 to shift the curve towards stronger turbulence values. The weather parameter model seemed to under predict the strength of the turbulence by 2-3 orders of magnitudes even prior to the shift in turbulence strength. This could be for a number of reasons. It was noted in the weather data file that the surface visibility was 22.8km. This seems a bit of an over estimate. Additionally, a haze was noted by the TARDIS operators on the night of the data collect. So, this exceptionally high visibility estimate could have played a role in lessening the strength of turbulence. Also, the surface level temperature estimate was listed at 42 degrees Fahrenheit. This was a low estimate of temperature. It was notably warmer in the 60-70 degree range during the data collection. Shifting the data to warmer temperatures in the Tatarski model would have an effect of increasing the strength of turbulence. It is also possible that the TARDIS is over predicting the strength of the turbulence. This would likely stem from the measurements on the Shack-Hartmann wave front sensor. When looking at the raw outputs, there was a high level of noise present due to the 40dB setting on the camera. This effected the filter functions employed to nullify the noise effect and also influenced the centroiding algorithm. It is possible that this could result in larger over estimates of localized tilt on the measured wave front. If this over estimate was uniformly random in tilt direction and strength the variance calculation used to estimate $r_0$ could be influenced towards stronger estimates of path averaged turbulence strength.

Data Collection 2 is shown in the right plot of Figure 83. Here the Hufnagel-Valley 10-10 model, the green solid line and green dashed line curves, were plotted. Again, turbulence strength was added within the boundary layer to match the data more closely. For the solid green curve, the $A$

coefficient to $15 \times 10^{-15}$ and the $H_A$ coefficient to 300m. This came close to matching data at low altitudes. For the dashed green curve, the $A$ coefficient was $4.5 \times 10^{-15}$, the typical value for the Hufnagel-Valley 10-10 model, and the $H_A$ coefficient was set to 500m. This came close to matching data at higher altitudes. Further manipulation of the Hufnagel-Valley model could yield better results. The dashed blue curve is a weather parameter derived model. Here the modeled values were multiplied by a factor of 20 to shift the curve towards stronger turbulence values. The weather parameter model seemed to under predict the strength of the turbulence by 2 orders of magnitude even prior to the shift in turbulence strength. It is possible that this model under estimates turbulence for the same reasons stated for Data Collection 1. It is also possible that TARDIS may slightly over estimate the turbulence strength for the same reasons outlined in Data Collection 1. Ultimately, further analysis and development of the weather models and how the TARDIS system data is collected and analyzed could be done to shed light onto why there are differences or possibly bring closer agreement in these models. TARDIS does however, seem to agree well with the Hufnagel-Valley 10-10 model as long as the low altitude associated parameters are increased. This hints at the possibility that the Hufnagel-Valley model captures the turbulence scaling with altitude well, but has a small deficiency in capturing the ground layer turbulence. This is a recognized deficiency and is the reason why the $D$ and $H_D$ terms were added to the original equation as shown in Equation 23. These terms were added specifically to capture increased turbulence strength localized to the surface layer.

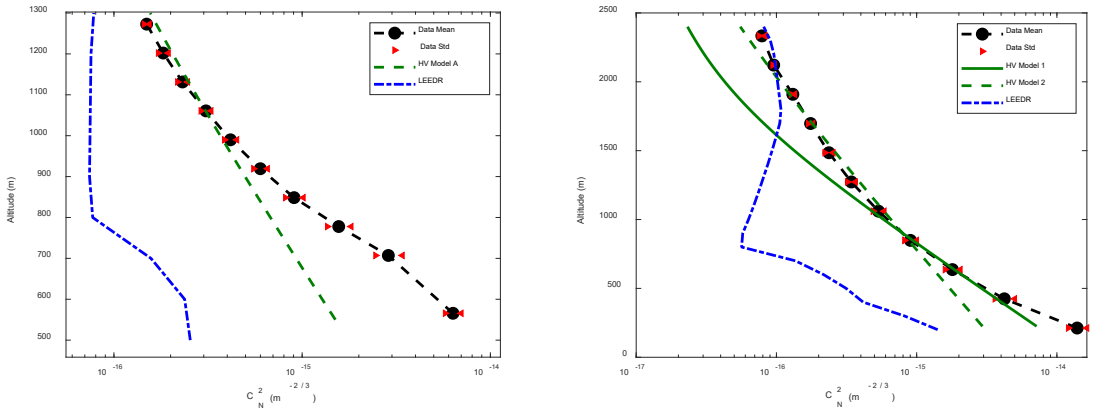


Fig. 83. Comparison of (left) Data Collection 1 and (right) Data Collection 2 to a modified Hufnagel-Valley 10-10 model with extra turbulence strength present within the boundary layer and a weather parameter model derived utilizing Tatarski's equations for estimating $C_n^2$ from $C_T^2$

The results from Data collection 3 are shown in Figure 84 as compared to a modified Hufnagel-Valley 15-12 model and a weather parameter model derived utilizing Tatarski's equations for estimating $C_n^2$ from $C_T^2$. The Hufnagel-Valley model was used to give a relative sense of how the TARDIS derived turbulence profile compared to a standard parameterized model. Here the Hufnagel-Valley 15-12 model was chosen as the starting point. This was chosen because the average $r_0$ from the data collection was close to 15 cm. To better fit the collected data this model had to be modified. The overall strength was multiplied by a factor of 5 to move the green dashed line curve to the right. Also, the height of the $1/e$ boundary layer decay was raised from 100 m to 200 m. This gives a sense that the turbulence strength profile on the 6th of June had localized strong layers, that are not captured by an average $r_0$ value, and additionally, that the boundary layer was likely elevated. A better comparison for the TARDIS data is that of a weather parameter derived model. Atmospheric characteristics as described by weather parameters are the physical phenomena that contribute to the layered interaction that generates turbulence strength profiles as experienced by an optical imaging system. As shown in Figure 84 the weather parameter derived

model matches nicely with the measured data at approximately 750m and above. This adds confidence that TARDIS is making accurate measurements of the turbulence profile. The two profiles depart at low altitudes. There are a variety of possible explanations for this. First, the TARDIS sensing system at low altitudes experiences defocus in the Shack-Hartmann wave front sensor spots. This may lead to inaccuracies in the $r_0$ measurements, and consequentially biased $C_n^2$ evaluations. A more likely explanation is that the range gate depth used for this specific data collect made the TARDIS system insensitive to localized spikes or depressions in the measured turbulence strength estimates. For this data collection a range gate depth of 450 m was used. This is currently a set but fixed value for the TARDIS system. 450 m was chosen so that the SNR at higher altitudes produced a measurable signal. Future advances in TARDIS will remove this limitation so that the system can dynamically range gate while simultaneously dynamically change the range gate depth. When looking at the dashed blue curve in figure 84, the turbulence strength depression only lasts for an altitude range of approximately 300 m. Using a range gate depth larger than 300 m with overlapping separations, the localized turbulence strength weakening was likely missed. The upper and lower tails of the localized turbulence strength depression where turbulence was stronger likely influenced an estimate of the turbulence strength to also be stronger. Other possibilities for model to data mismatch could lie in the formulation of the weather parameter derived model as this type of model is sensitive to small, rapid changes in turbulence strength. It is important to be cognizant of this type of missed effect when using TARDIS to assess the strength profile of atmospheric turbulence. The setup of the TARDIS system should be carefully chosen by the observer so that the intended region of the atmosphere that is under study is captured appropriately.

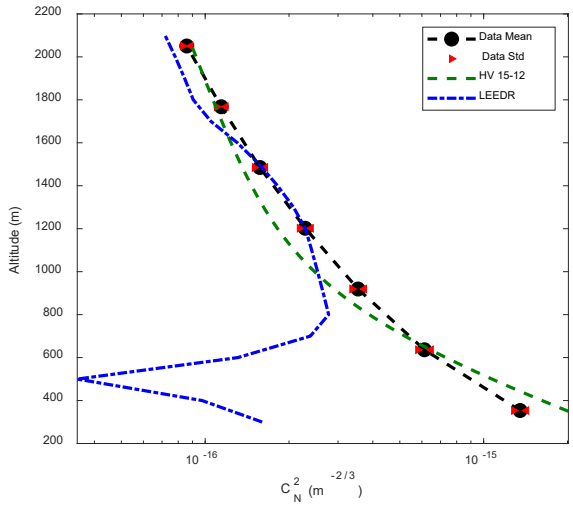


Fig. 84. Comparison of Data Collection 3 to a modified 5X Hufnagel-Valley 15-12 model with the height of the $1/e$ decay raised from 100 m to 200 m and a weather parameter model derived utilizing Tatarski's equations for estimating $C_n^2$ from $C_T^2$

Next steps to improve upon the TARDIS measurement methodology could include utilizing optimized gamma settings on the Shack-Hartmann wave front sensor camera. This would lower the noise and enable more accurate spot centroiding. Additional research could be conducted into methods for more accurate centroiding of a spot on the Shack-Hartmann wave front sensor. There are a number of methods possible each for thresholding, filtering, and centroiding the Shack-Hartmann wave front sensor spots. Which would work best on the TARDIS system is still a topic for future research. Other significant improvements to TARDIS could be acquisition of a more powerful laser. The laser used was chosen to suit a proof-of-concept system for performance and cost reasons. Laser systems exist currently that have improved beam quality and high pulse energy densities. These two attributes would greatly improve the TARDIS methodology, but come at a cost greater than $225,000 for a single system.

The next phase of collecting data with the TARDIS system involves conducting a co-located test with DELTA-Sky. DELTA-Sky is a turbulence estimation system developed by MZA Inc. It produces estimates of the turbulence strength based on differential jitter covariance that is present in point features within a set of passively collected images. DELTA-Sky can take data utilizing the moon as an extended source, where the moon crater centroids act as point features. From this the system estimates turbulence strength profiles. It will be interesting to compare and contrast the Delta-Sky turbulence profile estimates with the TARDIS estimates, as both methodologies are formulated around different base assumptions and measurement techniques. TARDIS is a near instantaneous direct measurement of perturbed wavefronts built from a sequence of dynamically ranged Rayleigh beacons that are stacked to produce estimates of the turbulence strength with altitude. DELTA-Sky operates around fourth order statistics that are an in-situ measurement that can be related to turbulence strength. Then through a geometry-based weighting schema, DELTA-Sky is able to produce measurement influenced estimates of the turbulence strength profile. Performing this comparison will possibly add validity to both techniques as well as highlighting the strength and weaknesses of each.

### 8.6 Conclusions

This body of research provides a novel means for quantifying the strength profile of atmospheric turbulence. Utilizing the outlined methodologies, a direct measurement of the perturbed wavefront is used which differs fundamentally from other means of estimating a turbulence strength profile. [26, 6, 27, 16] Due to this difference, the method of utilizing a dynamically ranged beacon to produce turbulence profile estimates could be used to add confidence to other methodologies or be used as an independent measurement technique that is not susceptible to the same set of error source influences. Furthermore, since this technology utilizes direct measurements of the wavefront, it is

conceivable that this could be linked to an adaptive optics system used for image correction. In particular, very large next generation telescopes [25] have difficulty providing adequate full field adaptive correction for the atmosphere based on total path integrated volume measurements. This is why these programs are exploring the uses of multiple beacons from varied ranges, and turbulence profile estimation techniques. Lastly, this technology is well suited to be coupled with a long-range projection system. Similar to a passive imaging system, a beam projection system could benefit from knowledge of the profiled turbulence strength. [62]

*Acknowledgments*

This effort has been supported by the Air Force Research Labs Sensors Directorate and the Air Force Institute of Technology Center for Directed Energy. Additionally, the authors would like to thank Ethan VanTilburg, Luke Weisenbach, and Matthew Wilson from Applied Optimization Inc. for their contributions to the development of TARDIS and data collections that took place at the John Bryan Observatory.

# IX. Conclusions

This body of research provides a new and innovative method for quantifying the strength profile of atmospheric turbulence utilizing dynamically ranged Rayleigh beacon measurements. There are multiple novel aspects that were born from this research. First, this is the first time the concept of a dynamically ranged beacon was formulated where a wavefront sensor could be used to take direct measurements of the perturbed wavefronts from multiple beacons in sequence at a fast enough rate that the atmospheric turbulence could be considered unchanging. Utilizing this measurement scheme, an algorithm was developed to exploit the unique nature of the data collect to produce an estimate of the turbulence strength along the viewing path. This algorithm was first tested through M&S and proved to produce accurate estimates of the turbulence strength profile. A laboratory based experiment was later designed to test this algorithm and proved to verify the M&S results. Next, Rayleigh beacon performance models were constructed to guide the design and build of a dynamically ranged Rayleigh beacon system. These performance models were optimized around maximizing the return signal strength for the range of beacon locations envisioned. After this, an industry part survey was conducted and components were chosen and procured. The components purchased were not the highest performing parts, but instead were good enough to prove this concept while also being economical so that costs were realizable within the budgetary constraints. The components were assembled and underwent laboratory testing to verify they met the required specification needed for creating a dynamically ranged Rayleigh beacon system. Next, these tested sub-systems were integrated into the telescope system at the John Bryan Observatory, and the full system was designated as the Turbulence and Aerosol Research Dynamic Interrogation System, also known as TARDIS. During initial on-sky testing it was discovered that the sharp spots were not producible on the Shack-Hartmann wavefront sensor. This resultant effect was traced back to the Pockels cell not being able to fully block all light. After some investigative research, a niche effect within the Pockels cell involving the degree of rotation or the polarized light in the presence

of a curved light field was analyzed, and deemed to be the root cause of light leakage. Since this light leakage was from near field light, it was significantly greater in strength than light originating from the beacon. This light leakage discovery was simply solved by inserting a couple spatial light filters into strategic spots in the sensing system, and making a small change to the original light relay design so that light passing through the Pockels cell was collimated.

Now that a new TARDIS sensing system was rebuilt, the system was ready to collect data. In parallel, a lab based system was constructed to test out the data processing algorithms and data acquisition systems. This lab system was simple and used static phase screens to emulate turbulence layers. This setup was successful in testing the data acquisition processes and data processing algorithms on non-synthetic data. The TARDIS system at this time was now producing strong signal content data on the Shack-Hartmann wavefront sensor for the laser beacon returns. Data captured from multiple ranges proved the concept of a dynamically ranged Rayleigh beacon. These initial captured estimates of $C_n^2$ provided a preliminary dataset for comparing TARDIS data to various models, such as weather parameter derived models using Tatarski's formulation.

Next steps beyond the presented research is to continue to collect data with the dynamically ranged Rayleigh beacon system so that a body of data collects under varied weather conditions and season variations can be collected. This will serve as a turbulence strength profile climatology for the John Bryan Observatory site and will be a valuable data source for future research. Future research could include doing an in-depth study on TARDIS data compared to traditional climatological models, weather parameter-based models, and alternative means of estimating turbulence strength profiles. These comparative tests may lead to discoveries in the alternate methodologies or enhancements that could be made to the TARDIS turbulence profile measurement system.

Overall, this body of research started with a novel concept for a method to directly measure turbulence strength profiles. That concept was optimized into a system point design where proof of concept components could be procured for affordable costs. The performance of each component was verified in the laboratory and the TARDIS was built. Small system discoveries were made along the way that were prohibitive to collecting proof of concept data, but each was eventually solved. Lastly, a proof of concept data collection was made that demonstrated the validity of the original concept, making a dynamically ranged Rayleigh beacon a novel and viable means for producing measurements of the turbulence strength profile.

## Bibliography


[1] A. Cortés, B. Neichel, A. Guesalaga, J. Osborn, F. Rigaut, D. Guzman. "Atmospheric turbulence profiling using multiple laser star wavefront sensors." *Monthly Notices of the Royal Astronomical Society* 427.3 (2012): 2089-2099.

[2] A. de la Nuez Cruz, B. Garcia-Lorenzo, J. Fuensalida, M. Rodriguez-Hernandez. "Atmospheric turbulence profiling at the Teide Observatory: comparison and calibration of SODAR and SCIDAR measurements." Optics in Atmospheric Propagation and Adaptive Systems X. Vol. 6747. International Society for Optics and Photonics, 2007.

[3] A. Guesalaga, J. Kolb, R. Donaldson, J. Valenzuela, S. Oberti, B. Neichel, J. Paufique, and P. Madec. "An on-line turbulence profiler for the AOF: on-sky results." *Adaptive Optics Systems VI*. Vol. 10703. International Society for Optics and Photonics, 2018.

[4] A. Lambert, Andrew, et al. "Turbulence profiling using extended objects for Slope Detection and Ranging (SLODAR)." Image Reconstruction from Incomplete Data IV. Vol. 6316. International Society for Optics and Photonics, 2006.

[5] A. Reeves, R. Myers, T. Morris, A. Basden, N. Bharmal, S. Rolt, D. Bramall, N. Dipper, and E. Younger. "DRAGON, the Durham real-time, tomographic adaptive optics test bench: progress and results." *Adaptive Optics Systems IV*. Vol. 9148. International Society for Optics and Photonics, 2014.

[6] A. Tokovinin, and V. Kornilov, (2007). Accurate seeing measurements with MASS and DIMM. *Monthly Notices of the Royal Astronomical Society*, *381*(3), 1179-1189.

[7] A. Tokovinin. "Turbulence profiles from the scintillation of stars, planets and moon." *Workshop on Astronomical Site Evaluation (Eds. I. Cruz-González, J. Echevarría & D. Hiriart)*. Vol. 31. 2007.

[8] C. Baranec, M. Lloyd-Hart, N. Milton, T. Stalcup Jr, J. Georges III, M. Snyder, N. Putnam, and J. Angel. "Progress towards tomographic wavefront reconstruction using dynamically refocused Rayleigh laser beacons." Advancements in Adaptive Optics. Vol. 5490. International Society for Optics and Photonics, 2004.

[9] C. Carr, S. Zuraski, Steven, J. Tompkins, S. Fiorino. “Comparing DELTA-Sky turbulence measurements to modeled Cn2 profiles from numerical weather data” *Multispectral Sensing Symposium Parallel Conference 2018*.

[10] C. W. Higgins, et al. "The effect of scale on the applicability of Taylor’s frozen turbulence hypothesis in the atmospheric boundary layer." Boundary-layer meteorology 143.2 (2012): 379-391.

[11] D. J. Laidlaw, et al. "Turbulence profiling for adaptive optics tomographic reconstructors." Adaptive Optics Systems V. Vol. 9909. International Society for Optics and Photonics, 2016.

[12] D. L. Fried and J. F. Belsher, "Analysis of fundamental limits to artificial-guide-star adaptive-optics-system performance for astronomical imaging," J. Opt. Soc. Am. A 11, 277-287 (1994).

[13] D. Thomson, R. Coulter, and Z. Warhaft. "Simultaneous measurements of turbulence in the lower atmosphere using sodar and aircraft." *Journal of Applied Meteorology* 17.6 (1978): 723-734.

[14] E. Bengt, “The Refractive Index of Air,” *Metrologia* 2, 71-80 (1966).

[15] Eskma Optics. Ultrafast Pulse Picking Systems. URL. eksmaoptics.com/out/media/EKSMA_Optics_Pulse_Picking_Systems.pdf.

[16] G. Gimmestad, M. Dawsey, D. Roberts, J Stuart, J Woods, F. Eaton. "LIDAR system for monitoring turbulence profiles." *Ground-based and Airborne Telescopes*. Vol. 6267. International Society for Optics and Photonics, 2006.

[17] G. Tyler. "Adaptive optics compensation for propagation through deep turbulence: a study of some interesting approaches." *Optical Engineering* 52.2 (2012): 021011.

[18] J. A. Georges, P. Mallik, T. Stalcup, J. R. P. Angle, and R. Sarlot, "Design and testing of a dynamic refocus system for Rayleigh laser beacons." *Adaptive Optical System Technologies II*. Vol. 4839. International Society for Optics and Photonics, 2003.

[19] J. Beckers. "Detailed compensation of atmospheric seeing using multiconjugate adaptive optics." Active Telescope Systems. Vol. 1114. International Society for Optics and Photonics, 1989.

[20] J. D. Schmidt, Numerical Simulation of Optical Wave Propagation with Examples in MATLAB, SPIE Press, Bellingham, Washington (2010).

[21] J. Georges III, P. Mallik, T. Stalcup, J. Angel, R. Sarlot. "Design and testing of a dynamic refocus system for Rayleigh laser beacons." *Adaptive Optical System Technologies II*. Vol. 4839. International Society for Optics and Photonics, 2003.

[22] J. Georges III, T. Stalcup, J. Angel, P. Mallik. "Field tests of dynamic refocus of Rayleigh laser beacons." *Astronomical Adaptive Optics Systems and Applications*. Vol. 5169. International Society for Optics and Photonics, 2003.

[23] J. McCrae, S. Bose-Pillai, and S. Fiorino. "Estimation of turbulence from time-lapse imagery." *Optical Engineering* 56.7 (2017): 071504.

[24] J. O. Kondo, O. Kanechika, and N. Yasuda, "*Heat and momentum transfers under strong stability in the atmospheric surface layer,*" Journal Atmos. Sci., 35, 1012–1021; 1978.

[25] J. Osborn, "Scintillation correction for astronomical photometry on large and extremely large telescopes with tomographic atmospheric reconstruction." Monthly Notices of the Royal Astronomical Society 446.2 (2015): 1305-1311.

[26] J. Osborn, R. Wilson, T. Butterley, H. Shepherd, M. Sarazin, Profiling the surface layer of optical turbulence with SLODAR, Monthly Notices of the Royal Astronomical Society, Volume 406, Issue 2, August 2010, Pages 1405–1408, https://doi.org/10.1111/j.1365-2966.2010.16795.x

[27] J. Osborn, T. Butterley, D. Föhring, and R. Wilson, (2015, March). Characterising atmospheric optical turbulence using stereo-SCIDAR. In *Journal of Physics: Conference Series* (Vol. 595, No. 1, p. 012022). IOP Publishing.

[28] J. R. P. Angel, "Dynamic refocus for laser beacons," Science with the LBT, ed. Tom Herbst, Sponsored by the Max-Planck Society and the LBT Beteiligungsgesellschaft, Proceedings of a Workshop held at RingbergCastle, Bavaria, July 2000, pp. 21-25.

[29] J. Ruoff and M. Totzeck, "Orientation Zernike polynomials: a useful way to describe the polarization effects of optical imaging systems." *Journal of Micro/Nanolithography, MEMS, and MOEMS* 8.3 (2009): 031404.

[30] J. Valenzuela, C. Béchet, A. Garcia-Rissmann, F. Gonté, J. Kolb, M. Louarn, B. Neichel, P. Madec, and A. Guesalaga. "Turbulence profiling methods applied to ESO's adaptive optics facility." *Adaptive Optics Systems IV*. Vol. 9148. International Society for Optics and Photonics, 2014.

[31] J. W. Hardy, Adaptive Optics for Astronomical Telescopes. Oxford University Press, Inc. New York, NY, (1998).

[32] L. C. Andrews, R. L. Phillips. *Laser Beam Propagation through Random Media*. SPIE Press. 2005.

[33] M. C. Roggemann, B. Welsh, P. Gardner, R. Johnson, B. Pedersen. "Sensing three-dimensional index-of-refraction variations by means of optical wavefront sensor measurements and tomographic reconstruction." Optical Engineering 34.5 (1995): 1374-1385.

[34] M. Hart, N. Milton, K. Powell, C. Baranec, T. Stalcup, D. McCarthy, and C. Kulesa. "Wide-field image compensation with multiple laser guide stars." *Proceedings of the Advanced Maui Optical and Space Surveillance Technologies Conference, Editor. S. Ryan*. 2009.

[35] M. Lloyd-Hart, J Georges, J. Angel, G. Brusa-Zappellini, P. Young. "Dynamically refocused Rayleigh laser beacons for atmospheric tomography." Adaptive Optics Systems and Technology II. Vol. 4494. International Society for Optics and Photonics, 2002.

[36] M. Lloyd-Hart, S. Jefferies, E. Hege, and J. R. P. Angle, "New approach to Rayleigh guide beacons." *Adaptive Optical Systems Technology*. Vol. 4007. International Society for Optics and Photonics, 2000.

[37] M. Tallon, R. Foy. Adaptive telescope with laser probe: isoplanatism and cone effect. A&A, 235:549{557, 1990.

[38] MZA. *MZA DELTA PM-02-600 Specifications*. *MZA DELTA PM-02-600 Specifications*, www.mza.com/doc/misc/MZA_DELTA_PM-02-600_Specifications.pdf.

[39] R. A. Chipman, "Polarization analysis of optical systems, II." *Polarization Considerations for Optical Systems II*. Vol. 1166. International Society for Optics and Photonics, 1990.

[40] R. Avila, J. Vernin, and E. Masciadri, "Whole atmospheric-turbulence profiling with generalized scidar," Appl. Opt. 36 (30), 7898–7905 (1997). https://doi-org.wrs.idm.oclc.org/10.1364/AO.36.007898.

[41] R. E. Hufnagel "Variation of atmospheric turbulence." Digest of technical papers, *Topical Meetic on Optical Propagation through Turbulence* (1974).

[42] R. Goldstein, "Pockels cell primer." *Laser Focus* 34 (1968): 21.

[43] R. Ragazzoni, E. Diolaiti, J. Farinato, E. Fedrigo, E. Marchetti, M. Tordi, and D. Kirkman. "Multiple field of view layer-oriented adaptive optics-Nearly whole sky coverage on 8 m class telescopes and beyond." *Astronomy & Astrophysics* 396.2 (2002): 731-744.

[44] R. Ramlau, D. Saxenhuber, and M. Yudytskiy. "Iterative reconstruction methods in atmospheric tomography: FEWHA, Kaczmarz and Gradient-based algorithm." *Adaptive Optics Systems IV*. Vol. 9148. International Society for Optics and Photonics, 2014.

[45] S. Basu, H. Ping. "Estimating refractive index structure parameter (C2n) profiles in the atmosphere: a wavelet transform-based approach." *Laser Communication and Propagation through the Atmosphere and Oceans IV*. Vol. 9614. International Society for Optics and Photonics, 2015.

[46] S. Bose-Pillai, B. Wilson, J. Krone, A. Archibald, B. Elmore, J. McCrae, S. Fiorino, "Profiling atmospheric turbulence using dual-camera imagery of non-cooperative targets," Proc. SPIE 11506, Laser Communication and Propagation through the Atmosphere and Oceans IX, 115060J (22 August 2020).

[47] S. Bose-Pillai, J. McCrae, C. Rice, R. Wood, R. Murphy, S. Fiorino. "Estimation of atmospheric turbulence using differential motion of extended features in time-lapse imagery." *Optical Engineering* 57.10 (2018): 104108.

[48] S. Fiorino, D. Meier. "Improving the Fidelity of the Tatarskii $C_n^2$ Calculation with Inclusion of Pressure Perturbations." Propagation Through and Characterization of Atmospheric and Oceanic Phenomena, 2016, doi:10.1364/pcaop.2016.m1a.1.

[49] S. K. Saha, Diffraction-Limited Imaging with Large and Moderate Telescopes. World Scientific Publishing Co. Pte. Ltd. Hackensack, NJ (2007).

[50] S. Thomas. "A simple turbulence simulator for adaptive optics." *Advancements in Adaptive Optics*. Vol. 5490. International Society for Optics and Photonics, 2004.

[51] S. Zuraski, E. Beecher, C. Carr, T. Payne, A. Battle, L. Guliano, and S. Fiorino, "Turbulence and aerosol research dynamic interrogation system testing," in *Adv. Maui Opt. and Space Surveillance Technol. Conf.* (2018).

[52] S. Zuraski, E. Beecher, J. McCrae, S. Fiorino, "Turbulence profiling using pupil plane wavefront data derived Fried parameter values for a dynamically ranged Rayleigh beacon," Opt. Eng. 59(8), 081807 (2020), doi: 10.1117/1.OE.59.8.081807.

[53] S. Zuraski, J. McCrae, S. Fiorino. "Focal anisoplanatism influence on dynamically ranged Rayleigh beacon measurements." *Unconventional Imaging and Adaptive Optics 2020*. Vol. 11508. International Society for Optics and Photonics, 2020.

[54] S. Zuraski, S. Fiorino, E. Beecher, N. Figlewski, J. Schmidt, J. McCrae. "Electro-optic testbed utilizing a dynamic range gated Rayleigh beacon for atmospheric turbulence profiling." Optics in Atmospheric

Propagation and Adaptive Systems XIX. Vol. 10002. International Society for Optics and Photonics (2016).

[55] S. Zuraski, S., E. VanTilburg, M. Wilson, J. E. McCrae, & S. T. Fiorino. Implications of polarized pupil degradation due to focal shifts in dynamically ranged Rayleigh beacons. *Applied Optics*, *60*(3), 606-615. (2021)

[56] T. Butterley, R. Wilson, and M. Sarazin. “Determination of the profile of atmospheric optical turbulence strength from slodar data,” Mon. Not. R. Astron. Soc. 369, 835–845 (2006). https://doi-org.wrs.idm.oclc.org/10.1111/j.1365-2966.2006.10337.

[57] T. Cherubini, S. Businger. "Another look at the refractive index structure function." *Journal of Applied Meteorology and Climatology* 52.2 (2013): 498-506.

[58] T. J. Brennan. "Anatomy of the slope discrepancy structure function: characterization of turbulence." Laser Systems Technology. Vol. 5087. International Society for Optics and Photonics, 2003.

[59] T. Payne, E. VanTilburg, A. Chaudhary, M. Wilson, S. Payne, L. Weisenbach, R. Gnawali, J. Gibson, D. Beamer, A. Battle, and L. Guliano. “Small Telescope Electro-Optical Research”. DTIC Final Report AFRL-RY-WP-TR-2020-0121 (2020).

[60] V. I. Tatarski, 1961: *Wave Propagation in a Turbulent Medium*. McGraw-Hill, 285 pp.

[61] V. I. Tatarskii, “The effects of the turbulent atmosphere on wave propagation,” translation, Published for NOAA by the Department of Commerce and the National Science Foundation, Washington D.C. (1971). Israel Program for Scientific Translations.

[62] Y. Zhang, M. C. Roggemann, T. J. Schulz, and R. Kizito. (2004, January). Compensation of laser beam projection through turbulence in multimirror adaptive optics system with phase retrieval method. In *Free-Space Laser Communication and Active Laser Illumination III* (Vol. 5160, pp. 98-106). International Society for Optics and Photonics.

[63] Z. Barber, J. Dahl, R.Blaszczyk, S. Crouch, J. Love, B. Kilty, Em Kadlec, R. Reibel. "Coherent Lidar Techniques for Atmospheric Turbulence Measurements and Imaging." *Propagation Through and Characterization of Atmospheric and Oceanic Phenomena*. Optical Society of America, 2018.

[64] Z. Barber. *Synthetic Aperture Ladar Imaging and Atmospheric Turbulence*. Montana State University Bozeman, Bozeman, United States, 2016.

[65] Zemax Optical Studio, optical design and simulation software, URL: http://www.zemax.com

# REPORT DOCUMENTATION PAGE

*Form Approved*
*OMB No. 074-0188*



| 1. REPORT DATE *(DD-MM-YYYY)* | 2. REPORT TYPE | 3. DATES COVERED *(From – To)* |
|---|---|---|
| 12-07-2021 | Dissertation | August 2019 – July 2021 |

**TITLE AND SUBTITLE**

PROFILING ATMOSPHERIC TURBULENCE USING A DYNAMICALLY RANGED RAYLEIGH BEACON SYSTEM

**5a. CONTRACT NUMBER**

**5b. GRANT NUMBER**

**5c. PROGRAM ELEMENT NUMBER**

**6. AUTHOR(S)**

Zuraski, Steven M., Civilian, USAF

**5d. PROJECT NUMBER**

**5e. TASK NUMBER**

**5f. WORK UNIT NUMBER**

**7. PERFORMING ORGANIZATION NAMES(S) AND ADDRESS(S)**
Air Force Institute of Technology
Graduate School of Engineering and Management (AFIT/ENY)
2950 Hobson Way, Building 640
WPAFB OH 45433-8865

**8. PERFORMING ORGANIZATION REPORT NUMBER**

AFIT-ENP-DS-21-S-036

**9. SPONSORING/MONITORING AGENCY NAME(S) AND ADDRESS(ES)**
AGENCY (spelled out)
ADDRESS
PHONE and EMAIL
ATTN: POC
(no sponsor enter: Intentionally left blank)

**10. SPONSOR/MONITOR'S ACRONYM(S)**

**11. SPONSOR/MONITOR'S REPORT NUMBER(S)**

**12. DISTRIBUTION/AVAILABILITY STATEMENT**
**DISTRUBTION STATEMENT A.** APPROVED FOR PUBLIC RELEASE; DISTRIBUTION UNLIMITED.

**13. SUPPLEMENTARY NOTES**
This material is declared a work of the U.S. Government and is not subject to copyright protection in the United States.

**14. ABSTRACT**

This body of research provides a new means for quantifying the strength profile of atmospheric turbulence. Utilizing the outlined methodologies, a direct measurement of the perturbed wavefront is used which differs fundamentally from other means of estimating a turbulence strength profile. This dissertation provides the foundational theory for understanding atmospheric turbulence, provides reference to currently available turbulence estimation techniques, and provides details towards TARDIS, the tomographic turbulence estimation methodology, and analysis of initial proof of concept data collected.

**15. SUBJECT TERMS**
(Fill in with pertinent terminology related to the topic of your thesis.)

| 16. SECURITY CLASSIFICATION OF: | | | 17. LIMITATION OF ABSTRACT | 18. NUMBER OF PAGES | 19a. NAME OF RESPONSIBLE PERSON |
|---|---|---|---|---|---|
| a. REPORT | b. ABSTRACT | c. THIS PAGE | | | Steven Fiorino, AFIT/ENP |
| U | U | U | U | 186 | 19b. TELEPHONE NUMBER *(Include area code)* (937) 255-3636, ext 4506 (Steven.Fiorino@afit.edu) |

**Standard Form 298 (Rev. 8-98)**
Prescribed by ANSI Std. Z39-18